

## This is to certify that the dissertation entitled

# HIGH RESOLUTION ANALYSIS OF EXTRAGALACTIC GLOBULAR CLUSTERS

presented by

**Christopher Z Waters** 

has been accepted towards fulfillment of the requirements for the

Ph. D degree in Physics and Astronomy

Major Professor's Signature

(2/12(3:2)

Date

MSU is an affirmative-action, equal-opportunity employer

LIBRARY Michigan State University PLACE IN RETURN BOX to remove this checkout from your record.

TO AVOID FINES return on or before date due.

MAY BE RECALLED with earlier due date if requested.

DATE DUE	DATE DUE	DATE DUE
MAR Q 440 20131 3		

6/07 p:/CIRC/DateDue.indd-p.1

# HIGH RESOLUTION ANALYSIS OF EXTRAGALACTIC GLOBULAR CLUSTERS

 $\mathbf{B}\mathbf{y}$ 

Christopher Z Waters

#### A DISSERTATION

Submitted to
Michigan State University
in partial fulfillment of the requirements
for the degree of

DOCTOR OF PHILOSOPHY

Department of Physics and Astronomy

2007

#### ABSTRACT

## HIGH RESOLUTION ANALYSIS OF EXTRAGALACTIC GLOBULAR CLUSTERS

By

#### Christopher Z Waters

Globular clusters are massive compact groups of stars, with masses that range beyond  $10^6 M_{\odot}$ . Because they are so large, they can remain bound together as they orbit their host galaxies. They are also very luminous, which ensures that they can be seen at distances far beyond the point where individual stars are no longer visible. The combination of these two qualities makes them wonderful test particles to explore how the dynamical interactions of stars in the cluster change the observed parameters. The evolution of these clusters has not been very well constrained by observations. They must lose mass as they orbit, but the exact way that this mass loss changes their observed properties is not well known.

M87 is a massive galaxy located 16 Mpc away from the Milky Way. This makes it much farther than other galaxies that have clearly resolved globular clusters. However as M87 is so massive  $(M \sim 10^{12} M_{\odot})$ , its globular cluster population is much more numerous than those of other closer galaxies. Only about 150 globular clusters have been detected in the Milky Way, whereas M87 should have close to 10000 clusters. This large population allows for any observed relations to be less influenced by statistical uncertainty.

The core of M87 was imaged with the Advanced Camera for Surveys on the Hubble Space Telescope as part of a 50 orbit program in 2005 and 2006. During each orbit, multiple exposures were taken in the infrared F814W and red F606W filters, giving total exposure times of 73,800s in F814W and 24,500s in F606W. These very long

exposures provide some of the deepest data ever taken with HST.

As the data used in this project can resolve the faintest clusters, we can use it to investigate the luminosity and mass functions of the globular clusters in M87. The final sample contains 2091 clusters, with a luminosity function that matches well with previously published results. The mass function generated from these clusters shows the signature of mass loss from two-body relaxation. Much theoretical work has been done to investigate this evolution, but since there are few galaxies in which large numbers of clusters can be observed, these theoretical predictions have been difficult to test in the past. The change in the mass to light ratio between clusters of different ages and metallicity is an important complication in the shape of the mass function. However, by correcting for these changes, this sample shows that the different color groups of the M87 globular clusters indicate different formation epochs.

These data also provide much higher angular resolution than previously available for populous extragalactic systems. This resolution ensures that the clusters are broader than just simple point sources, allowing them to be fit with theoretical models of the cluster structure. Such fits show that the relations between the cluster structure and luminosity appear to be universal, as those found for M87 match well with the Milky Way, the only other complete sample that exists. These structure fits also show that the probability of the formation of low mass X-ray binaries in a cluster is influenced by the rate of stellar interactions.

Copyright by CHRISTOPHER Z WATERS 2007 To the squirrels of Michigan State University

#### **ACKNOWLEDGMENTS**

I would like to thank many people for helping with the science of this thesis. My discussions with Arunav Kundu have been essential in making sure that the analysis of the images and data have been done correctly. It is also likely that the **superking** program would not be in a useful state if not for the comments and suggestions of Mark Peacock. Tod Lauer provided great insight into how to correctly think about the formation of images, which has ensured that my fitting code works as well as it does. I'd also like to thank Ted Baltz for obtaining the telescope time necessary for this project, which has given me such an excellent dataset to work with.

I'd like to thank my advisor, Steve Zepf, for organizing this project, and for having the patience to let me work on problems at my own pace. This extends to my thesis committee, Jack Baldwin, Megan Donahue, Wayne Repko, and Bhanu Mahanti, who have made my defense of this thesis fairly easy.

I would like to thank the other grad students for many years of bowling, movies, and board games. Nathan DeLee and Brian Marsteller, in particular, have helped over the years by talking out various issues with me.

Katie Rabidoux kindly provided the photometric data for the stars in M3, used in constructing the color magnitude diagram in chapter 1. This is secondary, however, to her help in reminding me that crab cakes are wonderful. Finally, I'd like to thank Julie Krugler for suggesting many trips to coffeehouses, without which I never would have finished writing this thesis.

#### TABLE OF CONTENTS

Li	st of Table	es x
Li	st of Figu	res xi
Li	st of Syml	bolsxiv
1	Introduc	tion 1
	1.1	Globular Clusters
	1.2	Summary of Thesis Goals
	1.3	Previous Studies of Globular Cluster Systems
	1.4	Outline
2	Dynamic	s of Globular Clusters 9
	2.1	King Models
	2.2	Tidal Radii
	2.2.1	Tidal Radii with Circular Orbits
	2.2.2	Tidal Radii with Elliptical Orbits
	2.3	Mass Loss
	2.3.1	Dynamical Friction
	2.3.2	Stellar Evolution
	2.3.3	Gravitational Shocks
	2.3.4	Two-Body Relaxation
	2.4	Observed Properties of Globular Clusters
3	Point Sp	read Functions
	3.1	Pixel Response Functions and the Effective PSF 29
	3.2	PSFs for Extended Objects
	3.3	Evaluating the PSF for HST
	3.3.1	TinyTim
	3.3.2	Empirical PSFs
	3.4	PSF Generation
4	Data Rec	duction
	4.1	Image Combination
	4.1.1	Lauer Fourier Method
	4.1.2	Drizzle
	4.1.3	Determining Shifts
	4.2	Data Summary
	4.2.1	WFPC/2
	4.2.2	ACS
	4.3	Image Preparation

	4.3.1	Unsharp Masking	46
	4.3.2	Isophote Fitting	47
	4.3.3	Final Method	47
5	Globular	Cluster Luminosity Function	57
	5.1	Object Detection	57
	5.1.1	Instrumental Magnitudes	59
	5.2	Completeness Correction	59
	5.3	Photometric Calibration	60
	5.3.1	Aperture Correction	60
	5.3.2	Color Correction and Extinction	62
	5.4	Contamination	65
	5.4.1	Noise Objects	65
	5.4.2	Background Galaxies	66
	5.5	Cluster Candidates	67
	5.5.1	Photometric Accuracy	71
	5.6	Luminosity Function	73
	5.6.1	Color Dependence	73
	5.6.2	Radial Dependence	74
	5.6.3	Comparison with Published Results	75
	5.7	Blue Tilt	82
6	Clobular	Cluster Mass Function	87
U	6.1	Initial Mass Function of Globular Clusters	88
	6.2	Mass Loss Rates	89
	6.2.1	Fall & Zhang	90
	6.2.1	Baumgardt & Makino	90
	6.2.2	Lamers et al	92
	6.3	Mass Function	93
	6.3.1		95
	6.3.1	Comparison to Mass Loss Models	96
	$\begin{array}{c} 6.3.2 \\ 6.3.3 \end{array}$	Mass to Light Ratio	
		Comparison to Previous Results	99
	6.3.4	Color Dependence of the Mass Loss	100
7	Structura		104
	7.1	Error Analysis	105
	7.1.1	Position Errors	107
	7.1.2	0	107
	7.1.3	Structure Errors	108
	7.2	Fitting Results	109
8	Globular	Cluster Structure Results	112
	8.1	· · · · · · · · · · · · · · · · · · ·	113
	8.2	Effect of Distance on Structure	116
	8.3	Relations Between Core Parameters	116
	8.4	The Fundamental Plane of Globular Clusters	117
	8.5	LMXB Probability	118

9	Conclusio	$\mathrm{ons}\ldots\ldots 12^{2}$	1
A	Detailed	Source Code	7
	A.1	libkingmodel	7
	A.1.1	kingmodel.c	8
	A.1.2	kingimage.c	1
	A.1.3	kingconvolve.c	2
	A.1.4	kingutils.c	3
	A.2	Superking	4
	A.2.1	Initialization	5
	A.2.2	Fit Evaluation	6
	A.2.3	Fitting Procedure	7
В	Globular	Cluster Catalog14	0
	Reference	es	3

#### LIST OF TABLES

5.1	Source Extractor quantities	58
5.2	Color correction parameters	63
5.3	Sample size	71
5.4	Radial dependence of the GCLF	75
5.5	GCLF parameters	81
5.6	Bimodality with cluster luminosity	82
6.1	Best fitting mass loss fits to ACS data	94
6.2	Best fitting mass loss fits with variable $\Upsilon$	99
A.1	Search ranges for fitting	139

#### LIST OF FIGURES

1.1	Optical image of galactic globular cluster M3	6
1.2	Globular cluster color magnitude diagram	7
1.3	Optical image of Virgo Cluster	8
2.1	King model mass density and projected surface density profiles	12
2.2	Comparison of $W_0$ and $c$	24
3.1	Comparison of HST PSF to an Airy disk	29
3.2	Comparison of TinyTim and empirical PSFs	33
3.3	Comparison between calculated PSF and star	36
4.1	Original raw ACS image	49
4.2	Distortion corrected ACS image.	50
4.3	Final F606W reduced image	51
4.4	Final F814W reduced image	52
4.5	Result of unsharp masking method of galaxy subtraction	53
4.6	Result of ELLIPSE method for galaxy subtraction	54
4.7	Image histograms of galaxy subtracted images	55
4.8	Result of final galaxy subtraction	56
5.1	Completeness surfaces	61
5.2	Aperture correction surfaces	63
5.3	Color correction curve relating instrumental to final colors	65
5.4	Original F606W UDF image.	69

5.5	M87 data	70
5.6	Color magnitude diagrams of detected objects	72
5.7	Color magnitude diagram of the final sample of clusters	77
5.8	Final GCLF	78
5.9	Comparison of the red and blue cluster GCLFs	79
5.10	Radial Dependence of the GCLF	80
5.11	Comparison of the V GCLF to previously published results	84
5.12	Comparison of the I GCLF to previously published results	85
5.13	Blue tilt	86
6.1	Comparison of $\dot{M} \propto M^{-0.25}$ mass loss model to N-body simulations	92
6.2	M87 GCMF with best fitting mass loss models	95
6.3	Best fitting mass loss model with variable $\Upsilon.$	98
6.4	Comparison of the new GCMF to those previously published	101
6.5	Comparison of the GCMFs for the red and blue samples	103
7.1	Expected errors in position	108
7.2	Expected errors in magnitude and background level	110
7.3	Expected errors in the structural parameters	111
7.4	Fitting residuals.	111
8.1	Parameter correlations with absolute magnitude	115
8.2	Parameter trends in averaged bins of luminosity	120
8.3	Parameter correlations with projected galactocentric distance	121
8.4	Correlations between core structural parameters	122
8.5	LMXB Structure	123

Images in this dissertation are presented in color.

#### LIST OF SYMBOLS

$r_c$	Core Radius	10
W	Reduced Potential	11
Υ	Mass to Light Ratio	13
$r_t$	Tidal Radius	13
$t_r$	Relaxation time	22
$W_0$	Central potential	24
c	Concentration	24
$r_{hm}$	Half mass radius	24
$R_h$	Half light radius	24
$\mu_0$	Central surface brightness	25
$ ho_0$	Central mass density	26
$t_{rc}$	Core relaxation time	26
$t_{rh}$	Half mass relaxation time	26
П	Point Spread Function of a telescope.	27
$\mathscr{R}$	Pixel Response Function	29
$\Pi_{ ext{eff}}$	Effective PSF	30
$M_C$	IMF cutoff mass	88
$\gamma$	Mass loss decay exponent	89
au	Total mass loss from evaporation	89

# CHAPTER 1: INTRODUCTION

Globular clusters (GCs) are spherical groupings of many stars that are bound together by their own self gravity. They appear in every galaxy observers have studied, and seem to be among the oldest structures in the universe. High resolution images of galactic globular clusters, such as the Sloan Digital Sky Survey (SDSS) image of the globular cluster M3 presented in figure 1.1, show an obvious overdensity of stars compared to the background, with a very dense core of stars blending together.

#### 1.1 GLOBULAR CLUSTERS

The first globular cluster was discovered by Johann Abraham Ihle on August 26, 1665 while he was observing Saturn (Schultz, 1866). This object, now known as M22, was just one of the 28 galactic globular clusters that appear in Charles Messier's catalog of "nebulae," published roughly a hundred years later. The nature of these objects was first suggested by William Herschel (Herschel, 1789), who was able to resolve the individual stars in the cluster. This fact made it clear that globular clusters must be composed of many stars, and as the stars in the center of the cluster are more tightly packed, they must be held together by the mutual attractions between the component stars.

Following their discovery, star counts were used to estimate the shape of the mass profile, and with the introduction of statistical mechanics in the late nineteenth century, globular clusters began to be modeled as a gas of stars (Plummer, 1911). By the

middle of the twentieth century, steady state solutions were found that could satisfactorily match the observed density profiles (Hénon, 1961; King, 1966). However, these solutions indicated that the structure and evolution of these objects are intrinsically linked, and must be treated simultaneously. This realization has led to recent attempts to explain globular clusters using N-body simulations of the component stars, which can investigate both the structure and evolution (Baumgardt & Makino, 2003).

Globular clusters are believed to form from the collapse of giant molecular clouds. This collapse must happen relatively quickly, as the ignition of hydrogen burning in massive stars is likely sufficient to disperse any remaining gas. Because of this, all the stars in the cluster can be assumed to have formed at the same time, and as they all form from gas with the same chemical enrichment, they must all share the same metal content.

These two facts make globular clusters excellent laboratories to examine the lives of stars, as the only difference between the individual stars is their masses. The stars in the cluster therefore fall upon a path that traces the evolutionary history of the stars. Figure 1.2 illustrates the color magnitude diagram of the galactic globular cluster M3. The main sequence of stars is clearly visible up to the turnoff around  $V \sim 18.5$ . This point marks where massive stars are starting to evolve away from the main sequence, and up the red giant branch. The main sequence lifetimes of stars at the turnoff provide an estimate of the age of the cluster. These ages indicate that the globular clusters in the Milky Way are very old, with current ages on the order of the age of the universe.

Globular clusters are generally more metal poor than the Sun, consistent with their great ages. Like the metal poor stars of the galactic halo, the Milky Way globular cluster system is spherically distributed around the center of the galaxy. This fact was instrumental in one of the great discoveries of the structure of the Milky Way. Shapley (1921) used the observation that the globular clusters visible from Earth

are not isotropic in the sky, and that they seem to be distributed about a point 8kpc away. This led to the conclusion that the Earth is not located at the center of the galaxy.

#### 1.2 Summary of Thesis Goals

This thesis examines very deep observations of the central regions of the giant elliptical galaxy M87. This galaxy is a member of the Virgo cluster of galaxies, and is located at a distance of 16 Mpc (Macri et al., 1999). Figure 1.3 shows a section of the Virgo cluster as seen by the SDSS (Stoughton et al., 2002) with the bright object in the lower left corner being M87. The observations for this project were taken using the Advanced Camera for Surveys (ACS) aboard the Hubble Space Telescope (HST). This camera has a field of view of 202". × 202", which covers an area roughly the size of the bright core of M87 visible in the SDSS image. Although this relatively small image size does not allow the analysis of the full M87 globular cluster system (believed to number up to 10000 objects), by taking advantage of very long exposure time images, the sample of the GCs will be effectively volume limited, with even the faintest objects measured.

Without a cutoff in luminosity, such a sample can be used to construct a complete luminosity function for the M87 globular cluster system. This luminosity function can then be used to constrain the evolution of the clusters. The high angular resolution that HST provides also allows the clusters to be resolved, which allows their structure to be examined. Therefore, this data set presents an opportunity to put observational constraints on the structure and evolution of the cluster properties. As the number of clusters that comprise the sample is very large (N  $\sim$  2000), such constraints have the power to be more statistically rigorous than can be provided by the Milky Way.

## 1.3 Previous Studies of Globular Cluster Systems

For obvious reasons, the Milky Way GC system was the first to be examined in detail. The Harris (1996) compilation is the standard catalog of Milky Way clusters, drawing the best determined values from the published literature. The relations between the various structural parameters were examined by Djorgovski & Meylan (1994), which is currently the most reliable set of correlations between the parameters, despite the low number of clusters.

Although M31 is an obvious next choice for a target, many factors contribute to hinder the classification of the GC system. As the galaxy is mostly face on, the clusters are projected against the galaxy light, which makes them difficult to detect. In addition, the large angular size of the galaxy means that a complete survey requires many pointings. The most complete current survey is that of Barmby & Huchra (2001), containing 400 clusters.

Elliptical galaxies are generally considered the best locations to search for GCs as they have smooth light profiles against which clusters show up easily. In addition, elliptical galaxies have much larger numbers of globular clusters per unit luminosity. M87 has been studied before with the WFPC/2 camera on HST (Whitmore et al., 1995; Kundu et al., 1999; Waters et al., 2006). Recently, it was re-examined as part of the ACS Virgo Cluster Survey (ACSVCS) (Côté et al., 2004) which studied 100 galaxies in the Virgo cluster. The number of clusters examined per galaxy varies widely, which limits the conclusions that can be drawn from this sample. Another issue is that the survey did not have the depth required to detect the faintest clusters.

#### 1.4 OUTLINE

This thesis is organized as follows: Chapter 2 discusses the dynamical processes that shape globular clusters, and presents the background theory that is used in later chapters. Chapter 3 discusses the point spread function, and how this affects the image quality. Chapter 4 outlines the data reduction techniques used. Chapters 5 and 6 cover the globular cluster luminosity and mass functions, respectively, and discuss their applications to the evolution of the globular cluster system. Chapter 7 presents a new method for measuring the structural parameters of the globular clusters from high quality data, and chapter 8 presents the results of the measured parameters. Finally, Chapter 9 summarizes the results of this study, and presents the final conclusions. Appendix A gives the documentation for the code written for this thesis that simulates and fits globular cluster profiles and images. Appendix B discusses the final database of cluster parameters.



Figure 1.1 Image of the Milky Way globular cluster M3. This clearly shows that the core of the cluster contains many stars, but that even at radii much larger than this core, the cluster contains more stars than the background. This image was taken from the SDSS image server at http://www.wikisky.com.

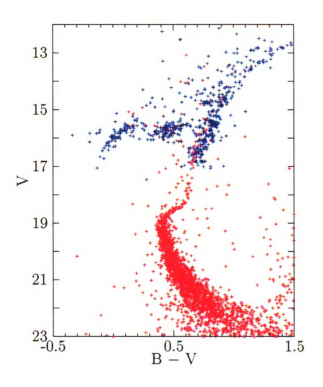


Figure 1.2 Color magnitude diagram of the stars in the globular cluster M3. As the stars are all of roughly the same age, they trace out the path of stellar evolution. The main sequence clearly is truncated at  $V\sim 19$ , indicating that more massive stars have evolved, populating the red giant branch. Measurements with V>17 are taken from SDSS catalogs (Stoughton et al., 2002). The measurement of the brighter stars shown in blue were supplied by Katie Rabidoux (private communication), based on observations taken at the MSU 24" telescope.

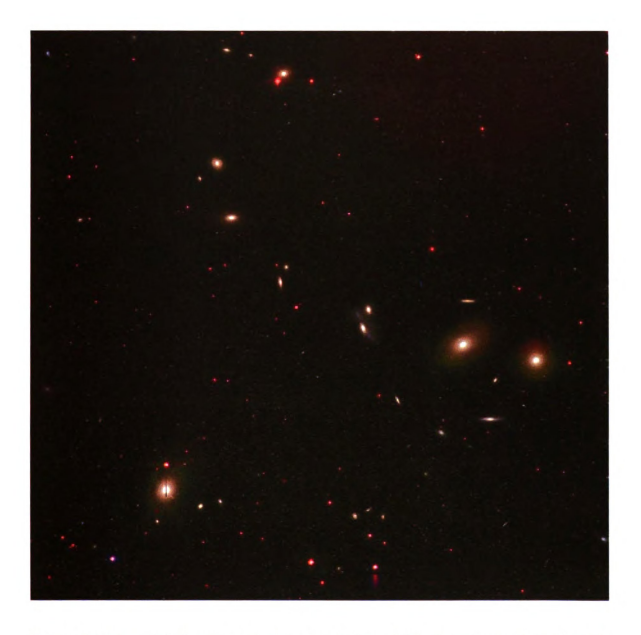


Figure 1.3 Image of the Virgo cluster of galaxies. M87, the target galaxy for this project, is located in the bottom left corner. M86 and M84 are the other two large elliptical galaxies on the right side of the image along with the stream of galaxies known as Markarian's Chain. This image was taken from the SDSS image server at http://www.wikisky.com.

## CHAPTER 2:

## DYNAMICS OF GLOBULAR CLUSTERS

#### 2.1 KING MODELS

The standard assumption for modeling the dynamics of globular clusters is that they are comprised of a large number of identical stars of mass m moving in the potential created by their own self gravity. We can initially assume that the system is collisionless, and neglect two-body interactions. The distribution function of the stars can then be defined to be  $f(\vec{x}, \vec{v}, t) \geq 0$ .

Jeans theorem states that the steady-state solution to the collisionless Boltzmann equation is a function only of integrals of motion in the potential (Binney & Tremaine, 1987). If we assume our system is spherically symmetric, then there are four such integrals: the total energy E and the three components of the angular momentum vector  $\vec{L}$ . This allows us to write our distribution function as

$$f = f(E, \vec{L})$$

For our globular cluster system, the potential that binds the stars together is generated by the stars themselves. Therefore, from Poisson's equation

$$\nabla^2 \Phi = -4\pi G \rho = -4\pi G m \int f d^3 \vec{v}$$
 (2.1)

We can make the assumption that the distribution function is isotropic, so the distri-

bution depends only on the particle energy based on the observations that globular clusters do not have significant rotation. Therefore,

$$f_{GC} = f(E)$$

A first guess for the distribution function for the stars in a globular cluster is that of the isothermal sphere, in which we assume that the energy of all stars is given by a Maxwellian distribution:

$$f_{\text{isothermal}}(E) = f_0 e^{-E/\sigma^2} = f_0 e^{\frac{-\Phi - \frac{1}{2}mv^2}{\sigma^2}}$$
 (2.2)

This yields an equation for the density

$$\rho_{\text{isothermal}}(\Phi) = 4\pi \int_0^\infty f_0 e^{\frac{-\Phi - \frac{1}{2}mv^2}{\sigma^2}} v^2 dv = \rho_0 e^{-\frac{\Phi}{\sigma^2}}$$
(2.3)

Poisson's equation allows us to rewrite this in terms of the radius from the center of the cluster instead of the local potential

$$-4\pi G\rho = \frac{1}{r^2} \frac{d}{dr} \left( r^2 \frac{d\Phi}{dr} \right)$$

$$\rho_{\text{isothermal}}(r) = \frac{\sigma^2}{2\pi G r^2}$$
(2.4)

From this potential, we can define the core radius (called the King radius by some authors) as

$$r_c = \sqrt{\frac{9\sigma^2}{4\pi G\rho_0}} \tag{2.5}$$

This radius is the point where the projected density equals roughly one half the central value. This radius represents a convenient radius scale for the cluster.

It is clear that this is a poor solution for globular clusters, as the total mass diverges to infinity when integrated over all radii. We can modify the isothermal

sphere by noting that globular clusters orbit host galaxies, and as such, experience an external potential  $\Phi_{G}$ . This assumption leads to a cutoff in the size of the cluster, as there will be a point where a test particle feels an equal pull to the cluster and the galaxy. This point is known as the tidal radius of the cluster (see section 2.2).

We can set the distribution for this model to be a modified "lowered isothermal" model:

$$f(E) = \begin{cases} f_0 \left( e^{-E/\sigma^2} - e^{-E_T/\sigma^2} \right) & E < E_T \\ 0 & E \ge E_T \end{cases}$$
 (2.6)

We can make the simplification that any particle that "just reaches" the tidal radius will be stripped from the cluster, so we can set  $E_T = \Phi(r_t)$ . We can then renormalize the potential such that  $\Phi(r_t) = 0$ , which gives

$$f_{\text{King}}(E) = \begin{cases} f_0 \left( e^{-\frac{\Phi + \frac{1}{2}mv^2}{\sigma^2}} - 1 \right) & E < 0 \\ 0 & E \ge 0 \end{cases}$$
 (2.7)

This distribution function yields a density of

$$\rho_{\text{King}} = 4\pi f_0 \int_0^{v_{max}} e^{-\frac{\Phi + \frac{1}{2}mv^2}{\sigma^2}} v^2 dv$$
 (2.8)

where  $v_{max} = \sqrt{-\frac{2\Phi}{m}}$  from the virial theorem. Defining a "reduced potential"  $W = -\frac{\Phi}{\sigma^2}$ , allows this to be solved as

$$\rho_{\text{King}}(W) = \rho_1 \left( e^W \operatorname{erf}(\sqrt{W}) - \sqrt{\frac{4}{\pi}W} \left( 1 + \frac{2}{3}W \right) \right)$$
 (2.9)

We can again use Poisson's equation to find a the density at a given radius

$$\frac{d}{dr}\left(r^2\frac{dW}{dr}\right) = -4\pi G\rho_1 r^2 \left(e^W \operatorname{erf}(\sqrt{W}) - \sqrt{\frac{4}{\pi}W}\left(1 + \frac{2}{3}W\right)\right)$$
(2.10)

Unlike the isothermal sphere, this differential equation must be solved numerically (see Appendix A.1 for details on fast and accurate evaluation of King models). Figure 2.1 shows how the volume and projected surface density change with radius for a set of central potentials,  $W_0$ .

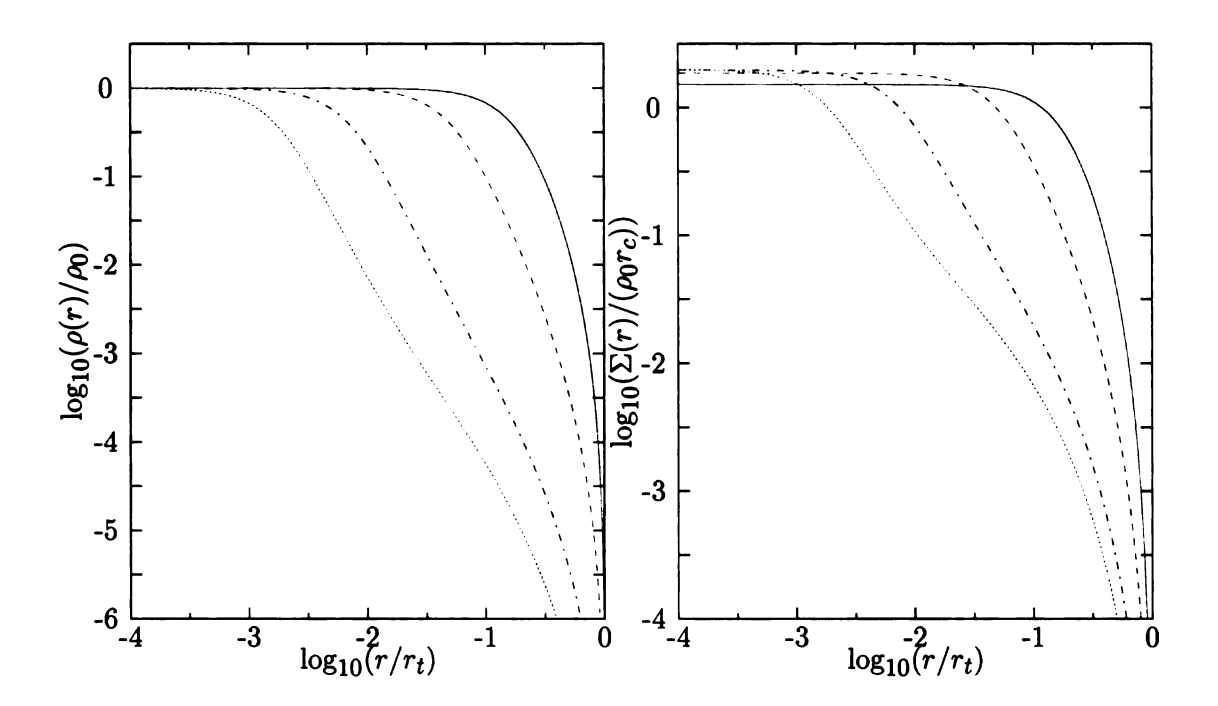


Figure 2.1 Mass density and projected surface density for single mass King models values of  $W_0 = 3$  (red), 6 (green), 9 (blue), and 12 (magenta). The highest value of  $W_0$  falls off the fastest in this plot.

Although this model has been used successfully to fit globular cluster surface brightness profiles, deviations for high quality profiles have led to many attempts at a more realistic model. The most intuitively reasonable is the multi-mass King model (Da Costa & Freeman, 1976), which allows the stars in the cluster to have a distribution instead of just a single value. If we assume energy partition between all

the stars, such that  $m_i \sigma_i^2 = m_j \sigma_j^2$  then the distribution function becomes

$$f_{\text{MM}}(E) = \begin{cases} \sum_{i} C_{i} f_{0} \left( e^{-\frac{\Phi + \frac{1}{2}mv^{2}}{\sigma^{2}}} - 1 \right) & E < 0 \\ 0 & E \ge 0 \end{cases}$$
 (2.11)

where the  $C_i$  are the fractional masses for each class of stars. Extra care must be taken when using such models to fit clusters, because although the mass is given by this distribution function, the fact that the mass to light ratio  $\Upsilon$  may not be the same for each class of stars means that the observed light distribution may not match the mass distribution.

Another change to the standard King model that has been proposed is to relax the requirement of velocity isotropy (Gunn & Griffin, 1979). If the stars have different masses, then some of them will be scattered onto non radial orbits. Such a model provides a distribution function of the sort

$$f(E,L) = \begin{cases} \sum_{i} C_{i} e^{-L^{2}/(2\sigma_{i}^{2}r)} f_{0} \left( e^{-\frac{\Phi + \frac{1}{2}mv^{2}}{\sigma^{2}}} - 1 \right) & E < 0 \\ 0 & E \ge 0 \end{cases}$$
 (2.12)

However, both of these changes to the simple single mass King model require very precise star counts to observe any deviations from the predicted projected density of the standard single mass King model projected density. They also require many more assumptions about the properties of the stars in the cluster, and because of this, can be adjusted in many ways to ensure a good fit.

#### 2.2 TIDAL RADII

As globular clusters orbit a host galaxy, their sizes must be constrained in some fashion. At some radius  $r_t$ , their density profiles must drop to zero, and all stars

outside this radius must be considered bound instead to the host galaxy. A simple estimate of this size can be found by calculating the point at which tidal interactions with the host galaxy will cause stars to leave the cluster.

The gravitational force keeping a star bound to the cluster is obviously just

$$F_{\text{cluster}} = -\frac{GM_CM_{\star}}{r_C^2} \tag{2.13}$$

Along a line connecting the cluster and the host galaxy, the tidal force will be

$$F_{\rm tidal} = \frac{2\Delta r G M_G M_{\star}}{r_G^3} \tag{2.14}$$

In this case, setting  $\Delta r \equiv r_C$  gives the tidal force felt by a star along this line, and allows us to estimate the tidal radius as

$$r_t = r_G \sqrt[3]{\frac{M_C}{2M_G}} \tag{2.15}$$

#### 2.2.1 TIDAL RADII WITH CIRCULAR ORBITS

This result neglects the fact that the cluster is not stationary in the galactic potential, but instead orbits the galaxy. If we take the simple assumption of circular orbits, then the cluster and host galaxy experience a potential that can be considered time independent in a frame that rotates about the center of mass with angular velocity

$$\omega^2 = \frac{G(M_G + M_C)}{r_G^3} \tag{2.16}$$

In such a frame, Jacobi's integral is constant, and is given by

$$E_J = \frac{1}{2}v^2 + \Phi_G + \Phi_C \tag{2.17}$$

$$= \frac{1}{2}\dot{r}^2 + \frac{1}{2}r^2\omega^2 + \Phi_{G+C} \tag{2.18}$$

$$= \frac{1}{2}\dot{r}^2 + \Phi_{\text{eff}} \tag{2.19}$$

where  $\Phi_{eff}$  is the effective potential felt by a star:

$$\Phi_{\text{eff}} = \frac{GM_G}{r_G} + \frac{GM_C}{r_C} + \frac{1}{2}r^2 \frac{G(M_G + m_C)}{r_G^3}$$
 (2.20)

As  $\dot{r}^2$  is always a positive quantity, there exists a range of valid potentials to keep  $E_J$  constant, which in turn constrains the region of space in which the stars can occupy and be part of the cluster. This boundary is the Roche surface for the cluster, and we can estimate the tidal radius by taking the distance from the center of the cluster to the Lagrange point between the cluster and the galaxy. This yields a value

$$r_t = r_G \sqrt[3]{\frac{M_C}{3M_G}} \tag{2.21}$$

which is close to the estimate from a static case (Binney & Tremaine, 1987).

Unfortunately, this tidal radius is poorly defined. The surface of zero velocity is not spherical, and as such, the radius changes at different orientations with the host galaxy. In addition, stars that pass this radius are not lost with 100% efficiency. Although they are likely to remain unbound if they pass beyond this surface, they will still travel along with the cluster for some time. Finally, the most important problem is due to clusters not orbiting on perfectly circular paths, but rather following elliptical orbits.

#### 2.2.2 TIDAL RADII WITH ELLIPTICAL ORBITS

A cluster on an elliptical orbit experiences a potential that varies with time. As this is difficult to calculate (as it also depends on the relaxation time of the cluster), the standard assumption (King, 1962) is that the tidal radius is set at pericenter, and stays fixed at that size for the remainder of the orbit. This assumption leads to a tidal radius with the form

$$r_t = r_G \sqrt[3]{\frac{M_C}{(3+e)M_G}}$$
 (2.22)

where e is the orbital eccentricity of the cluster. Other models (Innanen et al., 1983) have modified this result by considering the motion of the cluster through a realistic mass distribution, and calculating the tidal radius at pericenter. This gives just a slight change,  $r_t = \frac{2}{3}r_{t\,\text{elliptical}}$ .

Recently, Brosche et al. (1999) have suggested that the ratio of the true observed tidal radius to the theoretical tidal radius can be parameterized by the form

$$\frac{r_{t \text{ observed}}}{r_{t \text{ theoretical}}} = 10^{c} \left(\frac{r_{A}}{r_{P}}\right)^{b} \tag{2.23}$$

where  $r_A$  and  $r_P$  are the apo- and peri-center distances. They provide their preferred values of b = 0.664 and c = -0.405. This can be constrained from observations, as the theoretical tidal radius is proportional to  $M^{1/3}$  (Baumgardt & Makino, 2003).

#### 2.3 Mass Loss

Globular clusters lose mass continually over their lifetimes. There are four main methods by which mass leaves a globular cluster: dynamical friction, stellar evolution, gravitational shocks, and evaporation due to two-body relaxation. As each of these mechanisms have differing time scales, the relative contribution from any one method changes over the cluster's lifetime.

#### 2.3.1 DYNAMICAL FRICTION

Dynamical friction is a slowing felt by a mass as it travels through a population of other masses. In terms of a globular cluster, dynamical friction serves to degrade the orbit of the cluster as it passes through the stars of the galaxy.

Following Binney & Tremaine (1987), we can write the force felt by a globular cluster due to the interactions with the galaxy mass density:

$$F_{\text{dynamical friction}} = \frac{-4\pi \ln \Lambda G^2 M_C^2 \rho(r)}{v_C^2} \left( \text{erf}(X) - \frac{2X}{\sqrt{\pi}} e^{-X^2} \right)$$
(2.24)

where  $\ln \Lambda$  is the Coulomb logarithm,  $X = \frac{v_C}{\sqrt{2}\sigma} \sim 1$ , and  $v_C^2 = \frac{GM_{enc}}{r}$ . This force will cause the cluster to lose angular momentum at a rate

$$\frac{dL}{dt} = \frac{Fr}{M} = v_C \frac{dr}{dt} \tag{2.25}$$

as the cluster speed can be assumed to remain the same. We can solve this differential equation for the time it takes for all of the angular momentum to be dissipated, i.e.,  $r \to 0$ . Doing this, with the M87 mass distribution presented by Vesperini et al. (2003) yields a timescale

$$t_{\rm dynamical \, friction} \sim \frac{3.0905 \times 10^{13} \, \rm yr}{\ln \Lambda} \left(\frac{v_C}{\rm km/s}\right) \left(\frac{M_C}{M_\odot}\right)^{-1} \left(\frac{r}{\rm kpc}\right)^2$$
 (2.26)

This very long timescale makes it clear that the effects of dynamical friction are expected to be very small over the lifetime of a globular cluster. In fact, only the most massive clusters are likely to experience any significant mass loss from this mechanism.

#### 2.3.2 STELLAR EVOLUTION

The next source of mass loss in globular clusters comes from the evolution of the stars that make up the cluster. Taking a simple relation for the main sequence lifetime of bright, massive stars (where  $M > M_{\odot}$ ) (Chernoff & Weinberg, 1990)

$$t_{\rm MS} \sim 6 \times 10^9 \left(\frac{M}{M_{\odot}}\right)^{-3} {
m yr}$$
 (2.27)

We can see that these lifetimes can be far less than the expected lifetime of the cluster, especially for the most massive stars. Since all stellar remnants have a smaller mass than the initial mass of the star, having the highest mass stars fully evolve on very short time scales ( $t_{\rm MS} \sim 10^6$ ) will clearly cause a sudden drop in cluster mass after a similar time period.

The effect of stellar evolution on the cluster mass can be estimated by taking a distribution of stars (such as a Kroupa (2001) IMF with  $N_{\star} \sim 1 \times 10^6$ ), and letting it evolve with the mass of the star immediately changing to the mass of its remnant after its main sequence lifetime has elapsed. This model is clearly an oversimplification, as it ignores mass loss due to stellar winds for high mass stars, and neglects the entire post-main sequence evolution. Regardless, it will provide an estimate of the relative importance of stellar evolution on the cluster mass loss.

Based on the main sequence lifetimes listed above, it is clear that the majority of stellar evolution happens within the first 1 Gyr, after which, the rate should fall quickly. As the fraction of mass in a cluster due to massive stars is assumed to be constant (as this is only dependent on the cluster IMF), we can write the mass loss using the form

$$\frac{dM}{dt} = -\nu_{\rm SE}M\tag{2.28}$$

where  $\nu_{SE}$  is a time dependent function related to the number of stars leaving the main sequence. It is clear that  $\nu_{SE}$  must have a sudden drop at early times as the

most massive stars evolve. This drop should then slow to a small value as lower mass stars become the "most evolved," as these stars evolve on much longer timescales.

The fact that the majority of the mass loss due to stellar evolution occurs very early in the cluster's lifetime is convenient, as it means we can simply ignore all consideration of this mass loss by simply scaling all cluster initial masses to their value after stellar evolution has subsided, and then ignore the effect on the subsequent evolution. This is reasonable as the fact that the mass loss equation above has the solution

$$M(t) = M_0 e^{\int_0^t \nu_{\rm SE}(t')dt'}$$
 (2.29)

Mass loss with this form will only change the normalization of the mass function, although the shape will remain the same.

Finally, it is worth noting that the sudden drop in mass at early times is likely to be sufficient to disrupt clusters that have low binding energy. This suggests that clusters that form with very low initial concentrations, or alternatively, with a disproportionately large number of massive stars relative to the total, are unlikely to survive past the first 1 Gyr, and will be absent from later surveys.

#### 2.3.3 Gravitational Shocks

Gravitational shocks occur as the cluster passes by a large but finite mass distribution, such as the disk of a spiral galaxy or a giant molecular cloud in a galaxy halo. The passage of the cluster by these objects creates gravitational tidal forces that on average transfer energy to the stars in the cluster, making them more likely to escape the cluster.

Given the tidal acceleration acting on a point x in the cluster due to an object at distance R from the cluster,

$$a_{\text{tidal}} = -\frac{2xGM_P}{R^3} \tag{2.30}$$

we can substitute  $R^2 = b^2 + v^2t^2$ , where b is the distance of closest approach for the cluster and the perturbing mass. Using the impulse approximation for this acceleration yields the expected change in velocity for the test star:

$$\Delta v = \frac{2GM_Px}{b^2v} \tag{2.31}$$

We can then find the average change in energy per unit mass

$$\Delta E = \frac{1}{2}\Delta v^2 = \frac{1}{2}x^2 \left(\frac{2GM_P}{b^2v}\right)^2$$
 (2.32)

and, by integrating over the entire cluster, determine the total change in energy in the cluster stars (Binney & Tremaine, 1987)

$$\Delta E_{\text{total}} = \frac{M_C}{3} r_h^2 \left(\frac{2GM_P}{b^2 v}\right) \tag{2.33}$$

The timescale for this process to disrupt a cluster is of the order for this change in energy to exceed the binding energy of the cluster

$$t_{\rm SH} \sim \nu_{\rm encounters}^{-1} \frac{E_{\rm binding}}{\Delta E_{\rm total}}$$
 (2.34)

For shocks from the galaxy disk (q.v. Spitzer, 1987; Ostriker et al., 1972; Fall & Zhang, 2001)

$$t_{\rm SH} = \frac{3}{20} \frac{GM_C P_C v_Z^2}{r_h^3 g_m^2} \tag{2.35}$$

where  $P_C$  is the orbital period of the cluster around the galaxy,  $v_Z$  is the cluster velocity as it passes through the plane of the disk, and  $g_m$  is the maximum gravitational acceleration experienced by the cluster. For Milky Way clusters, this gives a timescale on the order of  $t_{\rm SH}\sim 6\times 10^9 {\rm yr}$ . With this dissolution timescale, we can

write the mass loss rate as (Fall & Zhang, 2001)

$$\nu_{\rm SH} = \frac{7}{3} \frac{\kappa_{\rm S} \bar{A}}{t_{\rm SH}} \tag{2.36}$$

where the factor of  $\frac{7}{3}\bar{A}$  accounts for corrections to the simple treatment of the derivation using the impulse approximation, and  $\kappa_S$  is the constant relating how much mass is lost for a given change in cluster energy

$$\frac{\dot{M}}{M} = \kappa_{\rm S} \frac{\dot{E}}{E}$$

This directly gives the relation

$$\frac{dM}{dt} = \nu_{\rm SH} M \tag{2.37}$$

As before with stellar evolution, this form has an exponential solution, which again yields evolution that does not change the shape of the mass function, but only shifts the normalization over time.

#### 2.3.4 Two-Body Relaxation

The final mass loss process and generally the most important is evaporation from the cluster due to two body relaxation. In the dense stellar environments of globular clusters, there will be many interactions between the stars, which serves to turn the velocity distribution into a Maxwellian. However, the high velocity tail of this distribution will ensure that some stars in the cluster will have velocities that will move them beyond the tidal radius of the cluster, at which point they will be lost to the host galaxy.

This mass loss must then have a timescale related to the time needed for the cluster to achieve a Maxwellian velocity distribution. This is the definition of the

relaxation time, which we can write as

$$t_r = \frac{v^2}{\langle (\Delta v)_{\parallel}^2 \rangle} \tag{2.38}$$

where  $v^2$  is the is kinetic energy per mass for a star, and  $\langle (\Delta v)_{\parallel}^2 \rangle$  is the average change of this energy per unit time. These quantities can be found by solving the Fokker-Planck approximation for the cluster (Spitzer, 1987; Binney & Tremaine, 1987), yielding a relaxation time:

$$t_r = 0.065 \frac{v^3}{nm^2G^2 \ln \Lambda} \tag{2.39}$$

Generally for a globular cluster, the important timescale is the relaxation time within the half mass radius. In this case  $n=\frac{1}{2}\frac{M}{m_{\star}}\frac{1}{V}=\frac{3}{8\pi}\frac{M}{mr_h^3}$ , and assuming the velocities are circular

$$t_r \propto \frac{M^{1/2} r_h^{3/2}}{mG^{1/2} \ln \Lambda}$$
 (2.40)

From the virial theorem, we know that the kinetic energy of the stars in the cluster is equal to half the cluster potential energy. This leads to the conclusion that the escape velocity is only twice the average velocity of a star in the cluster. If we determine how many stars have such velocities over the course of a relaxation time, we can also find the expected mass loss rate:

$$\nu_{\rm ev} = \frac{\xi_e}{t_r} \tag{2.41}$$

where  $\xi_e$  is the probability that a star with escape velocity is able to reach the edge of the cluster before being scattered back to a lower velocity. Following Spitzer (1987)

$$\xi_e = \frac{4\pi}{n_f} \int_{2v_m}^{\infty} f(v)v^2 dv = \frac{4}{\pi^{1/2}} \int_{2.45}^{\infty} e^{-x^2} x^2 dx$$
 (2.42)

which gives an estimate of  $\xi_e \sim 7.4 \times 10^{-3}$ , within an order of magnitude of the value

of  $\xi_e = 0.045$  given by more detailed evaluation with realistic mass distributions for the stars (Hénon, 1961). This gives a mass loss rate of (Fall & Zhang, 2001)

$$\nu_{\rm ev} = \frac{7.25\xi_e m G^{1/2} \ln \Lambda}{M^{1/2} r_h^{3/2}} \tag{2.43}$$

Substituting in the mean cluster density  $\bar{\rho}$ , which we assume to be constant over the lifetime of the cluster, we find

$$\nu_{\text{ev}} = k\xi_e \, (G\bar{\rho})^{1/2} \, m \ln \Lambda M^{-1} \tag{2.44}$$

and a mass loss equation

$$\frac{dM}{dt} = -\nu_{\rm ev}M\tag{2.45}$$

$$= k\xi_e (G\bar{\rho})^{1/2} m \ln \Lambda \tag{2.46}$$

As this mass loss is independent of mass, the solution is a linear decay, where

$$M(t) = M_0 - \mu_{ev}t (2.47)$$

This is a different form for the mass loss than for stellar evolution and shocks. It gives an amount of mass lost per unit time that is independent of the cluster mass and constant in time. Because of this, small clusters will be completely destroyed due to evaporation long before the heaviest clusters have lost even a fraction of their mass. Such mass loss has the effect of quickly depleting the mass function at low mass. After time t, we would expect that all clusters with initial mass  $M_0 < \mu_{ev}t$  to have been fully disrupted. This does not mean, however, that no clusters lower than this will be found. These new low mass clusters will be the remnants of more massive clusters that have also lost mass through evaporation.

# 2.4 Observed Properties of Globular Clusters

The structure of globular clusters is defined in terms of the central potential  $W_0$ . This parameter is not however, how the structure is generally defined based on observations. Instead, the King model concentration is used in its place, and is defined based on the two main lengths for the cluster

$$c = \log_{10} \left( \frac{r_t}{r_c} \right) \tag{2.48}$$

Figure 2.2 shows that c can be used as a replacement for  $W_0$ .

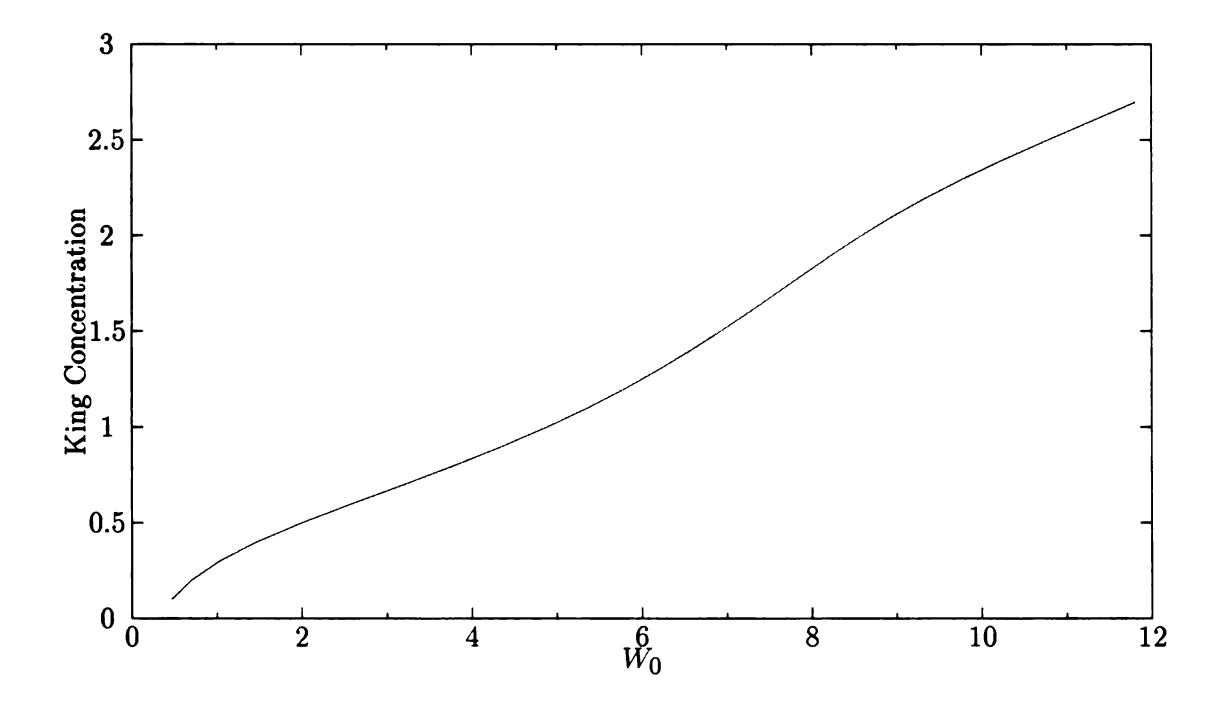


Figure 2.2 Comparison of the central potential  $W_0$  with the observable concentration c.

The half mass radius  $r_{hm}$  is another commonly measured quantity is defined as the radius that contains half of the total mass of the cluster. As the mass is generally an inferred parameter based on the surface brightness, the half light radius,  $R_h$  is often used in its place. This radius contains one half of the total flux of the cluster,

and can be used as a suitable substitute for the half mass radius. Both of these radii are larger than the core radii for most clusters.

A variety of photometric parameters can also be defined to quantify the flux normalization. The most common of these is the central surface brightness,  $\mu_0$  For most observations, this is difficult to measure accurately, as it requires a fit to the surface brightness profile, which is then extrapolated to zero radius. Therefore, it is often replaced with the average surface brightness within the half light radius, which is more easily measured. The equation for this is simply

$$\langle \mu \rangle_h = V + 2.5 \log_{10} \left( 2\pi R_h^2 \right)$$
 (2.49)

The central surface brightness can be used to find the central luminosity and mass densities. Converting the central surface brightness in magnitudes into a luminosity surface density (in  $\frac{L_{V,\odot}}{\text{pc}^2}$ ) is reasonably straight forward

$$\log_{10}(\Sigma_0) = 0.4(26.362 - \mu_V(0)) \tag{2.50}$$

which can be used to determine the luminosity density in the center of the cluster:

$$j_0 = \frac{\Sigma_0}{r_c p} \tag{2.51}$$

In this case, p is a function of the King model that determines how much of the surface luminosity is contributed from the core, and how much arises from the projection. This can be calculated from the King model by taking

$$p \sim \int_0^{r_c} \Sigma(r) dA / \int_0^{r_c} \rho(r) dV \tag{2.52}$$

Converting this central luminosity density into a mass density is just a simple multi-

plication by the mass to light ratio:

$$\rho_0 = \Upsilon j_0 \tag{2.53}$$

The relaxation time is the main timescale for the evolution of the cluster. At the core of the cluster, the relaxation time is defined as (equation 2.3.4)

$$t_{rc} = 1.491 \times 10^7 \frac{k}{\ln \Lambda} \langle m_{\star} \rangle^{-1} \rho_0^{1/2} r_c^3 \tag{2.54}$$

$$= 2.5013 \times 10^7 \rho_0^{1/2} r_c^3 \left( \ln \left( \frac{4}{30} M \right) \right)^{-1} \text{yr}$$
 (2.55)

This timescale often overestimates the evolution, so the half mass relaxation time is generally used instead. This time is

$$t_{rh} = 8.933 \times 10^5 \frac{1}{\ln \Lambda} \langle m_{\star} \rangle^{-1} M^{1/2} r_h^{3/2} \tag{2.56}$$

$$= 2.6799 \times 10^{6} M^{1/2} r_h^{3/2} \left( \ln \left( \frac{4}{30} M \right) \right)^{-1} \text{yr}$$
 (2.57)

Finally, the metallicity of globular clusters can be estimated reasonably well from the photometric color. This relationship is defined based on the known metallicities and colors from the Milky Way clusters, and is usually written in the form (Kundu et al., 1999):

$$[Fe/H] = -5.89 + 4.72 (V - I)$$
 (2.58)

As globular clusters have colors around  $V-I\sim 1.0$ , they have metallicities around [Fe/H]  $\sim -1.2$ , illustrating that globular clusters are more metal poor than the sun, which is to be expected based on their ages.

# CHAPTER 3: POINT SPREAD FUNCTIONS

At the distance of M87, the projected sizes of globular clusters are similar to the resolving limit of HST. Because of this, we have to account for the effects of the point spread function,  $\Pi$ . The point spread function (hereafter PSF) defines how the light of a point source (such as a star at great distance) is spread over the focal plane of the telescope by diffraction.

In the simplest model, we can consider a telescope as simply a circular aperture separated from the focal plane by a distance  $r_0$ . If we only allow monochromatic light of wavelength  $\lambda_0$  to pass through the aperture, then we can model the light as it passes through the aperture as a series of spherical wavefronts. This yields an image amplitude of

$$E = \iint_{\text{Aperture}} \frac{E_0}{r} e^{i(kr - \omega t)} dA \tag{3.1}$$

For the circular aperture, we can break the integral into strips of dA = xdy where  $x = 2\sqrt{R^2 - y^2}$ . Since the difference in amplitude due to diffraction is related to the differences in path length between all contributions, we can rewrite the equation of the spherical wave at a given time to explicitly contain this difference in path length  $kr - \omega t = yk\sin\theta$ . Performing the integration, and making further substitutions

 $v = \frac{y}{R}$  and  $\gamma = kR\sin\theta$ 

$$E = \frac{2E_0R^2}{r_0} \int_{-1}^{1} e^{i\gamma v} \sqrt{1 - v^2} dv$$

$$= \frac{2\pi E_0R^2}{r_0} \frac{J_1(\gamma)}{\gamma}$$
(3.2)

where  $J_1(x)$  is the first Bessel function. The final image intensity is the square of this, so

$$I = I_0 \left( \frac{J_1(kR\sin\theta)}{kR\sin\theta} \right)^2 \tag{3.3}$$

which is the definition of the Airy disk.

We can compare this simple model to the known properties of HST by noting that the core size of the PSF for visible light is roughly 0'.05. The first minimum of the Airy disk occurs when  $2R\sin\theta=1.22\lambda_0$ . Setting  $\lambda_0=555$ nm and R=1.2m, we find that this gives a size  $\theta\sim0'.058$ , showing that the HST PSF is dominated by the diffraction effects of the telescope aperture. Figure 3.1 shows a comparison between highly sampled HST PSFs for the F814W filter, and an Airy disk generated at the peak wavelength of this filter  $\lambda=814$ nm.

The extra structure that is visible in the real HST PSF shows that real PSFs are composed of more than a single simple diffraction pattern. It is clear from inspection of the formula above that the effect of diffraction is a Fourier transform of the aperture. The optical path of HST contains many more elements than a simple circular opening, such as support structures, and the "spider" that holds the secondary mirror. The addition of these objects creates the added complexity that is seen in the final PSF.

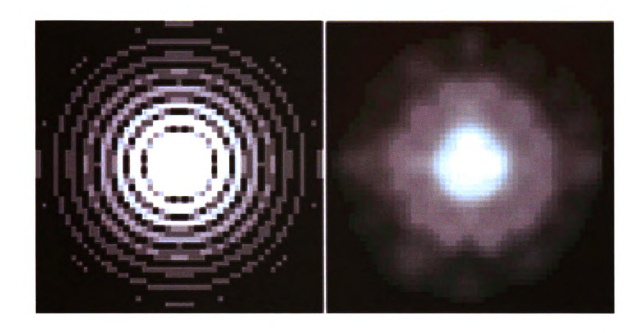


Figure 3.1 Comparison of the Airy disk for a circular aperture comparable in size to the HST to a highly sampled real HST PSF. This PSF is generated for the F814W filter with the Airy disk created for the peak wavelength of that filter. The first zero of the Airy disk clearly correlates to the size of the central core of the true PSF.

# 3.1 PIXEL RESPONSE FUNCTIONS AND THE EFFECTIVE PSF

A further complication in modeling the PSF arises from the fact that the focal plane of the telescope is not a perfect imaging plane, but rather an array of sensors that make up the CCD imager. For an ideal CCD, the measured image of a point source would be equivalent to

$$I(i,j) = \Pi(x,y) \otimes \coprod (i,j)$$
 (3.4)

where III is the Shah function, a regular grid of impulse functions. Due to imperfections in the production of CCDs, pixels do not fully sample light equally well when that light is centered differently. If we define the pixel response function  $\mathscr{R}$  as the sensitivity function of a given pixel over its surface, then the actual detected image will be

$$I(i,j) = \Pi(x,y) \otimes \mathcal{R}(x,y) \otimes \coprod (i,j)$$
 (3.5)

The pixel response represents the changes in the detection efficiency of a given pixel when light is incident on different portions of the pixel. One of the main sources of this is due to the finite thickness of the detector material, and the fact that that material does not absorb photons with 100% efficiency. This leads to internal reflections off the back surface of the detector, which in turn causes the light to be scattered into neighboring pixels. Assuming this scattering is uniform, a point source centered near a pixel edge will have fewer photons detected in the incident pixel compared with a source at the pixel center. The individual pixels in the detector are also not perfectly electrically isolated from each other. This can allow captured photons (now present as a charge in the detector) to bleed into neighboring pixels. This adds a further contribution to  $\mathscr{R}$ .

Since we can never truly observe the real PSF, but only the convolution of the PSF and  $\mathcal{R}$ , we can define a new function  $\Pi_{\text{eff}}$ , the effective PSF as

$$\Pi_{\text{eff}} = \Pi \otimes \mathcal{R} \tag{3.6}$$

By defining this, we now have a function that works as the standard PSF would in a continuous focal plane. The effective PSF must be smoother and broader than the instrumental PSF, as it convolved with  $\mathcal{R}$ , which has a width similar to the size of a pixel. However, by switching to  $\Pi_{\text{eff}}$ , we no longer need to worry about integrating over the surface of a pixel, as that integration is incorporated already.

# 3.2 PSFs for Extended Objects

We have defined the PSF so far in terms of the effect of diffraction on a point object. For extended objects, the relations are largely the same. For a point source, the pixel phase (where the center of the PSF falls in the pixel) changes the flux significantly. This is not necessarily the case for extended objects, as the fact that the illumination covers the entire pixel reduces the effect of the pixel phase. If we assume that the pixel is illuminated by roughly the same flux across its entire surface, then the PSF for an extended object can be evaluated by simply evaluating the  $\Pi_{eff}$  at the center of the pixel. As the light distribution becomes less flat across the pixel, the PSF shifts to the location of the peak of the flux. However, this will smoothly shift to the point like case if the distribution becomes significantly peaked.

# 3.3 EVALUATING THE PSF FOR HST

Since we need the PSFs for HST to accurately model the detected GCs, we can take advantage of the fact that being in space makes the PSF generally stable with time. For ground based observatories, motions of the atmosphere can significantly change the width of the PSF. These motions create a PSF that is much larger than the aperture diffraction pattern. For ground based observations, the PSF can then be assumed to be of the form

$$\Pi_{\text{ground}} = \Pi_{\text{eff}} \otimes e^{-(x^2 + y^2)/2\sigma_{\text{atm}}}$$
 (3.7)

where  $\sigma_{\text{atm}}$  is of the order of 1", almost certainly larger than  $\Pi_{\text{eff}}$ . By being in space, HST does not have this added convolution, and so depends only on the telescope itself, which leads to consistent modeling of the PSF. Creating such a model for the PSF is essential for HST, as many pointings do not have sufficient stars to create one directly from the observation.

### 3.3.1 TINYTIM

TinyTim (Krist, 1993) is a program that is designed to model the PSF for HST. It takes a theoretical model of the telescope aperture and obstructions, and uses Fourier Transforms to directly estimate the shape of the PSF. It incorporates the expected object spectrum and the filter response to determine the relative contributions for all wavelengths. The pixel response of the detector is added as a convolution at the end of the evaluation.

This program works well for WFPC/2, and is the standard method for generating PSFs for this instrument. However, the ACS detector is far off the central axis of the telescope, and as such, has serious geometric distortion. The standard correction for this distortion is to use Drizzle (see section 4.1.2 for details) to correct the ACS frames. As the parameters that govern this procedure can change, the default Tiny-Tim distortion correction does not in general provide a PSF that accurately represents what is actually observed by the detector.

#### 3.3.2 EMPIRICAL PSFS

To resolve this problem of poorly modeled PSFs, Anderson & King (2006) took the tactic of empirically measuring the PSFs. To do this, they used 126 orbits of observations with HST to image the same field in the globular cluster NGC 6397. This field contained roughly 4000 stars, which were imaged at different rotations and shifts, to ensure that the stars do not fall on identical locations on every image. A model of the PSF was then created, and fit to the stars, yielding a position and flux for each star on each frame. These positions are then used to construct a model of the distortion for the detector. Finally, the true pixel values were used to update the model of the PSF. This process was iterated until a final solution was found. This iterative process is important, as asymmetries in the PSF can alter the measured centroid for the star, which will in turn yield a worse distortion model (Anderson & King, 2003).

The final result of this iterative process was an accurate distortion model, and a highly sampled  $\Pi_{\rm eff}$ . As there are 4000 stars on 126 images, each of which is roughly 10 pixels in radius, it is clear that this data provides millions of samples of the effective PSF. To eliminate changes in the PSF across the surface of the detector, the models were calibrated over different areas so that any changes in the PSF beyond the standard distortion corrections would be accounted for in the model.

This iterative process was repeated for a variety of filters, and then tabulated into reference images that contain highly sampled PSFs at a variety of positions across the image. By interpolating between the different PSFs, we can generate a high resolution PSF for any position on the detector, and then by interpolating that highly sampled PSF, we can make one for a given pixel phase. These PSFs are designed for the raw flat fielded and distorted "FLT" frames. This choice was made as this image is the most photometrically accurate, as it has had the least processing or resampling.

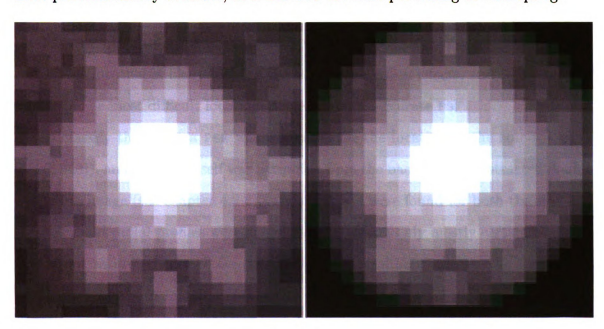


Figure 3.2 Comparison of TinyTim PSF to the Anderson & King (2006) empirical ACS PSF after applying the distortion correction. Although the general shapes are similar, the cores clearly differ, with the TinyTim PSF being more oblong than the empirical PSF.

# 3.4 PSF GENERATION

To generate PSFs for use in modeling the globular clusters, the individual data FLT frames were zeroed out, and the empirical PSFs were placed at the positions of globular clusters in the original data. The shifts between frames were included in this, such that the PSFs on each frame have slightly different pixel phases. This was done with the goal that once the frames were distortion corrected and aligned, all PSFs for a given position will also align. These PSF frames are then combined in the same way as the data, ensuring that the final PSFs are the most accurate representation of a point source in the data.

Quantifying the error in the final PSFs is very difficult, as there are few bright stars in the field. As M87 lies out of the plane of the Milky Way, this lack of stars is not surprising. Complicating the effect is the fact that one of the two obvious stars is saturated at the core, making it effectively useless in characterizing the quality of the PSFs we generate. The one remaining star is located at the edge of the bottom chip. This location is likely to have the largest distortion effects, and so is likely to be one of the most difficult locations to generate an accurate PSF.

To classify the error, a PSF was generated for the location of the star ((x,y) = (3995, 340)), and the star itself was extracted from the background subtracted double resolution image (see chapter 4.2.2). The centroids were found for both the star and the PSF, and radial profiles were generated. As we are only mostly certain that this star is not saturated, the choice was made to flux calibrate the PSF by forcing the profile at 5 pixels to match. This choice excludes the central peak, and calibrates based on the light in the second maximum. Once this was done, the star and flux calibrated PSF were interpolated to a common grid, and the percent error between the two was calculated as

$$E = \frac{\text{Star} - \text{PSF}}{\text{Star}} \tag{3.8}$$

Only the central  $20 \times 20$  pixels were checked, as beyond this point, the star image has dropped to less than 0.1% of the peak, and noise from the galaxy background begins to be the main source of light. Inside this box, the error is well described by a Gaussian with  $\langle E \rangle \sim 2\%$  and  $\sigma_E \sim 6\%$ . The error in the central pixel is 5% which suggests that this star is not in fact saturated.

This result is reasonable, as it is consistent with the nominal uncertainty in the empirical PSF. Anderson & King (2006) provide an error estimate of 5% for their empirical PSFs, in the case of no additional corrections beyond the tabulated grid. As their method of correction is based on doing a similar error analysis to this, but for multiple stars across the image, we are unable to apply their method to our data. These errors are used to construct a perturbation to the standard PSFs, which reduces the error by about a factor of two.

In addition to the simple errors, we can check that the PSF shape is correct. Although the star and PSF have nearly identical "bumps and wiggles," the PSF appears to have a slightly broader core than the star. Approximating the core of both with a Gaussian shows that the PSF is indeed  $\sim 0.15$  pixel broader in both directions ( $\sigma_x^{\rm star} = 1.64$ ,  $\sigma_x^{\rm PSF} = 1.80$ ,  $\sigma_y^{\rm star} = 1.71$ ,  $\sigma_y^{\rm PSF} = 1.85$ ). This error likely arises from some error in the placement of the PSFs onto the individual frames. In that coordinate system, this error transforms to an interframe scatter of about 0.08 pixel, a value which would not be surprising. One possible source of this scatter is from errors in the geometric distortion, which seems to account for the majority of this scatter ( $\sigma_{\rm distortion} \sim 0.05$  pixels, Meurer (2002)).

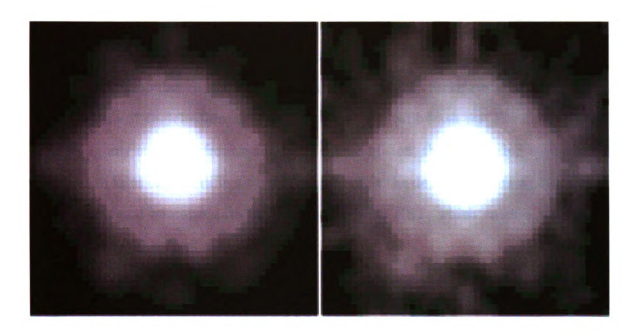


Figure 3.3 Comparison of final drizzled ACS PSF generated from the Anderson & King (2006) empirical PSFs to the star on the final drizzled data image. The PSF is made for the position of the star to ensure the distortion calculations match and that the different response across the detector are removed.

# CHAPTER 4: DATA REDUCTION

The data used for this project comes entirely from the Hubble Space Telescope. As discussed in Chapter 3, the PSF for ground based telescopes is much too wide for extragalactic globular clusters to be imaged accurately. Since we wish to measure the structure of the clusters, this added broadening will wash out the cluster light, preventing any structure from being visible. In addition, the broadening makes identification of faint objects difficult, which would limit the depth to which we can probe. Very high signal to noise data can be created with HST, which ensures that these faint objects will be well detected.

# 4.1 IMAGE COMBINATION

As HST is limited in the length of any single image by its orbit time, multiple short exposures must be taken to get the long total exposure times needed to achieve the required high signal to noise. Using multiple exposures of the same image also allows for problems on the image to be removed. Since the HST detectors are in space, they are much more susceptible to interference from cosmic rays, which can interact with the detector and show up as erroneous bright objects. However, as these cosmic rays are very unlikely to occur on the same pixels in all images, they can be easily removed by comparing the multiple frames. In addition, the effects of cosmic rays build up over the exposure, so a single long exposure will have more contamination from cosmic rays than a short exposure.

The HST detectors also have a number of bad pixels and bad columns, which do not correctly measure the light incident on them. The main cameras are also comprised of multiple detectors, which have gaps between them. By dithering the telescope pointing, the location of the scene on the detectors also changes, and both of these gaps in the data can be repaired using pixels from other images. The final benefit of multiple dithered images is that the data can be combined to yield higher resolution combined images than any of the original images. The creation of this higher resolution image requires that the dither include non-integer shifts. As we assume that the pixels of the detector sample the light distribution in some regular fashion, these fractional shifts sample the light in the intervening space. The simplest case is one in which four images are combined with relative shifts (0,0), (0.5,0.5), (0.5,0.5). Since these images sample the light regularly on a grid with twice the original image resolution, a new image can be created by interlacing the pixels together.

It is important to note that the construction of new higher resolution images has little effect on the angular size of the PSF. This new image in no way deconvolves the scene from the PSF, it merely samples the data better. This means that objects smaller than the PSF will remain unresolved in the new data. In addition, the very act of co-adding data tends to introduce further blurring, depending on the technique and sampling pattern used.

#### 4.1.1 Lauer Fourier Method

One method of recovering resolution from multiple frames is presented by Lauer (1999), using image combination in the Fourier domain to create a Nyquist sampled image. Briefly, this method expands each data image by interleaving blank pixels to pad the data to the final resolution. The Fourier transform of these images is taken, and multiplied by a phase factor to incorporate the interframe shifts. These transform

images each contain some information about the image at frequencies higher than the original sampling frequency. By summing these transform images the contributions from each dithered image can be incorporated to provide the best estimate for this high frequency information. The final combined image is then created by taking the inverse Fourier transform.

In the simple interlacing case as considered above, this method yields identical results. However, it can also yield reasonable estimates even when the sampling isn't ideal. Another benefit is that overconstrained sets of images can be combined in a least squares method to provide an image that deals with noise on the individual frames.

Although this method can accurately recreate the underlying scene, it has fairly strict data requirements. First, the input frames must be cleaned of all cosmic rays and errors, and must have any geometric distortion due to the instrument optics corrected. These requirements make it immediately difficult for dealing with ACS images, which have large distortion effects. Secondly, the input frames should fully sample the pixel phase space, otherwise, they will create biased images, that depend on the individual frames unevenly. These images may also contain aliases from Fourier domain "satellites," which can arise if the final Fourier transform image does not properly taper to zero at high frequency. Such satellites will create a blurring of the high frequency information, limiting the final resolution that can be created. Finally, there is no packaged form for this method, which prevents widespread adoption, despite its mathematical elegance.

#### 4.1.2 Drizzle

Another method commonly used to combine data is the Multidrizzle package in Pyraf (Koekemoer et al., 2002). Although less mathematically rigorous, it has much looser data requirements and is mostly automated. This process not only combines the

images, but also cleans image defects and corrects for the geometric distortion.

The Drizzle algorithm operates on the input images by first shrinking the pixels by a scale factor called the "pixfrac." This step holds the centers of the pixels fixed, but decreases the area, leaving gaps between the pixels. These shrunken pixels are then transformed via a geometric transformation onto the final image grid. The small pixels are then "drizzled" onto the final image by allowing the pixel values to be added to the output pixels in proportion to the area covered.

This addition to the output grid can be altered by changing the kernel used for the addition, with a "square" kernel simply adding the fraction based on the area of overlap, and a "Gaussian" kernel weighting the contribution from the center of the input pixel more than the edges. An important way to estimate the image is to use the "turbo" drizzle, which contributes all of the input pixel's light only on a point in the center.

After all the individual frames have been drizzled to the output image, a rescaling is done by normalizing against the weight in each pixel. Since all pixels are not guaranteed to have the same input area contributed to them, this rescaling is essential to ensure that the counts measured on all pixels have the same basis. If few images are used, this rescaling can add noise to the final image due to non-uniform weights.

Multidrizzle first reads the flags for each pixel in the raw flat fielded "FLT" images, and creates a set of masks for known bad pixels. The FLT images are then projected onto a common coordinate system via a "turbo" drizzle. The WCS from each image, plus an external correction supplied from a shiftfile, is used to create the transformation from the "FLT" to the "single\_sci." This step corrects the frames for geometric distortion, and removes the background offsets between images, ensuring the various frames have the same geometric and photometric calibration.

At this stage, the many "single\_sci" images represent multiple realizations of the true scene. However, cosmic rays and unknown image defects create deviations from

this true scene. We can use the fact that we have many images to remove these defects. A median image is created from the "single\_sci" images, with discrepant pixels clipped out. This median image is "blotted" back to the FLT frame for each image, to create "BLT" images, which are an expectation of what each raw FLT frame should look like.

Cosmic ray rejection is accomplished by comparing the FLT to the BLT images. To avoid improperly masking the bright peaks of real objects (which are most likely to have the largest scatter between individual images), the masking is weighted by a gradient image, in which each gradient pixel is set equal to the largest deviation between the neighbors in the FLT image. A pixel is then flagged as a cosmic ray if the difference between the FLT and the BLT exceeds:

$$|FLT - BLT| > \text{scale} \cdot \nabla_{FLT} + \frac{S}{N} \cdot \sigma_{\text{noise}}$$
 (4.1)

Errors in the image alignment and sky level can easily lead to improper masking of objects in the CR phase. If the shifts are incorrect, then the objects will be clipped from the median image, and hence will likely be flagged as cosmic rays. Errors in the sky level between frames can do the same, by limiting the number of images that truly contribute to the median image. Such an error can allow cosmic rays to slip through by being improperly excluded from the median image.

Once the cosmic rays are found, their locations are added to the static mask created earlier. This creates a final mask used for the final drizzle. This drizzle uses a more accurate "square" kernel with the pixfrac set to 0.7 to minimize the size of the final PSF. Each FLT is then drizzled onto the final "DRZ" image, with all bad pixels removed and the sky levels matched. The final DRZ image has an exposure time equal to the sum of the exposure times of the component FLTs. A weight file is also created that stores the exposure time sum that contributed to each pixel of the DRZ. The weight varies between pixels based on the effects of the distortion correction and

the number of frames contaminated by cosmic rays at that position. This weight is essential to gauge how well the shifts are calculated. In the case of poorly determined shifts, the locations of objects in the DRZ image are matched by lower values in the weight image, as the objects peaks will have been flagged as cosmic rays on the frames that have the worst shifts.

#### 4.1.3 Determining Shifts

Accurate interframe shifts are essential to ensure the highest quality final images. As bad pixels are masked by the Drizzle algorithm, based on flagging statistical outliers, having inconsistent shifts will skew these statistics.

The first step in measuring shifts is projecting all of the data frames onto distortion corrected frames. This projection mosaics the multiple chips together, and arranges the frames onto the same WCS. This can easily be accomplished by stopping Multidrizzle after the creation of the single\_sci images.

With the various frames drizzled to what should be a common frame, the errors between the frame WCS and the true sky WCS manifest as shifts in object coordinates between the corrected images. A first guess at the transformations needed to correct each image is created by manually identifying a pair of objects on each image. The images then have catalogs of objects created with Source Extractor (Bertin & Arnouts, 1996). The brightest objects (500 in this case) are extracted from these catalogs. The initial transformation is used to find matching objects, which are then used to refine the transformation by solving the least squares problem for each frame j at each matched point i:

$$X_{\text{reference }i} - X_{0j} = S_j \left( \cos \theta_j x_{ji} + \sin \theta_j y_{ji} \right)$$
$$Y_{\text{reference }i} - Y_{0j} = S_j \left( \cos \theta_j y_{ji} - \sin \theta_j x_{ji} \right)$$

As the transformation is improved, more matches will be found, so this is iterated until the transformation for each frame converges.

With accurate shifts calculated, we next need to calculate correct sky background levels. These values are calculated by the calibration process based on the distribution of image pixel values. Large features (such as the galaxy itself in our data) will skew this distribution, and tend to overestimate the background level. The individual FLT images are drizzled into single\_sci frames again, incorporating the new shifts. Empty regions of the images are found, and then the median in a box  $100 \times 100$  pixels is taken. Each image then has the median deviation from all boxes calculated, after subtracting the minimum from all images. This median is written to the FLT image header, to be subtracted during the final run of multidrizzle.

# 4.2 Data Summary

The data used for this thesis come from two sets of many orbit observations of the galaxy M87. The data were taken as part of an initial microlensing survey with the WFPC/2, and again in a followup survey with the ACS. In order to measure these microlensing events, they must be monitored over their light curves. This requires a time series of data taken fairly regularly. For our purposes of creating very deep images, we can ignore any slight changes due to this microlensing, and simply combine all the images together into very deep exposures.

# 4.2.1 WFPC/2

The data for the original microlensing survey were combined by Tod Lauer, using his optimal Fourier method. Superimages for each of the four detectors on WFPC/2 were created. These data were taken in two filters, the F606W (a V filter, with peak wavelength at  $\lambda = 606$ nm) and F814W (an I filter, peak wavelength  $\lambda = 814$ nm), with total exposure time  $t_V = 11600$ s and  $t_I = 30160$ s.

These data were used to design and test the methods for detection on such deep images. A very deep luminosity function was created for the globular clusters (Waters et al., 2006). However, difficulties in constraining the PSF prevented reliable structure fitting. Conveniently, the followup ACS data were taken at this time, and the project switched to use the new data.

# 4.2.2 ACS

The followup data came from a 50 orbit series of observations with the ACS. The images are of the core of the giant elliptical galaxy M87, extending out to a projected radius of 8 kpc. The data were taken over the course of a three month search for microlensing events, which need multiple exposures to look for the changes in brightness. This arrangement yields data that can be combined into single very deep exposures.

The same two filters were used for this project as for the WFPC/2 survey: F606W and F814W. On each observing day, four exposures in F814W were taken with slight pointing offsets to provide for full image sampling every day. This was done as F814W was the primary filter used for the microlensing search. These exposures are matched by a single exposure in F606W, which are dithered over the different days, providing a full sampling of the image plane over the entire set of observations.

In all, 49 F606W and 205 F814W images were combined to yield final images with exposure times of  $t_V = 24500$ s and  $t_I = 73800$ s, making these some of the deepest images ever taken with HST. In addition to these exposures, 8 exposures in F606W and 13 in F814W were taken but excluded due to a loss of the telescope pointing. The main images were combined to a resolution of 0'.045 pixel<sup>-1</sup>, the nominal resolution of ACS. These images therefore have the highest signal to noise possible. A second set of images were combined at twice this resolution, 0'.025 pixel<sup>-1</sup>, for use in modeling the clusters. These higher resolution images are useful as they provide a better view of the cluster structure.

### 4.3 IMAGE PREPARATION

Given that the final combined exposure times make the final images among the deepest ever taken with HST, we have an excellent opportunity to measure the globular cluster luminosity function fainter than has been done before for any other galaxy. In order to take advantage of this depth, however, we need to first prepare the images to ensure that objects are detected with the best possible efficiency. This preparation mainly involves the removal of the galaxy light. If the galaxy were not removed from the image, then the photometry of the clusters would be biased by the addition of extra signal from the galaxy.

Subtracting the galaxy from the image is essential in another way as well. The detection threshold is defined in terms of the image noise. This constant threshold works fine for images with uniform noise, such as a sparse field of stars, but for these images with their strongly varying noise distribution, the threshold needs to be defined better. This variable noise arises from the fact that the brightness of any given pixel is dependent on the number of stars that fall within that pixel. This is a Poissonian distributed quantity, so the noise due to the galaxy scales as the square root of the galaxy brightness. The center of the galaxy is thus a much noisier region of the image than the edges, and so using a fixed detection threshold will miss many real objects at the edges, and count too many noise spikes in the core. With an accurate model of the galaxy flux, the detection threshold can be weighted to ensure equal detection efficiency across the image.

The model of the galaxy light must not be biased by any objects on the image, and must handle the steep changes near the core of the galaxy. There are two common methods used for removing galaxies, unsharp masking and isophote fitting. Unfortunately, both of these techniques have failings, and so a hybrid method was developed to ensure the best quality subtraction possible.

#### 4.3.1 Unsharp Masking

The unsharp masking method estimates the galaxy light by smoothing the image so as to remove the contributions from small scale objects. A simple Gaussian filter will not work to accomplish this, as any final image will still contain the flux from all of the small objects, just smeared out onto a larger scale. Instead, a median filter is used, as this can ignore the bulk of the light from these objects. The quality can be increased by clipping the highest and lowest pixels from the box before the median is taken. As the main objects found on the image are mainly globular clusters, we can choose a box size larger than the expected sizes of these objects. This consideration leads to the choice of a box  $100 \times 100$  pixels in size.

Two main issues arise from this fitting method. First as each pixel in the final image is calculated a different filter box, adjacent pixels may not have smoothly changing values. Although the majority of pixels in the filter box will remain the same, there can be sufficient changes to significantly change the output values. This effect will increase as the image noise increases, to the point where the galaxy subtraction may actually increase the final image noise. Secondly, bright objects can skew the median, even if the brightest pixels are excluded. This effect will cause the unsharp masked image to oversubtract around any bright objects on the image. It also influences how the core of the galaxy is subtracted, where the steep galaxy profile skews the median to lower values. This prevents the core from being correctly modeled, and it will show up as undersubtracted. Figure 4.5 shows the results of unsharp masking on the final combined F814W image. These defects in the method can be clearly seen, with the most obvious oversubtraction occurring around the spiral galaxy at the bottom of the frame.

#### 4.3.2 ISOPHOTE FITTING

The ELLIPSE routine in IRAF is commonly used for modeling the light distribution of galaxies. It fits the galaxy as a series of concentric elliptical sophotes, allowing the ellipticity, orientation, and center to vary with radius. This method has the benefit then that all adjacent pixels represent similar points on a smoothly changing model, which should reduce the noise in the fit. As it fits the values based on only pixels which match an isophote, it is able to generate a model that accurately accounts for the steep gradient in the galaxy core. This method can be biased by objects on the image, but as an isophote is generally fit using many pixels, only objects that take up a significant fraction of the isophote will have much influence. Such objects can be masked out, which helps remove this problem.

Unfortunately, the isophote fitting can create odd artifacts at radii where EL-LIPSE has determined the ellipticity has changed. This leads to small "waves" where the galaxy light is only partially subtracted, often with matching areas of oversubtraction on the opposite side of the center. Finally, the ELLIPSE algorithm requires the isophotes have full angular sampling. This is not true at the largest radii, as the square image prevents such sampling. As the algorithm stops when this sampling is not possible, the corners of the image have no fitting done, and hence no subtraction. Figure 4.6 shows the results of ELLIPSE on the F814W image, illustrating these problems.

#### 4.3.3 FINAL METHOD

The solution to the difficulties presented is to use a hybrid of these methods. The image is first scanned by a large box ( $100 \times 100$  pixels) and the pixel statistics calculated within the box. All pixels  $4\sigma$  higher or lower than the box median are flagged, and the statistics recalculated without them until no more pixels are being flagged. The box is shifted by half its width, and the process repeated to create a mask that

řeá(

contains all real objects on the image. Since the data region of the final DRZ image is smaller than the total image, the empty regions created by distortion correction are also flagged on the mask file.

With a reliable mask created, ELLIPSE is used to find a model for the galaxy. The fitting algorithm used by ELLIPSE only allows this to work out to a radius where a full isophote can be constructed. To fill the regions that are not modeled, we assume that the ellipticity and position angle are fixed at the values of the last fitted isophote. Incomplete isophotes are then constructed by taking the median values in annuli of increasing semi-major axis. This extends the fit to cover the entire image.

Although the galaxy model created by ELLIPSE does an excellent job of removing the majority of the galaxy signal, especially in the sharply peaked core, it still leaves the small "waves" in the final image. These waves are removed by generating a new mask from the ELLIPSE subtracted image, and then sampling the image with a wide median filter and constructing a bicubic spline model between these sampled points. This spline model is then evaluated across the image, and that difference removed. With the waves removed, we are left with an image that is fully cleaned of the galaxy. The final step of the image preparation is the removal of any remaining constant background offset. This is done by subtracting the mode of the image intensity histograms from the image. The final mode subtracted histograms are shown in figure 4.7. The pixel distribution is asymmetric in the galaxy subtracted images, which is not entirely surprising, as the real objects on the frame should increase the number of pixels with positive values. The final galaxy subtracted F814W image is shown in figure 4.8, which shows the clear improvement over the other methods.

The output of this filtering is saved as the "data" image, which has had the galaxy light subtracted off, and is used for all subsequent analysis. The "background" image is the final galaxy model, and the "noise" image is the galaxy model plus the fixed read noise for our data. This image is used as the weight for the detection routine.

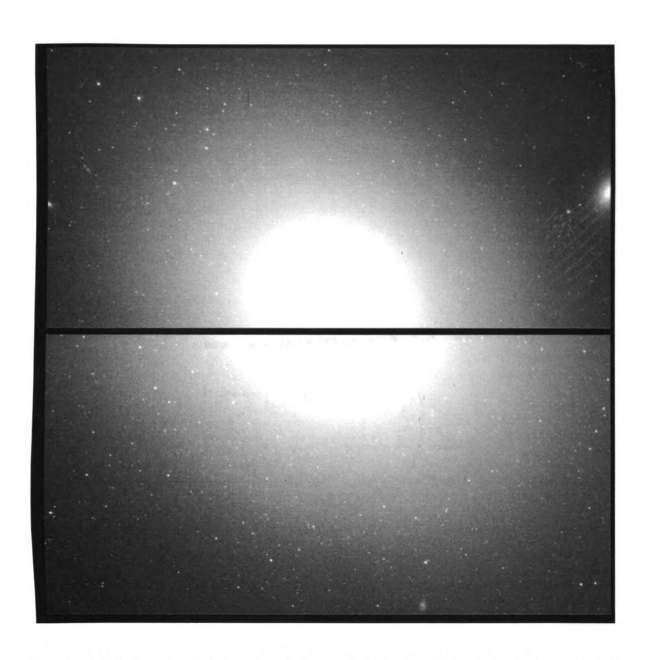


Figure 4.1 Original F606W raw FLT frame before reduction. Cosmic rays can be seen, such as the feature between the bright GC and the companion galaxy on the right edge.

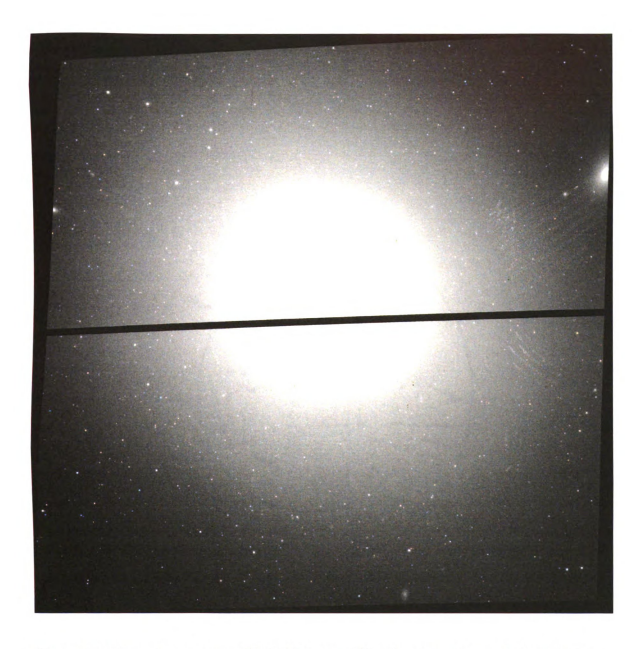


Figure 4.2 Distortion corrected F606W frame. The rhombus shape of the ACS detector footprint can be clearly seen as a result of distortion correction.

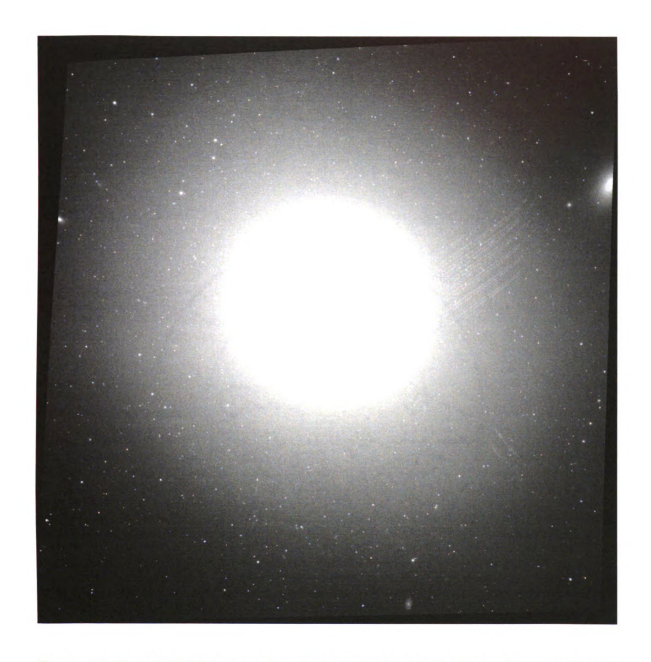


Figure 4.3 Final F606W image after combining with Multidrizzle. The cosmic rays have been eliminated from this image, and the interchip gap has been filled with data from other frames.



Figure 4.4 Final F814W image after combining with Multidrizzle.

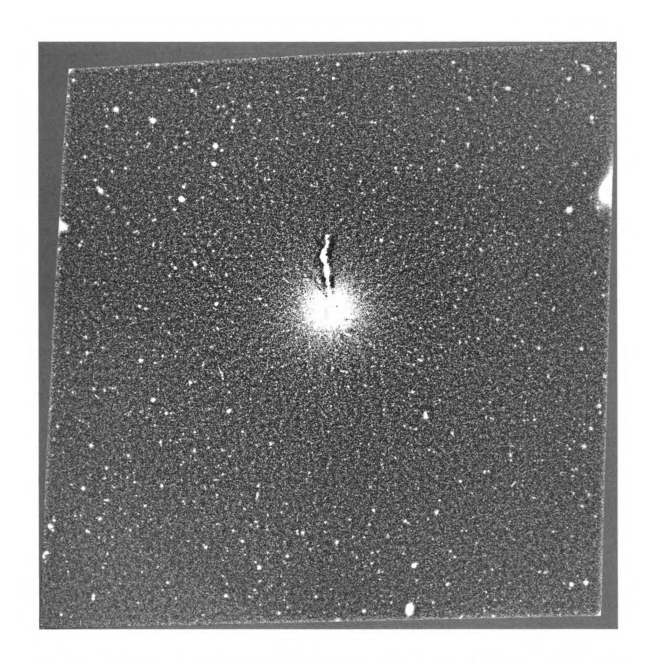


Figure 4.5 Subtraction of galaxy light using unsharp masking, with a  $100 \times 100$  pixel box. Although it creates a generally smooth image, the fringing effects can be seen at the eges of the data, as well as in the oversubtraction that surrounds bright objects. The sharp rise toward the galaxy core skews the median filter, which prevents pixels within a box that contains the very center of the galaxy from being correctly subtracted

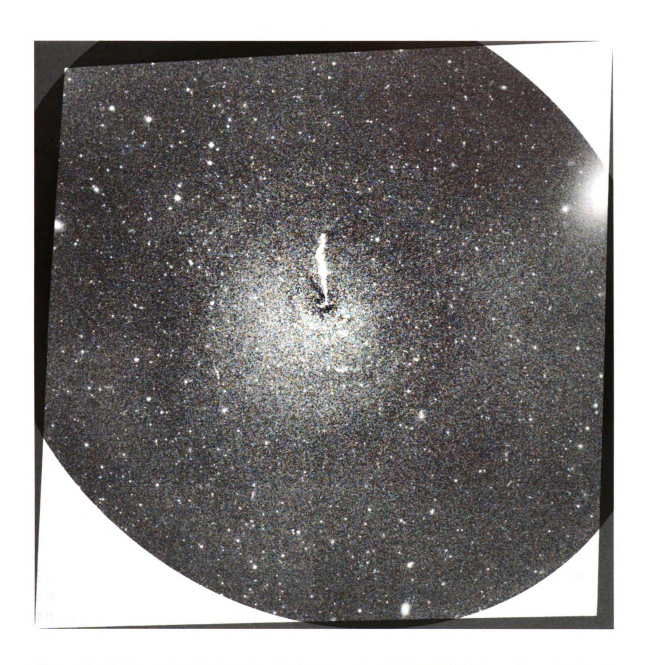


Figure 4.6 Subtraction of the galaxy light using the IRAF ELLIPSE routine. Although the core of the galaxy shows much improvement (illustrated by the fact that the central dust lanes can now be seen), the two main failures are also visible. The corners of the image show where ELLIPSE has stopped fitting, and the unevenness around the core shows where the isophotes have failed to correctly match the galaxy's true ellipticity.

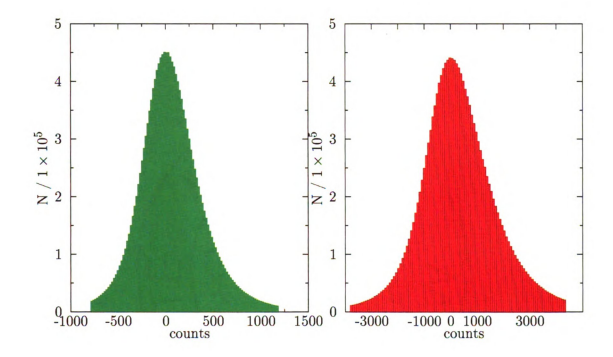


Figure 4.7 Image histograms for the F606W and F814W images. The centering about zero indicates the background subtraction has correctly removed the galaxy light. The asymmetry points out that these images contain real objects that are not subtracted by the galaxy removal.



Figure 4.8 Final galaxy cleaned image. Although some artifacts of the galaxy subtraction process can be found (such as around the companion galaxies), a clear improvement is evident over the simpler methods. This image also shows that the noise remaining after galaxy subtraction increases towards the center of the galaxy.

# CHAPTER 5: GLOBULAR CLUSTER LUMINOSITY FUNCTION

## 5.1 OBJECT DETECTION

Source Extractor (Bertin & Arnouts, 1996) was used to generate a database of objects. The galaxy subtracted "data" images were used as the search images, and the galaxy model was used to weight the detection process. By default, Source Extractor looks for objects a specified number of standard deviations above the background, taking the statistics across the entire image. As the noise in this data is highly dependent on the galaxy flux, this method does not work uniformly across the image. By supplying a weight image, however, Source Extractor scales the detection threshold across the image to reflect how the image noise truly behaves.

For this project, a detection threshold of  $3\sigma$  was used, with a minimum area of 2 pixels. This area criterion requires that an object must satisfy the threshold on at least two adjacent pixels, and helps to keep noise spikes from being detected as real objects. We also set the requirement that an object must be detected at this threshold on both the F606W and F814W frames. By requiring all objects be found in both filters, we reject any unusual features that appear in only one. Table 5.1 lists the quantities directly measured by Source Extractor for each detected object.

Table 5.1: Quantities measured for each object in both filters by Source Extractor.

Description	Units	
(X,Y)	position on data image	pixels
$(lpha,\!\delta)$	position in the sky (2000 epoch)	degrees
$m_i$	apparent magnitude within a fixed radius	mag
$\Delta m_i$	error in the apparent magnitudes	mag
threshold	local detection threshold	counts
background	local background level	counts
$F_{ m max}$	maximum flux value	counts
$F_{ m iso}$	total flux above detection threshold	counts
$A_{ m iso}$	area above detection threshold	pixels
$\mu_{ ext{threshold}}$	surface brightness at the threshold detection level	$mag / arcsec^2$
$\mu_{ ext{max}}$	surface brightness at object peak	$mag / arcsec^2$
$A_{j}$	area at isophotal levels: $I_j = \text{threshold} \cdot \left(\frac{F_{\text{max}}}{\text{threshold}}\right)^{j/8}$	pixels
flags	any internal flags about measurement problems	•••
FWHM	full width at half maximum	pixels
stellarity	classification ranging from one (star) to zero (galaxy)	•••
$r_{1/2}$	radius containing half of $F_{iso}$	pixels
$A_E$	major axis length	pixels
$B_E$	minor axis length	pixels
$ heta_E$	position angle of major axis	degrees
elongation	$rac{A_E}{B_E}$	
ellipticity	$1-rac{B_E}{A_E}$	
$d_{ m merge}$	distance between V and I image centroids	arcsec
$R_{ m gal}$	projected distance to galaxy center	arcsec

#### 5.1.1 Instrumental Magnitudes

Source Extractor automatically converts the raw fluxes to instrumental magnitudes, using the photometric zeropoints for the individual filters supplied. This zeropoint is also modified by the exposure time of the image, so the instrumental magnitude is defined as

$$m = -2.5 \log_{10}(F) + 2.5 \log_{10}(t_{exp}) + \text{Zeropoint}$$
 (5.1)

The zeropoint is listed in the calibration manuals for the individual detectors, and is reasonably well calibrated.

Unfortunately, this instrumental magnitude only measures the light within the apertures defined. A single aperture clearly does not fully account for all the cluster light, requiring a more complete study of the photometry.

# 5.2 Completeness Correction

Even though we have set the detection threshold fairly liberally, and have extraordinarily deep data, we still expect that we are not likely to be 100% efficient at detecting objects. The best way to quantify this detection efficiency is to add simulated clusters to the images, and then check to see how many of these are detected by searching with Source Extractor and the same detection limits.

Since the detectability of any given object is related to the surface brightness, and not just the total object flux, we must also incorporate the sizes of the objects. Simulated globular clusters with a fixed central potential of  $W_0 = 5$  (King c = 1.03) were generated for a grid of apparent instrumental magnitudes and tidal radii. At each grid point, 200 simulated clusters were randomly added to the background subtracted images. The detection and measurement was repeated as was done for the real data with each simulated cluster stored along with the values of the parameters calculated by Source Extractor.

Once this is finished, all objects at a given grid point are analyzed, and the ratio of the number found to the number input is calculated. Due to some significant objects that remain on the image after galaxy subtraction (most notably the central jet and the companion galaxy), some regions of the image are manually excluded, which changes the input number between grid points.

Figure 5.1 shows the completeness surfaces for the two filters. Over the range of tidal radii that we expect to find globular clusters, the size dependence of the completeness is fairly weak, so for all further analysis, we define the completeness solely as a function of apparent instrumental magnitude. Due to the radial dependence of the galaxy noise, the detection efficiency changes with distance from the core. To minimize the scatter in the completeness, we divide the data into two radial bins, breaking at the median cluster distance 68″.95. The final completeness for each filter was then calculated independently for each bin. This allows the completeness in the outer bin to extend to slightly fainter levels.

# 5.3 PHOTOMETRIC CALIBRATION

#### 5.3.1 APERTURE CORRECTION

The completeness values measured from the simulated clusters require the instrumental magnitudes of an observation to be calculated. The magnitudes measured by Source Extractor are taken at fixed radii. As the sizes of real clusters are not all the same, taking a single aperture magnitude for all objects will not equally measure the total light. This fact suggests that we need a way to correct the fixed aperture photometry to account for the variable cluster size. This is done with the aperture correction. This correction is parameterized by an estimate of the size of the object,

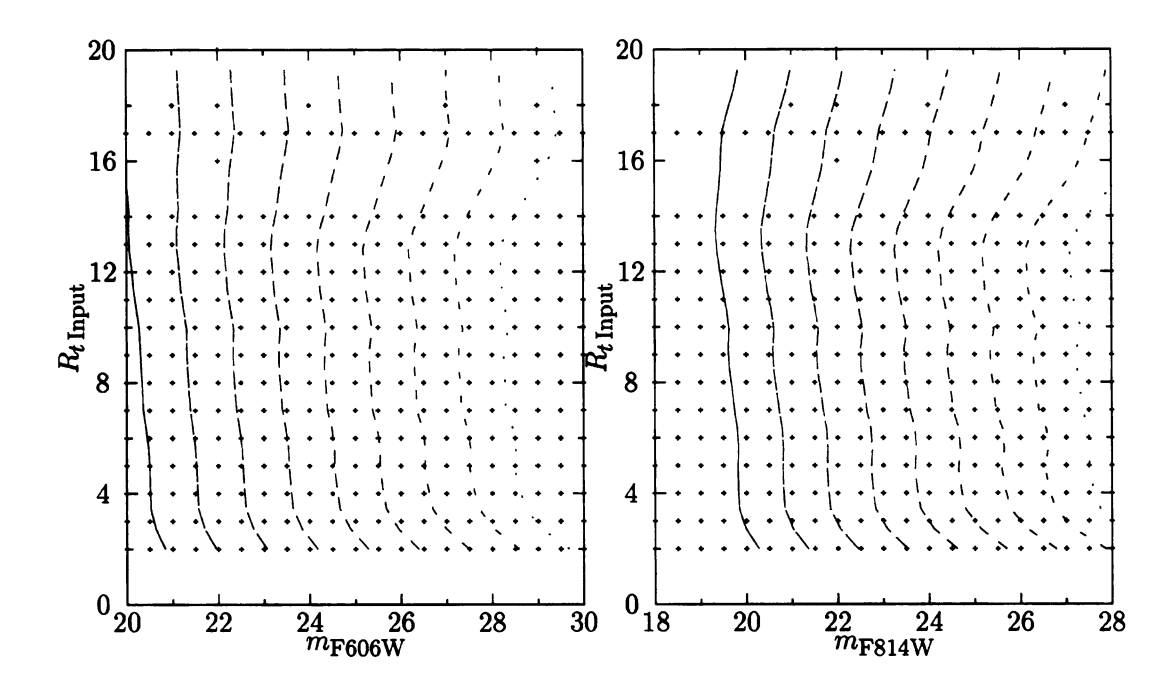


Figure 5.1 Completeness levels as a function of instrumental magnitude and input cluster size. The lines denote constant completeness, from 100% to 10%, with the completeness of the line equaling the data completeness. Note that the radius dependence is fairly weak, suggesting that the instrumental magnitude is the main factor in the completeness. The crosses show the locations of the simulated clusters used to estimate the completeness.

based on the measured magnitudes with different aperture radii:

$$\mathcal{R} = m_{4 \text{ pxl}} - m_{2 \text{ pxl}} \tag{5.2}$$

The logic behind this parameter is that a small object (with a radius smaller than 2 pixels) will have approximately the same magnitude in both apertures, yielding a value of  $\mathcal{R} \sim 0$ . As an object increases in size, more light is measured in the large aperture compared to the smaller, which pushes  $\mathcal{R}$  away from zero (and to more negative values due to the definition of magnitudes).

Given this size parameter, and one of the aperture magnitudes (taken as  $m_{4\,\mathrm{pxl}}$ 

for convenience), it should be possible to construct an aperture correction, such that

$$m_{\text{instrumental}} = m_{4 \text{ pxl}} + \mathcal{A}(\mathcal{R}, m_{4 \text{ pxl}})$$
 (5.3)

Conveniently, the data used for the completeness correction samples this function  $\mathcal{A}(\mathcal{R}, m_{4\,\mathrm{pxl}})$ , as the simulated clusters were created with a known instrumental magnitude, and  $\mathcal{R}$  and  $m_{4\,\mathrm{pxl}}$  are measured by Source Extractor. At each simulated cluster grid point, all detected clusters are measured, and the median values of  $\mathcal{R}$  and  $m_{4\,\mathrm{pxl}}$  are stored at that point, with the value of the aperture correction:

$$\mathcal{A}\left(\operatorname{median}(\mathcal{R}), \operatorname{median}(m_{4\,\mathrm{pxl}})\right) = m_{\operatorname{input\,instrumental}} - \operatorname{median}(m_{4\,\mathrm{pxl}})$$
 (5.4)

This grid of points has the upper end fixed, such that  $\mathcal{A}(0, m_{4pxl}) = 0$  to anchor the small object end of the aperture correction (which is not well sampled by the completeness data). This grid of values  $(\mathcal{R}, m_{4pxl}, \mathcal{A})$  is irregularly sampled as the values of  $\mathcal{R}$  do not linearly match the input sizes. For each detected object, the aperture correction is calculated using thin plate splines, which can interpolate such data. Figure 5.2 shows the surfaces of the aperture correction for the two filters.

In addition to this aperture correction, another correction of 0.1 magnitudes is applied to the final instrumental magnitude. This extra aperture correction compensates for light that is scattered to large angles by the optics of HST. This is a standard calibration step, and must be applied even though an aperture correction has already been applied. The simulated clusters used do not incorporate this scatter, as the PSF used ignores very wide angle scattering.

#### 5.3.2 Color Correction and Extinction

Most previously published results on globular clusters present the magnitudes using the standard Johnson Cousins BVRI system. Converting the instrumental magni-

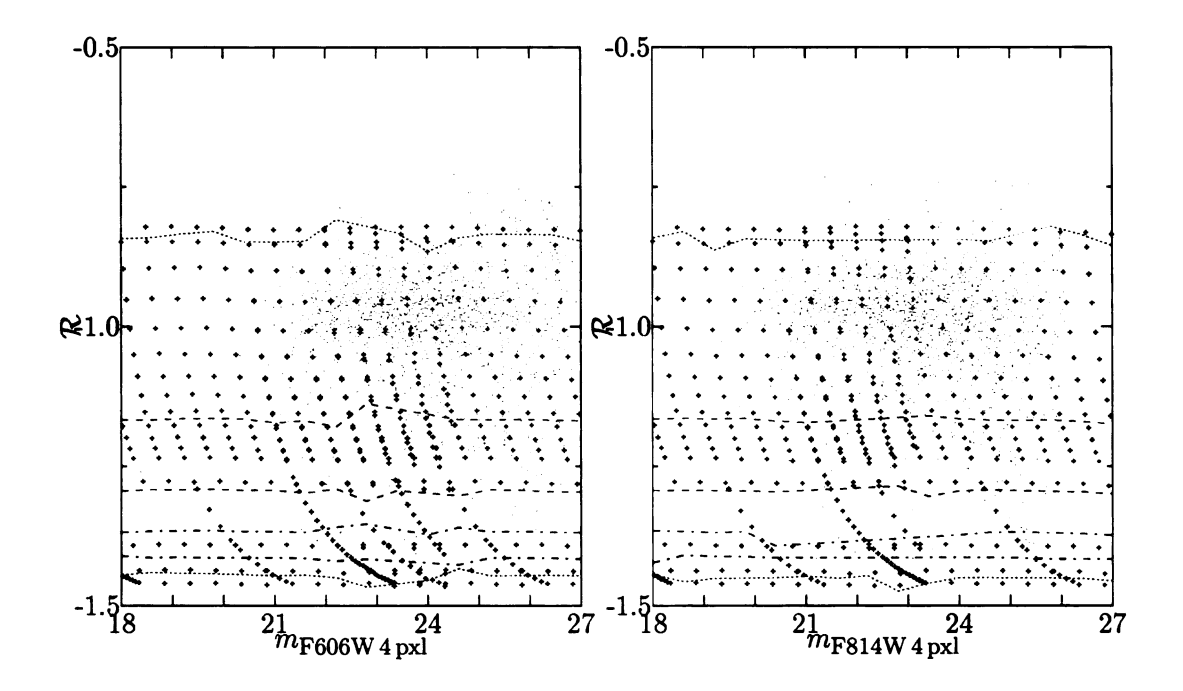


Figure 5.2 Aperture correction levels as a function of instrumental magnitude and input cluster size. The weak dependence on the measured magnitude indicates that the fraction of light lost is generally a function only of the object size. The crosses show the where the simulated clusters used for evaluation were placed, and the small dots show where the real globular cluster data falls.

tudes  $m_{\rm F606W}$  and  $m_{\rm F814W}$  to V and I requires a color correction. The correction parameters are taken from Sirianni et al. (2005) and reproduced in table 5.2

Table 5.2: Color correction parameters

Filter	$(V-I)_{ m break}$	$a_0$	$a_1$	$a_2$
F606W	< 0.4	$26.394 \pm 0.005$	$0.153 \pm 0.018$	$0.096 \pm 0.085$
	> 0.4	$26.331 \pm 0.008$	$0.340\pm0.008$	$-0.038 \pm 0.002$
F814W	< 0.1	$25.489 \pm 0.013$	$0.041 \pm 0.211$	$-0.093 \pm 0.803$
	> 0.1	$25.496 \pm 0.010$	$-0.014 \pm 0.013$	$0.015\pm0.003$
F775W	< 1.2	$25.241\pm0.005$	$-0.061 \pm 0.021$	$0.002 \pm 0.021$
	> 1.2	$25.292 \pm 0.033$	$-0.105 \pm 0.026$	$0.007 \pm 0.004$

The corrections are defined as:

$$V = m_{\text{F606W}} + a_0 + a_1(V - I) + a_2(V - I)^2$$

$$I = m_{\text{F814W}} + b_0 + b_1(V - 1) + b_2(V - I)^2$$

and are defined piecewise in color on two intervals separated at  $(V-I)_{\rm break}$ . The standard application of this color correction uses an iterative process, where the color V-I is updated at each step, and V and I are re-evaluated with that new color. Unfortunately, the piecewise definition of the color correction creates problems in the evaluation around the breaks. Instead, an algebraic solution was used, noting:

$$V - I = (m_{F606W} - m_{F814W}) + (a_0 - b_0) + (a_1 - b_1)(V - I) + (a_2 - b_2)(V - I)^2$$
 (5.5)

which can be solved for a corrected color in terms of the instrumental color. Formally, this yields two solutions, but it can be seen by checking a sample of colors that only the negative solution gives realistic magnitudes. Although this method seems to have the same problem at the color correction breaks, we can check that the calculated color falls within the necessary range for the coefficients used. Figure 5.3 shows a plot of the calculated V-I color as a function of the  $m_{\rm F606W}-m_{\rm F814W}$  instrumental color. As this function is continuous even around the color breaks, we can be sure that the color correction has been applied correctly.

The final photometric step is the application of an extinction term. This term accounts for the absorption of light as it passes through dust and gas in space. Using the Schlegel et al. (1998) value for M87's position on the sky, we can estimate this extinction as:

$$A_V = -0.074 (5.6)$$

$$A_I = -0.043 (5.7)$$

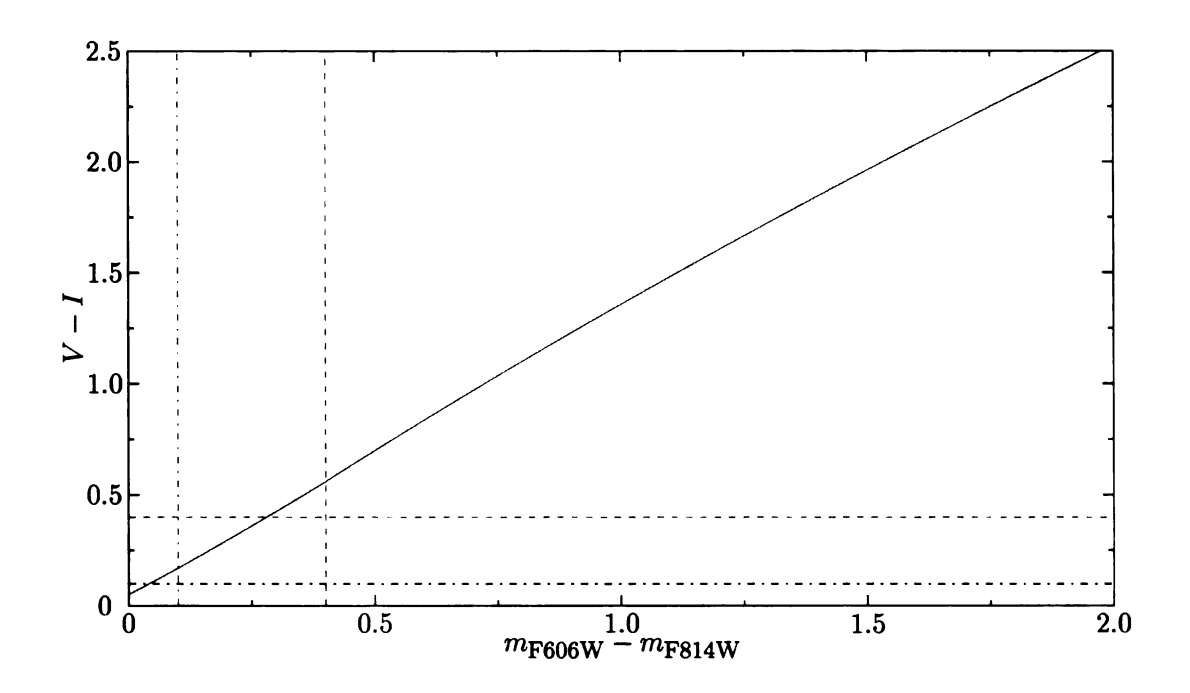


Figure 5.3 Plot of calculated V-I color as a function of instrumental  $m_{\rm F606W}-m_{\rm F814W}$  color. The continuity ensures that the correction has been applied correctly, even at the color breaks, which are marked with lines.

# 5.4 CONTAMINATION

Even with the various cuts placed on the data, it is still possible that some noncluster objects may remain in the sample. Although these objects masquerade as real clusters, we can statistically remove them by estimating how many of these objects should appear on our image. To do this, we need to find images that only contain the contaminating objects.

#### 5.4.1 Noise Objects

One method to look for noise spikes on the image is to run the detection code on an inverse image, generated by multiplying the data image by -1. The real objects on this inverted image have peaks that are then negative, and so fall below the detection threshold. Instead, only the dark areas of the data image will have peaks that allow

them to be detected. If the image histogram was perfectly symmetric, than the number of objects detected on this inverse image would directly give the number of noise spikes in the data image. The fact that the histograms shown in Figure 4.7 are not symmetric suggests that our data is deep enough to measure a bias in how the stars in M87 are distributed. Despite the fact that we cannot use these objects directly to correct for the contamination, we can still use this as a lower limit, and correct for the points that are detected.

#### 5.4.2 BACKGROUND GALAXIES

The contamination by background galaxies is obviously a major contribution to the number of objects found. A quick look at the galaxy subtracted data image shows a large number of background spiral galaxies that are easy to identify. The Hubble Ultra Deep Field (Beckwith et al., 2006) is a very deep data image taken of an "empty" field with a goal of looking at the distribution of distant galaxies. This gives an obvious way to estimate the contribution from these galaxies.

Unfortunately, simply searching for UDF galaxies will overestimate this contribution. Instead, we need to ensure that the noise characteristics of the UDF match that of the data. This first requires a rebinning of the UDF data from a pixel scale of 0.0.030 to the pixel scale of the data (0.0.045). Next, the UDF is overlaid on the image footprint of the data, and trimmed to match the field of view. With the geometry matched, the noise characteristics can be matched to our data. The UDF is given in counts per second, so must first be scaled to match the exposure time of our data. Finally a noise image is created from the data galaxy model. This noise model assumes each pixel is drawn from a Gaussian distribution with mean zero and standard deviation equal to the square root of the galaxy level. This noise model is then scaled such that when added to the UDF, the final image variance equals that of the data image. This method makes it certain that objects in the UDF frame that fall "near

the center of the galaxy" have more noise than objects that fall at the edge. Figures 5.4 and 5.5 show the original UDF image, as well as the final cropped and noise added final version. The apparent loss of objects from the center of the image is a result of the increase in the image noise in that region.

The reduction is identical for objects detected in the UDF as for the data objects, with the only exception being that the UDF filters are F606W and F775W. However, we can convert these filters to the same standard V and I system, minimizing the changes.

# 5.5 CLUSTER CANDIDATES

The cluster detection code used so far has been designed to detect as many objects as possible. Unfortunately, this also means that some fraction of the objects detected are not true globular clusters. The two main sources of contaminating objects are background galaxies and noise fluctuations from the galaxy light (including random local overdensities in the stars that make up the galaxy). To eliminate as many of these contaminating objects as possible, we make a series of cuts in the many dimensional space of parameters.

The first cut is to remove objects that have  $d_{\rm merge} > 0''.015$ . This removes things that are likely to be random matches of noise between the two images, that do not represent real objects. Next, we can apply a color cut where only objects with 0.5 < V - I < 1.7 are considered to be globular clusters. These limits are based on observations of other globular cluster systems and cover the range of colors where clusters are known to exist. Finally, we only want to consider objects that have a final completeness value greater than 0.5. This limit is chosen because if we are only detecting half of these objects, then any count of them is influenced more by the errors in the completeness than in the true number of objects.

These cuts so far are all based on obvious ways to limit the sample. We can

also make the assumption that globular clusters are circular, and set limits on their ellipticity such that  $\frac{A}{B}\Big|_{V,I} < 1.5$ . We also assume that clusters are peaked, such that the central pixel is brighter than the rest of the cluster. By comparing the peak surface bright to a calculated average surface brightness, we can exclude objects where the average surface brightness is brighter than the peak surface brightness:

$$\mu_{\text{peak}} < V + 2.5 \log_{10} \left( A_{\text{ISO}} \left( \frac{0.00455}{1 \text{pxl}} \right)^2 \right)$$
(5.8)

Such an object is likely a very extended background galaxy, or a very blurry noise object.

The numbers of clusters detected with each of the various cuts are given in table 5.3. This shows that the various restrictions on the data remove the majority of the contaminating objects, and yields a final number of clusters consistent with what is expected based on earlier surveys. The one object that is manually excluded from the sample is the HST-1 knot in the jet, which successfully eludes these cuts. This is likely due to the fact that it is dominated by a small flaring emission source, that makes it appear reasonably point like (Perlman et al., 2003; Waters & Zepf, 2005). Figure 5.6 shows the color magnitude diagrams of both the full sample of detected objects, as well as the full sample of objects on the contaminating frames. It is clear that at the brightest magnitudes, the globular clusters are easy to identify.



Figure 5.4 F606W UDF image rescaled to match the pixel scale of the M87 data. Nearly all objects on this image are galaxies, making it an excellent field to investigate the expected contamination from background galaxies.



Figure 5.5 F606W UDF image cropped to the footprint of the M87 data, and with added noise to simulate the effects of the galaxy subtraction process. This added noise can be seen by the apparent preferential loss of objects from the center of the image, where the noise added has a stronger variance.

Table 5.3: Impact of Selection Cuts on Sample Size

Cut	$N_{ m clusters}$	$N_{ m inverse}$	$N_{ m UDF}$
Raw V	9454	721	790
Raw I	12495	249	255
Joint V+I	6624	194	249
$d_{ m merge} < 0\rlap.{''}015$	5392	194	249
${\rm Completeness} > 0.5$	4045	47	231
V-I < 1.7	3113	26	176
V-I>0.5	2919	16	114
$\left. \frac{A}{B} \right _V < 1.5$	2434	6	60
$\left. rac{A}{B}  ight _I < 1.5$	2191	4	34
$\mu_{ m peak} < \langle \mu \rangle$	2092	2	33
Final Sample	2091	2	33

# 5.5.1 PHOTOMETRIC ACCURACY

As the ACS pointing contains the majority of the clusters imaged by Kundu et al. (1999) and Waters et al. (2006), we can test the photometric accuracy of the survey by comparing the measured magnitudes to those previously done. For the Kundu et al. (1999) sample, there are 989 clusters matched between the two samples, with magnitude differences

$$V - V_{
m Kundu} = -0.028 \pm 0.100$$
 
$$I - I_{
m Kundu} = 0.033 \pm 0.107$$
 
$$(V - I) - (V - I)_{
m Kundu} = -0.06 \pm 0.110$$

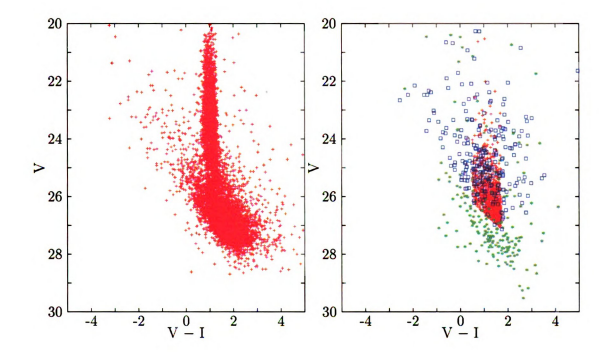


Figure 5.6 Color magnitude diagrams of detected objects. The left panel shows all objects detected on the data image. The globular clusters are clearly visible as the vertical stripe around  $V-I\sim 1.0$ . The right panel shows the objects detected in the inverse (shown as asterisks) and UDF (shown as boxes) images. The objects detected in the data image, but excluded from the sample due to their properties are also shown as small crosses.

For the Waters et al. (2006) sample, there are 814 clusters in common, and the differences are

$$V - V_{\rm Waters} = 0.035 \pm 0.102$$
 
$$I - I_{\rm Waters} = 0.073 \pm 0.086$$
 
$$(V - I) - (V - I)_{\rm Waters} = -0.035 \pm 0.127$$

These deviations are consistent with the expected photometric errors.

# 5.6 LUMINOSITY FUNCTION

The luminosity function for the globular clusters shows how many are detected at a given magnitude. Each detection is weighted by the a factor

$$W_i = \frac{\pm 1}{\text{Completeness}_i} \tag{5.9}$$

where the positive case is for objects from the "cluster" sample, and the negative case for the "false" and "UDF" samples. These samples are included to correct for the expected contaminating objects that still exist in the sample. The error in each bin is then

$$E_{\rm bin} = \langle |W_i| \rangle \sqrt{N_{\rm bin}} \tag{5.10}$$

Figure 5.8 shows the final GCLF, including both the completeness weighting and the contamination rejection. Overplotted with the GCLF is the smoothed completeness as a function of magnitude. This shows that our sample is 50% complete to nearly  $V \sim 27$ . As this is the product of the completenesses in both the F606W and F814W filters, the final completeness is color dependent. For the range of colors we consider for our globular cluster sample, the 50% completeness limit generally follows the line  $V_{50\%} \sim 25.9 + 0.8 \, (V - I)$ .

GCLFs have in general been modeled by Gaussians, due to their peaked natures. Recently, more physically motivated models have been used, based on the expected mass lost from the clusters. Such models are discussed further in Chapter 6. The best fitting Gaussian to the binned GCLF gives a turnover of  $\langle V \rangle = 23.62$  with a width of  $\sigma_V = 1.40$ . Repeating this for the I data yields  $\langle I \rangle = 22.58$  with  $\sigma_I = 1.35$ .

### 5.6.1 COLOR DEPENDENCE

The M87 globular clusters are bimodal in color, as are the GCs in most galaxies. This bimodality is obvious from the color magnitude diagram, in figure 5.7, with a blue

peak around  $V-I\sim 0.9$  and a red peak at  $V-I\sim 1.1$ . If we divide the clusters between two samples in color separated at  $V-I\sim 1.03$ , we can create luminosity functions for each. This divisions places 959 clusters in the blue sample, and 1133 in the red sample. Figure 5.9 shows the GCLFs for these two samples, along with their associated completeness functions.

It is clear from this figure that the faint end of the blue sample falls off faster than the red sample. This drop is somewhat expected based on the color dependent completeness function, but as shown, the falloff occurs at a level where the sample should still be roughly 90% complete. Therefore, this drop must be a real effect, such that the faintest clusters tend to be from the red sample. On the bright end of the GCLF, the blue sample also drops off at brighter magnitudes. Fitting Gaussians to these two samples confirms these effects, with the blue sample having a higher mean than the red sample, with  $\langle V \rangle_{\rm blue} = 23.31$  and  $\langle V \rangle_{\rm red} = 23.89$ . In addition to the differences in the means, the widths of these Gaussian fits are also different, with the blue sample significantly narrower than the red sample:  $\sigma_{\rm blue} = 1.21$  and  $\sigma_{\rm red} = 1.40$ .

We can check that these fits are not just an effect of the sampling by comparing them with the t- and F- tests. These tests indicate that the means of the two samples are significantly different (t=10.042, p-value =  $1.6 \times 10^{-23}$ ), as are the variances (F=1.34, p-value =  $2.5 \times 10^{-6}$ ).

#### 5.6.2 RADIAL DEPENDENCE

Although we can only measure the projected distance from the clusters to the center of M87, any radial dependence of the cluster luminosities should still be evident. To investigate this, the clusters were divided into five bins in projected radius with widths of 2 kpc. Table 5.4 shows the Gaussian fits to the GCLFs for these bins, along with the number of clusters in each bin. The fall in the number of clusters beyond  $R_{GC} \sim 6$  kpc is due to the shape of our field, and not from a sudden drop in the

cluster density. Figure 5.10 plots the binned GCLFs as simple lines, along with the completeness functions for each bin. We can see that the peak of the GCLF moves fainter with increasing distance from the center of the galaxy, along with an increase in the GCLF dispersions.

Table 5.4: Radial Dependence of the GCLF

Bin	$N_{ m GC}$	$\langle V \rangle$	σ
0 < R < 2	186	23.30	0.985
2 < R < 4	481	23.46	1.246
4 < R < 6	569	23.56	1.280
6 < R < 8	568	23.73	1.437
8 < R < 10	244	23.75	1.488

We can again use the t- and F- tests to confirm that this radial gradient is a real property of the GCLF. Comparing each bin against the next larger indicates that only the outer two bins have consistent means ( $p \sim 0.43$ ). This is likely due to the fact that the outermost bin preferentially samples the smaller radii due to the square shaped frame, so it is sampling clusters most like its neighboring bin. The variances also match for the two outer bins ( $p \sim 0.53$ ) and also for the  $R_{2\rightarrow 4}$  and  $R_{4\rightarrow 6}$  bins ( $p \sim 0.53$ ). Again, the differences in completeness make an attractive explanation for this, but as before, the data is complete beyond the point where the GCLF begins to fall.

#### 5.6.3 Comparison with Published Results

A selection of published Gaussian GCLF fits are presented in Table 5.5. Figures 5.11 and 5.12 show these fits overplotted with this new ACS GCLF data for both filters.

The first GCLF to compare our data to is based on the Harris (1996) catalog of Milky Way globular clusters, using the most recent (2003) revision. The histogram of this data is shown in figure 5.11, illustrating the statistical advantage found in our sample. The peak for the Milky Way is only marginally fainter than we observe in M87, with a t-test p value that suggests they are not significantly different. The variances, however, are very much different, with the Milky Way GCLF much narrower. This variance is in fact consistent with the M87 blue sample, which is reasonable as the Milky Way GC system is composed predominantly of blue clusters.

For our V GCLF, we compare against the two WFPC/2 surveys (Kundu et al., 1999; Waters et al., 2006) as well as one ground based survey (McLaughlin et al., 1994). The WFPC/2 samples match well, with reasonable t- and F- test p values. Incorporating the photometric offsets calculated in Section 5.5.1 shifts the turnover values even further into agreement. The McLaughlin et al. (1994) sample has much brighter completeness limits, such that they are only sensitive to the bright half of the GCLF. This leads to a significant problem in fitting a Gaussian, as is seen by the fainter peak and wider dispersion.

The agreement with the I GCLF is not quite as good, likely due in part to the worse completeness effects for the I data. The Kundu et al. (1999) and Waters et al. (2006) samples are again reasonably consistent, with the p values improving again when the offsets between the samples are applied. The comparison with the ACSVCS sample (Jordán et al., 2007) indicates significant disagreement. This is likely biased due to the fact that the ACSVCS used the F850LP (z) filter, which extends further into the infrared that our F814W. To compare the samples, we've used a simple conversion of I - z = 0.3. This ignores any more complicated color dependence of the correction, which may account for the narrower dispersion in the ACSVCS fits. However, it seems far more likely that the ACSVCS dispersion is an underestimate, based on the lack of the very faintest clusters in their sample.

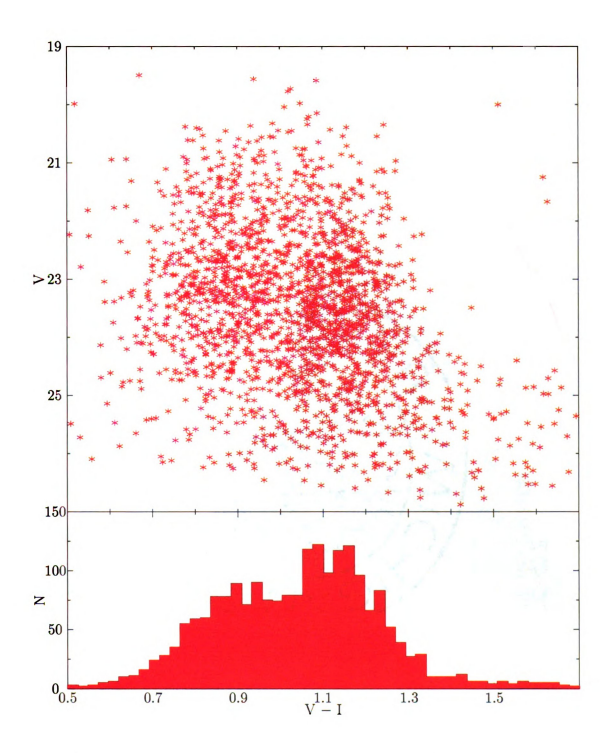


Figure 5.7 Color magnitude diagram of the final sample of clusters with color histogram. The blue and red clusters can be seen as grouping around  $V-I\sim0.9$  and  $V-I\sim1.1$  respectively.

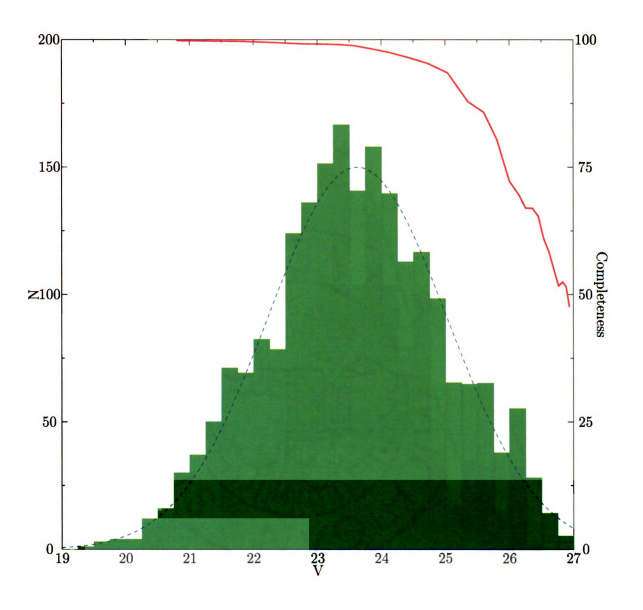


Figure 5.8 Final globular cluster luminosity function along with the completeness function. This shows that the sample is at least 50% complete down to 27th magnitude, where the cluster distribution is seen to drop to roughly zero. The dashed curve represents the best fitting Gaussian, with  $\mu=23.623$  and  $\sigma=1.40$ .

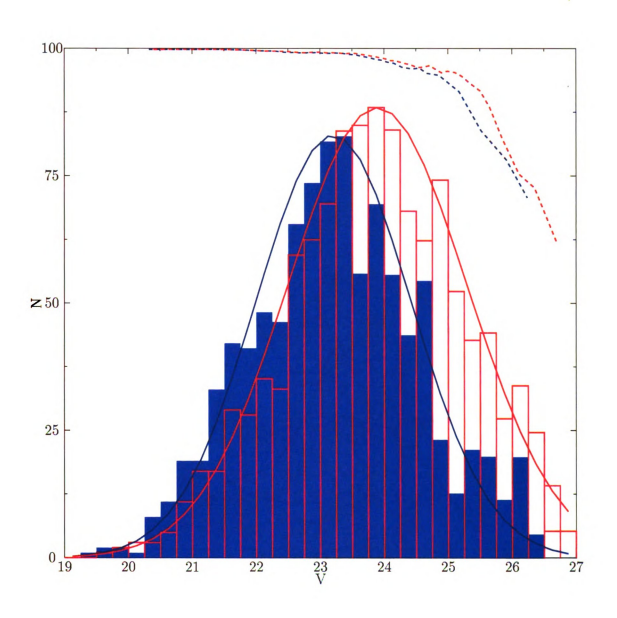


Figure 5.9 Comparison of the red and blue cluster GCLFs. The Gaussian fits are plotted, along with the smoothed completeness curves for both samples.

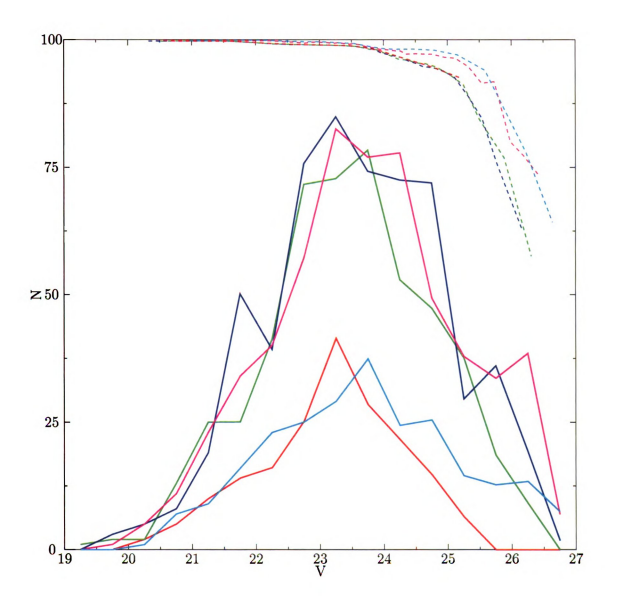


Figure 5.10 Comparison of the GCLF between five bins in projected distance from the center of M87 along with their completeness curves. The lines are for  $R_{0\rightarrow2}$  (red),  $R_{2\rightarrow4}$  (blue),  $R_{4\rightarrow6}$  (green),  $R_{6\rightarrow8}$  (magenta), and  $R_{8\rightarrow10}$  (cyan).

Table 5.5: Gaussian Fits to the GCLF

Galaxy	Reference	Filter	Filter N <sub>GC</sub> Limit	Limit	η	Q	t-value	Ь	F-value	Ь
Milky Way	Milky Way Harris (1996)	>	153	~ 29	23.70	1.18	0.656	0.256	1.412	$6.8 \times 10^{-3}$
M87	McLaughlin et al. (1994)	>	3688	$\sim 24$	24.20	1.73	13.108	0.00	1.52	0.00
M87	Kundu et al. (1999)	>	1032	$\sim 26$	23.67	1.39	0.887	0.188	1.018	0.749
M87	Waters et al. (2006)	^	1013	$\sim 26$	23.60	1.42	0.428	0.334	1.026	0.645
M87	Kundu et al. (1999)	I	1032	$\sim 25$	22.55	1.28	0.496	0.31	1.118	0.039
M87	Waters et al. (2006)	Ι	1013	$\sim 25$	22.50	1.30	1.467	0.02	1.08	0.137
M87	Jordán et al. (2007)	z	1745	$\sim 26$	22.689	1.242	9.84	$6.88 \times 10^{-23}$	1.187	$1.8 \times 10^{-4}$
M87	This sample	>	2091	$\sim 27$	23.623 1.402	1.402				
M87	This sample	I	2091	$\sim 26$	22.575	1.353				

# 5.7 Blue Tilt

Recent deep observations of extragalactic globular cluster systems have suggested the existence of a "blue tilt," where fainter clusters from the blue metal poor sample are bluer (and hence, more metal poor) than the brighter blue clusters (Strader et al., 2006; Harris et al., 2006). This tilt is explained as a result of a metallicity-luminosity relation of the form  $Z \propto L^{0.55}$ .

We can look for such a trend in our data by dividing the sample into bins of width one magnitude, and running a KMM (Ashman et al., 1994) test on these samples. This test looks for bimodality in the sample, and finds the best fitting peaks and dispersions for the two groups. Table 5.6 shows the results of this test, and the results are plotted over the globular cluster color-magnitude diagram in figure 5.13.

Table 5.6: Bimodality with Cluster Luminosity

Bin	$N_{ m GC}$	$\%_{\mathrm{blue}}$	$\mu_{ m blue}$	$\sigma_{ m blue}$	$\%_{ m red}$	$\mu_{ m red}$	$\sigma_{ m red}$
V < 20	9	0.22	0.59	0.11	0.78	1.12	0.19
20 < V < 21	63	0.53	0.85	0.09	0.47	1.10	0.08
21 < V < 22	229	0.47	0.84	0.08	0.53	1.11	0.11
22 < V < 23	421	0.54	0.87	0.10	0.46	1.14	0.06
23 < V < 24	613	0.45	0.85	0.09	0.55	1.15	0.08
24 < V < 25	459	0.35	0.84	0.10	0.67	1.19	0.13
25 < V < 26	224	0.49	0.95	0.15	0.51	1.33	0.13
26 < V < 27	74	0.48	0.98	0.16	0.52	1.42	0.14

The brightest bin contains too few objects to give reliable results, and the color dependent completeness can be seen to deplete the edge of the CMD below  $V \sim 25$ , making the faintest two bins also unreliable for investigating the color bimodality.

The remaining bins have almost identical values for  $\mu_{\text{blue}}$ , indicating that our sample shows no evidence for a blue tilt. As this sample is much deeper (generally by at least a magnitude) and more complete than those that appear to have a blue tilt, it seems likely that the tilt is not a real effect, but rather some systematic photometric error.

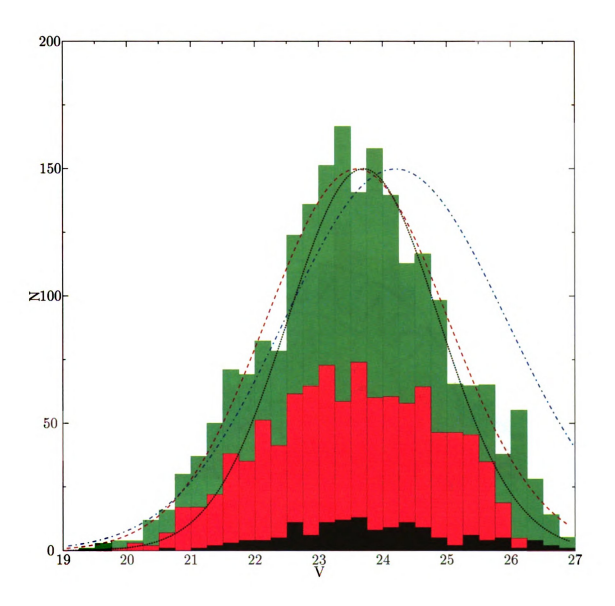


Figure 5.11 Comparison of the final GCLF to the M87 GCLF of Waters et al. (2006) (red histogram) and the Milky Way GCLF based on the data of Harris (1996) (black histogram). This comparison shows the number advantage this new sample presents. In addition, the truncation of the Waters et al. (2006) sample at  $V \sim 26$  can be seen to limit the faint end of the GCLF. Overplotted are the best fitting ACS Gaussian fit (dashed line), the Milky Way fit (dotted line), and the ground based McLaughlin et al. (1994) fit (dot dashed), rescaled to match the number of ACS clusters.

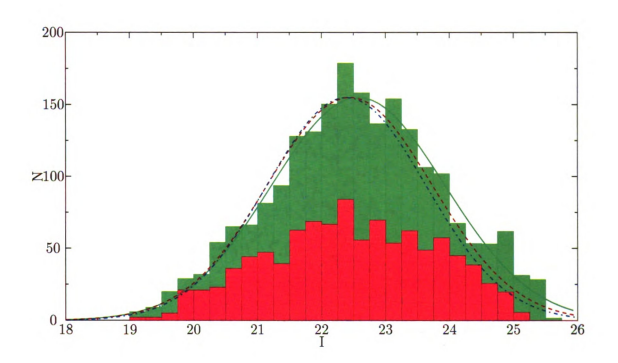


Figure 5.12 Comparison of the final I band GCLF to the M87 GCLF of Waters et al. (2006). The Gaussian fits are for the ACS (solid), WFPC/2 (dashed), and the ACSVCS z filter (dot dashed).

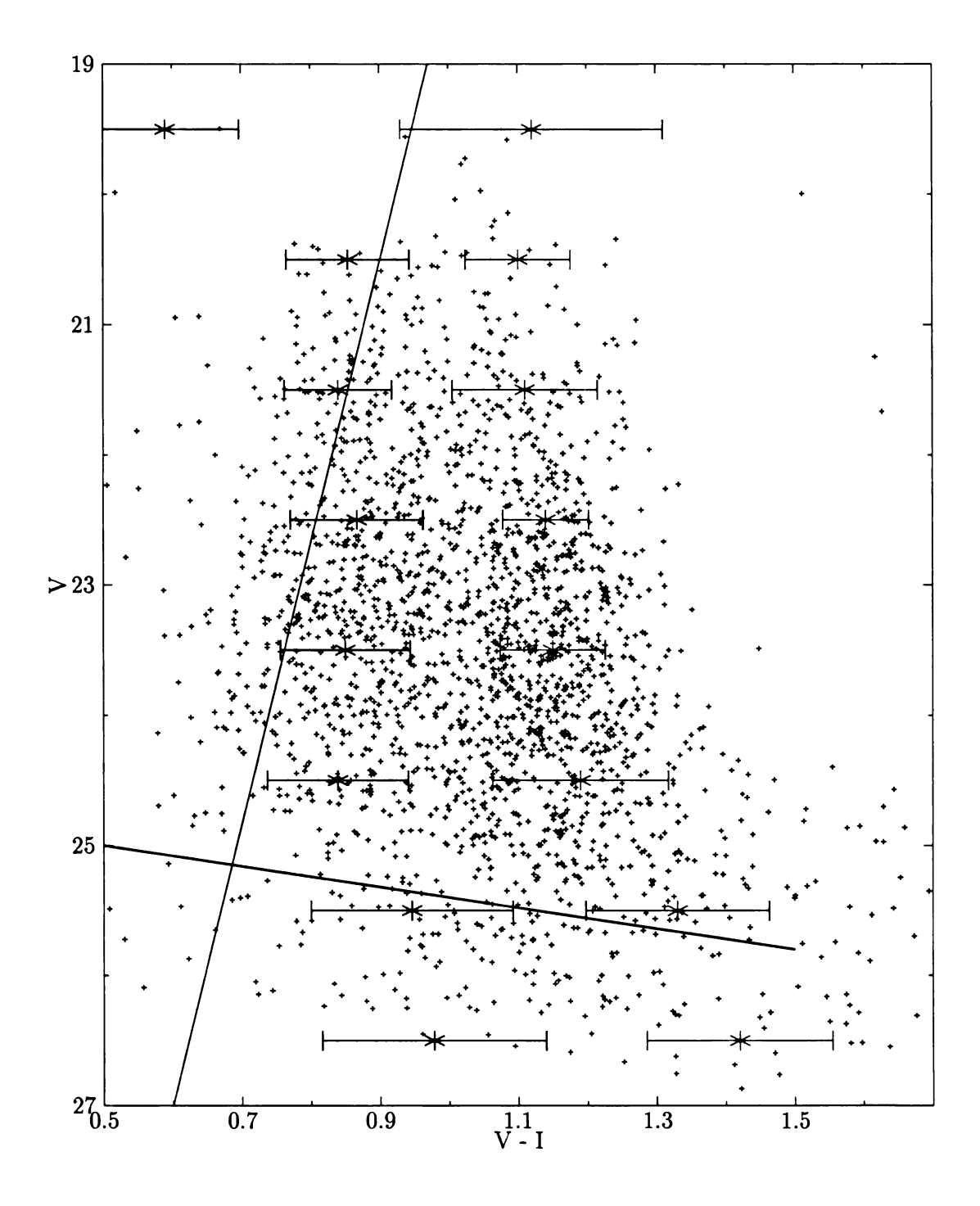


Figure 5.13 Bimodality of the cluster sample as a function of magnitude. As the peaks of the blue cluster distribution stay constant from  $V \sim 21$  to  $V \sim 25$ , we see no evidence for a blue tilt. The black line illustrates the 90% completion limit, below which we expect to see completeness issues influence the fitting.

# CHAPTER 6: GLOBULAR CLUSTER MASS FUNCTION

The mass spectrum of globular clusters is defined as  $\psi(M)dM$ , which gives the number of clusters with mass between M and M+dM. We then define the mass function as

$$\Psi(\log_{10}(M)) = \frac{M\psi(M)}{\log_{10}(e)}$$
(6.1)

to directly relate to observational counts of clusters. In the literature, both  $\psi$  and  $\Psi$  are interchangeably called the "mass function."

For an initial mass function  $\psi_0 \equiv \psi(M,0) = \psi(M)$ , we can see that the evolved form of this must be  $\psi(M,t) \propto \psi_0(M_0)$  where  $M_0$  is the original mass of the cluster at t=0. Considering the mass loss mechanisms of section 2.3, we can see that for both stellar evolution and gravitational shocks, the mass loss has the form

$$\frac{M(t)}{M_0} = e^{-\nu t} \tag{6.2}$$

whereas two body relaxation yields

$$M(t) = M_0 - \mu t \tag{6.3}$$

Since the form of both stellar evolution and gravitational shocks simply scales the initial mass function, we can neglect the effects of these mechanisms, and instead, simply allow the normalization to change over time. This defines the evolution with

respect only to the number of clusters that survive. Evaporation does not follow this form, and so must be treated by actually evolving the cluster mass spectrum.

# 6.1 Initial Mass Function of Globular Clusters

For this study of the M87 globular cluster system, we want to consider two forms for the initial mass function. The first IMF we consider is a power law, where

$$\psi(M) \propto M^{-\alpha} \tag{6.4}$$

The standard choice of  $\alpha$  is  $\alpha=2.0$ , as this is what is observed to be the luminosity function of young star clusters in merging galaxies (Zhang & Fall, 1999). Since these merging galaxies are thought to be in the process of creating new globular clusters, this observed function is likely to be a reasonable estimate of the mass function of all systems of newly formed clusters. This IMF is also reasonable from a theoretical standpoint, as it assumes that the collapse of the giant molecular clouds that form GCs is effectively scale free.

Unfortunately, such power law mass functions overpredict the number of high mass globular clusters in many evolved systems. A solution is to use a Schechter (1976) like function, in which above some cutoff mass,  $M_C$ , the number of clusters decays exponentially:

$$\psi(M) \propto M^{-\alpha} e^{-M/M_C} \tag{6.5}$$

This form retains a power law shape at low masses, but falls off to more closely match observations at higher mass. Burkert & Smith (2000) present this form of IMF as the result of the expected mass function for the sizes of giant molecular clouds that form from the merging of smaller clouds. They give  $\alpha = 1.5$  and also provide a fit to value for the cutoff in M87,  $M_C = 5 \times 10^6 M_{\odot}$ . We use this form for the fitting, although we allow the cutoff value to be fit to match the data.

# 6.2 Mass Loss Rates

If we define the mass loss rate as

$$\frac{dM}{dt} = -kM^{-\gamma} \tag{6.6}$$

we would like to find a form for the total mass function as a function of time, given the initial mass function  $\psi_0(M)$ . As the mass loss equation is so simple, we can solve it by direct integration:

$$M^{\gamma}dM = -kdt$$

$$\int_{M_0}^{M(t)} M^{\gamma}dM = -k \int_0^t dt$$

$$\frac{1}{1+\gamma} \left( M(t)^{1+\gamma} - M_0^{1+\gamma} \right) = -kt$$

So, the cluster mass at any time is just

$$M(t)^{1+\gamma} = M_0^{1+\gamma} - kt(1+\gamma) \tag{6.7}$$

Since we observe the evolved mass, we can invert this to find the starting mass for a given cluster, which gives the relative weights for that cluster from the IMF. This gives the mass spectrum for evolved clusters as

$$\psi_{\text{evolved}}(M) = \psi_{IMF}(M_0)$$
 (6.8)

$$= \psi_{IMF} \left( \left( M(t)^{1+\gamma} + kt(1+\gamma) \right)^{1/(1+\gamma)} \right)$$
 (6.9)

This evolved mass function depends on the product of the mass loss rate and the current time of evolution. As we only know the current ages of the clusters indirectly, it makes sense to consider this as a single parameter,  $\tau = k \cdot t$ . This represents the total mass lost by the cluster over its entire life. This also provides the peak value

of the GCMF, as clusters at the peak have lost roughly half their mass, and so have current masses equal to  $\tau$ .

### 6.2.1 FALL & ZHANG

Following Fall & Zhang (2001), we can consider the mass loss of a globular cluster to be due mainly to the effects of two-body relaxation. As stellar evolution happens quickly, we can assume that it happens immediately after the clusters' formation, and as such, can be treated as a simple shift of the IMF. Similarly, the mass loss due to shocks affects the mass function as a whole, and can also be ignored as a simple shift. Using the general form above, we can write the mass loss as

$$\frac{dM}{dt} = -kM^{0.0} \tag{6.10}$$

where is k is the  $\mu_{ev}$  of evaporation defined in section 2.3.4.

#### 6.2.2 BAUMGARDT & MAKINO

We would also like to consider the model presented by Baumgardt & Makino (2003), based on N-body calculations of multimass globular clusters. These simulations included all of the mechanisms presented in section 2.3. Baumgardt & Makino (2003) parameterize the dissolution timescale of clusters in their simulation as

$$t_{\text{diss}} = k t_{rh}^{x} t_{\text{crossing}}^{1-x}$$

$$= k \left( \frac{N^{1/2} r_{h}^{3/2}}{G^{1/2} m^{1/2} \ln \Lambda} \right)^{x} \left( \frac{r_{h}^{3/2}}{G^{1/2} N^{1/2} m^{1/2}} \right)^{1-x}$$

$$\sim k \left( \frac{N}{\ln \Lambda} \right)^{x} \frac{R_{G}}{V_{G}}$$
(6.11)

Noting that  $N = \frac{M}{\langle M_{\star} \rangle}$ , we can see that this gives

$$t_{\rm diss} \propto M^x$$
 (6.12)

We can convert this to the general form by noting

$$\int_{M_0}^0 -kM^{\gamma} dM = \int_0^{t_{\text{diss}}} dt \tag{6.13}$$

$$k\frac{1}{\gamma+1}M_0^{\gamma+1} = t_{\text{diss}} \tag{6.14}$$

so,  $\gamma = x - 1$ . The simulations they performed suggested a range of x from 0.75 to 0.85, with 0.75 being their preferred value. This gives a general mass loss:

$$\frac{dM}{dt} = -kM^{-0.25} (6.15)$$

Some authors have suggested that the correct way to convert the Baumgardt & Makino (2003) dissolution time to a mass loss is to set the mass loss rate  $k \propto M_0^{\gamma}$ , and leave that fixed for the entire lifetime of the cluster. For an evolved system like M87, this will give a result very similar to the constant mass loss rate  $\dot{M} = kM^{0.0}$ . All massive clusters  $(M \gg \tau)$  will have lost such a small fraction of their mass that they show no change. The least massive clusters  $(M \ll \tau)$  will also have effectively the same mass loss rate, as they all come from progenitor clusters with nearly identical masses. Only around the turnover  $(M \sim \tau)$  will there be much change, where the progenitor masses are sufficiently different to create changes in the mass loss rate. This will have the effect of creating a slightly more peaked mass function, although the scale of this effect is still very small.

A final check that setting the mass loss rate as a function of the current cluster mass is correct can be seen by overplotting the evolution curve of this model against the evolution curves plotted by Baumgardt & Makino (2003) of their N-body simu-

lations. Figure 6.1 does this, illustrating that both this model and the N-body data drop faster than linear early in the cluster's life, and then slow down to a slower than linear loss in the later stages of evolution.

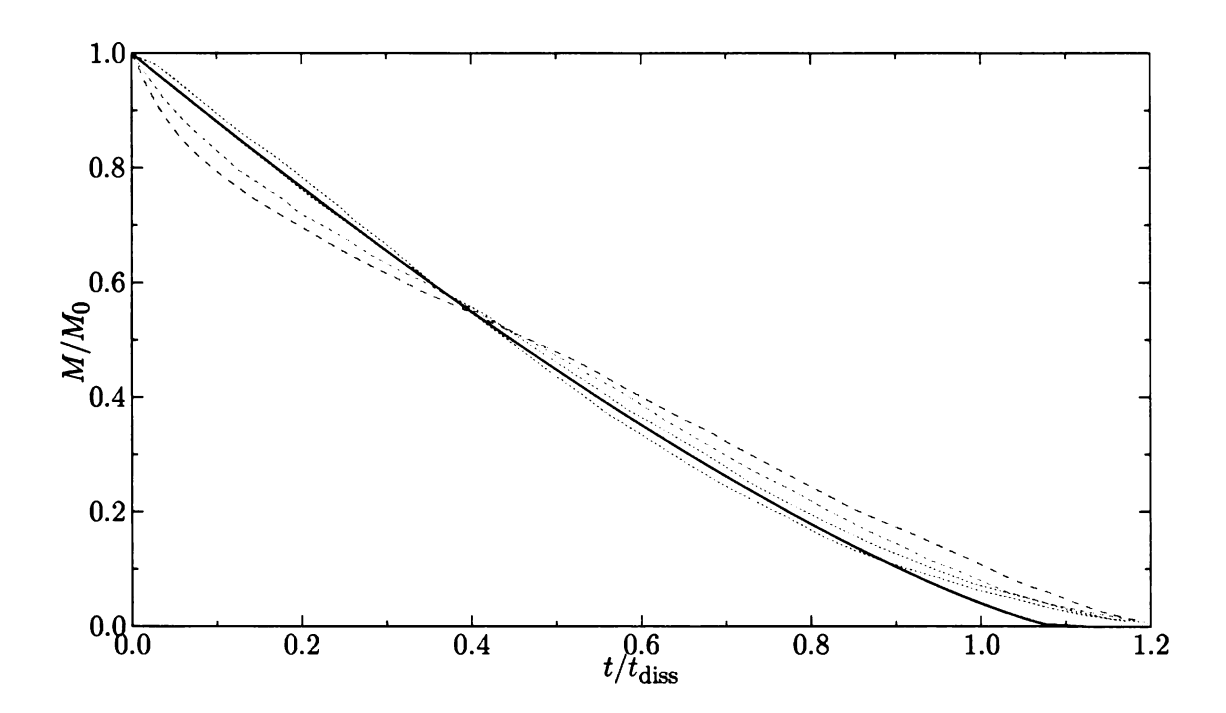


Figure 6.1 Comparison of  $\dot{M} \propto M^{-0.25}$  mass loss model to various Baumgardt & Makino (2003) N-body simulations. The deviation around  $t/t_{\rm diss}=1.0$  arises from the differences when the number of stars in the cluster becomes small.

#### 6.2.3 Lamers et al.

The final published model we consider is that given by Lamers et al. (2005). This model builds upon the results of Baumgardt & Makino (2003), by noting that as  $\ln \Lambda$  also depends on the number of particles, it must slowly vary over the life of the cluster as the number of stars drops. They use a polynomial fit to this function, adopting the form

$$1.91 \left(\frac{N}{\ln \Lambda}\right)^{0.75} = 1.911. \left(\frac{N}{\ln (0.02N)}\right)^{0.75} \sim 951.N^{0.62}$$
 (6.16)

This polynomial is equivalent around  $N\sim 3\times 10^5$ , which corresponds to a mass

 $M_{\rm equiv} \sim 1.25e5$ , with a slight overestimate of the dissolution time for lower masses. Lamers et al. (2005) also notes that for an object moving in a circular orbit,

$$\frac{v^2}{r^2}m = \nabla \cdot \vec{F} = 4\pi G\rho \tag{6.17}$$

and uses this to substitute the local galaxy density for the second term in the Baumgardt & Makino (2003) solution, giving their final dissolution time as

$$t_{\rm diss} = C_{env} \left(\frac{M}{10^4 M_{\odot}}\right)^{0.62} \left(\frac{\rho}{M_{\odot} pc^{-3}}\right)^{-1/2} {\rm Myr}$$
 (6.18)

where  $C_{env}$  is a parameterization of the dissolution time. They quote a value for  $C_{env}$  of 810, with a range stretching down to 300.

They compare this relation to the star cluster populations of the Milky Way, M51, M33, and the Small Magellanic Cloud. Although these samples contain large numbers of young clusters that are unlikely to be bound globular clusters, they insist the results are valid for all types of clusters. Using the general form again, this has a mass loss

$$\frac{dM}{dt} = -kM^{-0.38} (6.19)$$

following the conversion from dissolution time to mass loss used above for Baumgardt & Makino (2003).

#### 6.3 Mass Function

The observed clusters are used to make the mass function for M87, by first converting the measured magnitudes to masses, via the relations:

$$\begin{array}{lcl} \frac{L}{L_{\odot}} & = & 10^{(V+5-5\log_{10}(d)-V_{\odot})/(-2.5)} \\ \frac{M}{M_{\odot}} & = & \Upsilon \frac{L}{L_{\odot}} \end{array}$$

where we take the mass to light ratio to be equal to  $\Upsilon=3.0$ . A histogram of these masses is created in boxes of logarithmic M, weighted by their completion factors (in the same way as for the GCLF), yielding the mass function  $\Psi$ . This mass function is plotted in figure 6.2, along with the best fitting mass loss models. This figure shows that the Burkert & Smith (2000) IMF fits the high mass clusters best.

The fits to the mass loss models were created by minimizing the  $\chi^2$  deviations for each bin. The models were allowed two free parameters: A, an arbitrary normalization defined to be equal to the value of  $\log_{10}(\Psi(6))$ , and  $\tau$ , the total mass loss experienced by the clusters. For the Burkert & Smith (2000) IMF, the value of  $M_C$  was also allowed to vary to ensure the best possible model. This makes only a small difference in the value, as  $M_C$  tends to stay reasonably close to the initial value. The best fitting values for these fits for each mass loss model are given in table 6.1 along with the reduced  $\chi^2$  for each fit.

Table 6.1: Best fitting mass loss fits to ACS data.

IMF		γ	au	A	$\chi^2$
Powerlaw	$\alpha = 1.8$	0.00	150980	2.275	2.9933
		0.25	9346.2	2.277	3.5235
		0.38	2273.8	2.275	3.8841
Powerlaw	$\alpha = 2.0$	0.00	202558	2.281	2.4658
		0.25	12175	2.279	3.0689
		0.38	2927.4	2.275	3.4850
Burkert & Smith (2000)	$\log_{10}(M_C) = 6.4$	0.00	178462	2.375	1.3648
		0.25	11950	2.382	1.6782
		0.38	3238.6	2.390	1.8368
Burkert & Smith (2000)	$\log_{10}(M_C) = 6.376$	0.00	186644	2.382	1.3512
	$\log_{10}(M_C) = 6.343$	0.25	13481	2.399	1.6053
	$\log_{10}(M_C) = 6.340$	0.38	3772.2	2.408	1.7451

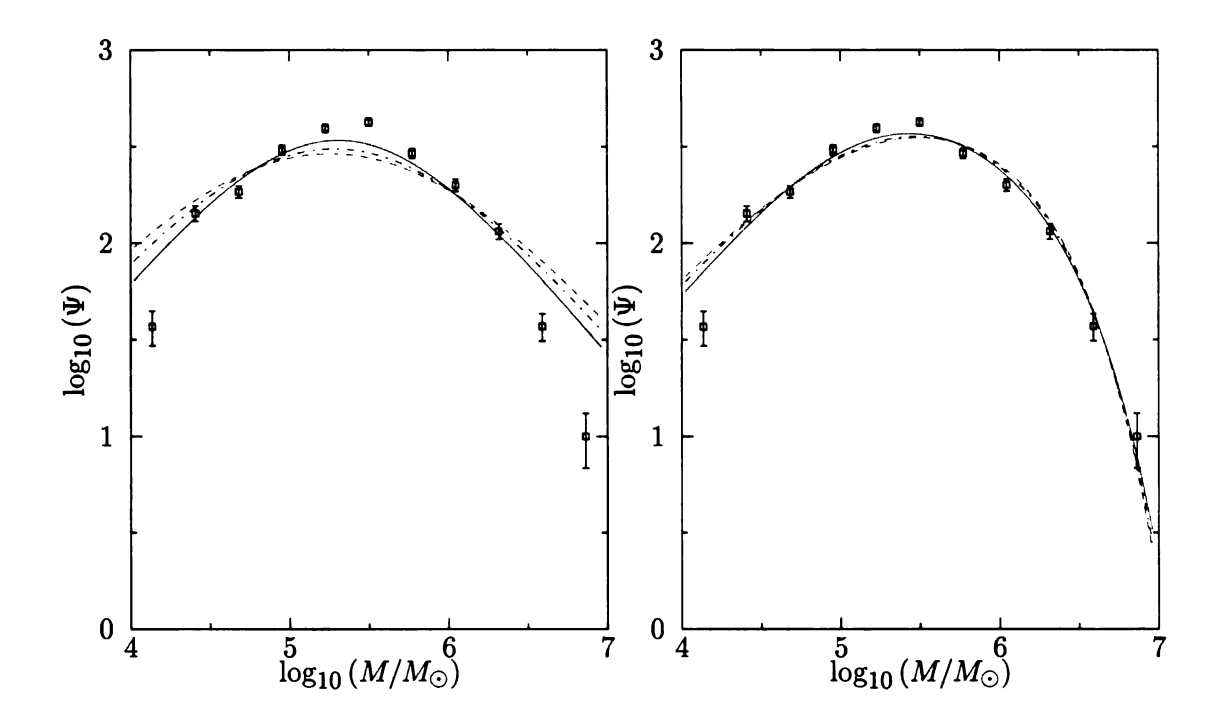


Figure 6.2 M87 GCMF with best fitting mass loss models. The left panel shows models with powerlaw IMFs, and the right panel shows models with Burkert & Smith (2000) IMFs. Fit parameters are given in table 6.1. The mass dependence for the models are  $M^{0.0}$  (red solid line),  $M^{-0.25}$  (blue dot dashed line), and  $M^{-0.38}$  (green dashed line).

#### 6.3.1 Comparison to Mass Loss Models

We can compare these best fitting values to the expected values of  $\tau$  from the mass loss coefficients in each of the models. For the Fall & Zhang (2001) case, this is easy, as  $\tau$  is simply equal to  $\mu_{\rm ev} \cdot t_{\rm lifetime}$ , or

$$\tau_{FZ} = 269\xi_e (G\rho)^{1/2} m \ln \Lambda t_{\text{lifetime}}$$
(6.20)

Taking the lifetime to be 12 Gyr,  $\xi_e = 0.045$ ,  $m = 0.7 M_{\odot}$ ,  $\ln \Lambda = 12$ , and using the value of  $\rho \sim 3.7 \frac{M_{\odot}}{pc^3}$  gives a value of  $\tau_{FZ} = 157200$ , which is close to the best fit

value.

For the other two models,  $\tau$  does not directly relate to the mass lost, but to some power of this quantity. Given the general form of the mass loss (equation 6.6), we can note that for a model with mass dependence  $M^{\gamma}$ ,  $\tau$  will have units of  $\frac{M_{\odot}^{\gamma}}{yr}$ . Regardless, the expected coefficient of such a model can be calculated from the dissolution time, by noting that all of the cluster's mass is gone by that time, such that  $t_{\rm diss} = \frac{M^{\gamma}}{\tau}$ .

The dissolution time for the Baumgardt & Makino (2003) model is given by equation 6.11, so

$$\tau_{BM} = \frac{1}{1.91} (m \ln \Lambda)^{0.75} \left(\frac{R_G}{1 \text{kpc}}\right)^{-1} \left(\frac{v}{220 \text{km/s}}\right) \left(\frac{1}{1 - \epsilon}\right) \left(\frac{t_{\text{lifetime}}}{1 \times 10^6 \text{yr}}\right)$$
(6.21)

Using the same quantities as above, and assuming a circular orbit where  $\epsilon=0$  and  $v=\left(\frac{GM_{enc}}{r}\right)^{1/2}\sim488 \mathrm{km/s}$ , this gives  $\tau_{BM}=12778\frac{M_{\odot}^{0.75}}{\mathrm{yr}}$ , also consistent with the best fitting value.

Repeating this same procedure for the Lamers et al. (2005) model dissolution time yields

$$\tau_{Lamers} = C_{env}^{-1} \left( 10^4 M_{\odot} \right)^{0.62} \left( \frac{\rho}{M_{\odot} \text{pc}^{-3}} \right)^{1/2} \left( \frac{t_{\text{lifetime}}}{1 \times 10^6 \text{yr}} \right)$$
(6.22)

where we take  $C_{env} = 810$ . This yields a value of  $\tau_{Lamers} = 8605.9$  that is much greater than the best fit values. To match the best fit value, we must change  $C_{env} \sim 1847.9$ , which greatly increases the lifetimes for these clusters compared to the Lamers et al. (2005) prediction, a result that is not surprising, given that  $C_{env}$  is based on samples that likely contain objects that are not fully bound.

#### 6.3.2 Mass to Light Ratio

As the cluster evolves, mass segregation moves the most massive stars to the core, and the lighter stars to the outskirts of the cluster. These light stars are then preferentially stripped from the cluster, leaving the fraction of more massive stars in the cluster to rise over time. The lightest stars contribute only slightly to the mass of the cluster, but contribute even less to the cluster luminosity. Therefore, as these stars leave the cluster, the mass to light ratio drops.

Generally, the mass to light ratio changes more dramatically due to the evolution of the stars in the cluster. However, for old GC populations such as M87, this effect can be assumed to be negligible, as the stars with short evolution times will have all evolved. The N-body simulations of Baumgardt & Makino (2003) track the effect the loss of individual stars has on  $\Upsilon$ , as well as the changes due to stellar evolution. They correct for the stellar evolution, giving just the changes due to dynamics. For simplicity, we model these changes as

$$\Delta \Upsilon \left( \frac{t}{t_{\text{dissolution}}} \right) = \begin{cases} 0.0; & \frac{t}{t_{\text{dissolution}}} < 0.2\\ \frac{1}{6} - \frac{5}{6} \frac{t}{t_{\text{dissolution}}}; & \frac{t}{t_{\text{dissolution}}} > 0.2 \end{cases}$$
(6.23)

with the initial mass to light ratio  $\Upsilon_0 = 3.0$ .

As it is the best fitting model, we use the  $\gamma = 0.0$ , Burkert & Smith (2000) IMF model to examine the effects of this changing  $\Upsilon$ . This also has the benefit that the fraction of life is easy to calculate

$$\frac{t}{t_{\text{dissolution}}} = 1 - \frac{M}{M + \tau} \tag{6.24}$$

due to the linear nature of the mass loss. This allows the individual cluster masses to be corrected for the changes in  $\Upsilon$ . As this depends on the fit value of  $\tau$ , the correction and the fit must be iterated until a stable solution is found. The final fit gives a smaller value for  $\tau$ , but with a better value of  $\chi^2$ . This new best fitting  $\tau$  also matches much better with  $\tau_{FZ}$ , suggesting that the changes in mass to light are significant to the low mass end of the GCMF. Table 6.2 presents the best fitting model for the data using this variable mass to light ratio, and the fit is shown in

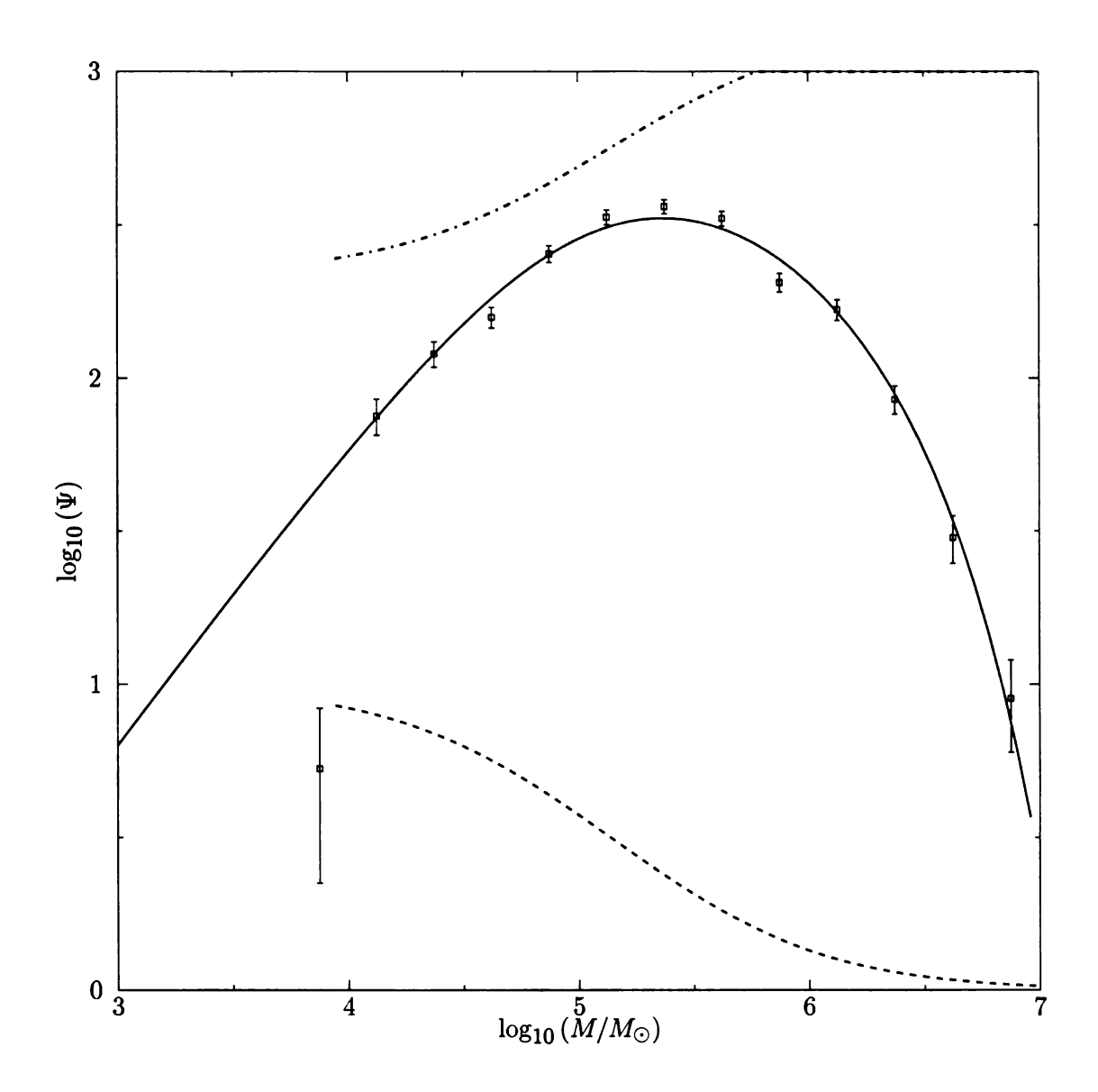


Figure 6.3 Best fitting mass loss model, incorporating the variable mass to light ratio from Baumgardt & Makino (2003). The dashed line shows the calculated  $t/t_{\rm diss}$  for the mass, and the dot dashed line shows the mass to light ratio used at each mass.

Table 6.2: Best fitting mass loss fits incorporating variable mass to light ratio.

Dataset	Burkert & Smith (2000) $\log_{10}(M_C)$	γ	τ	A	$\chi^2$
ACS	$\log_{10}(M_C) = 6.419$	0.00	149604	2.311	0.7587
${ m WFPC/2}$	$\log_{10}(M_C) = 6.350$	0.00	155177	1.996	0.7979
Harris (1996)	$\log_{10}(M_C) = 6.046$	0.00	113297	0.936	0.9486

#### 6.3.3 Comparison to Previous Results

Figure 6.4 shows how this new mass function compares to the one presented by Waters et al. (2006). The extra depth the new sample provides a tighter constraint on the mass loss rate, as the smallest clusters have more influence on the mass loss rate. The effects of the changing mass to light ratio also produce the effect predicted by Waters et al. (2006), that the premature loss of clusters was an artifact of such changes. When this new variable mass to light ratio method is used to fit the Waters et al. (2006) data, the results match up very well. The differences between the ACS and WFPC/2 mass loss rates are within 5% of each other.

We can also compare our results to those presented by Jordán et al. (2007) based on the results of the ACS Virgo Cluster Survey. They fit "evolved Schecter functions" to their data, similar to what is done here and in Waters et al. (2006) with our Burkert & Smith (2000) IMFs. Unfortunately, they do these fits in magnitude, forcing a conversion to our mass based units. For M87, Jordán et al. (2007) present the following values:

$$\langle \Upsilon \rangle = 2.67 \tag{6.25}$$

$$\delta = -7.287 \pm 0.089 \tag{6.26}$$

$$m_C = -9.850 \pm 0.232 \tag{6.27}$$

where we can convert these values to our units as

$$\delta = C - 2.5 \log_{10} \tau \tag{6.28}$$

$$m_C = C - 2.5 \log_{10} M_C \tag{6.29}$$

$$C = V + 2.5 \log_{10} M = 5.928 \tag{6.30}$$

This gives values  $\tau_{ACSVCS} = 197661.2$  and  $\log_{10} M_C = 6.321$ .

This neglects the fact that the F435W filter used by the ACSVCS does not directly match the profile of a V filter, but based on the reasonable agreement in the cutoff mass, this appears to work well regardless. The high value for  $\tau_{ACSVCS}$  derived in this manner, along with the truncation of their published luminosity functions indicates that they suffer from the same overestimate of the decay rate as the original Waters et al. (2006) data. In addition, as shown above, neglecting the dynamical effects on the mass to light ratio also tends to increase the best fit values of  $\tau$ .

The Harris (1996) Milky Way sample was also fit, although the number of clusters used is far smaller. It is interesting to note that the best fitting cutoff mass is significantly lower in the Milky Way.

#### 6.3.4 Color Dependence of the Mass Loss

The analysis of the red and blue GCLFs indicated that the distributions were significantly different than each other. We can investigate this further by examining the best fit mass loss models for these samples. Due to the splitting of the sample, we are restricted in how small a mass we can reliably fit. For both samples, the clusters below  $\log_{10} M \sim 4.5$  were excluded, as the evolution of  $\Upsilon$  depletes the bins in such a way as to bias the fits to large mass loss rates. Figure 6.5 shows the GCMFs for the two samples, along with their best fitting mass loss models.

This plot clearly shows that the blue sample has a higher cutoff mass than the

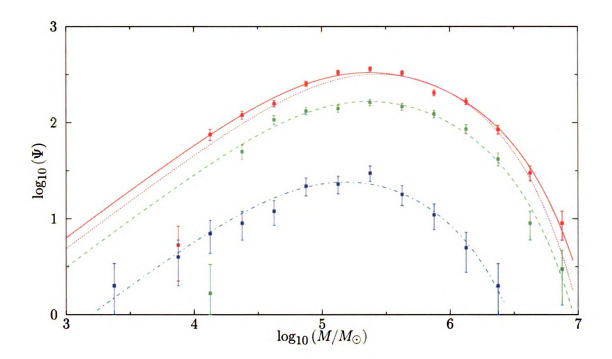


Figure 6.4 Comparison of this GCMF (red) to that presented by Waters et al. (2006) (green). The mass functions are scaled to provide the same normalization, and the best fitting mass loss models are shown for both. Note how the added depth in the new data offers better constraints on the mass loss. In addition, the best fit model from Jordán et al. (2007) is plotted for this new ACS sample (pink dotted), and the Milky Way data of Harris (1996) along with the best fit mass loss model (blue).

red sample (log  $M_{C\,\mathrm{blue}}=6.45$ , log  $M_{C\,\mathrm{red}}=6.32$ ). This is a rather significant shift, corresponding to a 30% difference in the masses for the clusters at the turnover. Such a large difference may be explained by a simple difference in the mass to light ratios due to the metallicity differences, as such changes can range up to around 10% (Ashman et al., 1995).

As the metal poor clusters are believed to be older, any evolutionary effect should be more pronounced on those clusters. Without such a signature, it seems unlikely that some high mass evolutionary effect can explain this difference.

The mass loss rates found by the best fitting models show that the blue clusters do seem to have lost more mass than the red ( $\tau_{\text{blue}} = 205113$ ,  $\tau_{\text{red}} = 130304$ ). This

is to be expected, as stellar evolution is linear with time, so the older blue clusters will have lost more of their mass over time. However, directly taking these values of  $\tau$  suggests that the blue population is nearly twice as old as the red population. This is unreasonable, and suggests that the fit values may be biased due to the lack of the lowest mass clusters.

However, if we shift the cutoff masses to be equivalent (in other words, assuming that the metallicity dependence of  $\Upsilon$  explains the effect fully), we can determine the new mass loss for the models. Holding  $\log_{10} M_{C\,\mathrm{red}}$  constant, we find a new fit to the blue clusters where  $\tau_{\mathrm{blue}} = 152052$ . If we assume that the mass loss is the same for both types of cluster, this gives a ratio for the ages of the red and blue clusters as

$$\frac{t_{\text{lifetime red}}}{t_{\text{lifetime blue}}} \sim 0.87 \tag{6.31}$$

For the nominal age of 12 Gyr for the blue clusters, this suggests that the red clusters formed about 1.5 Gyr later, consistent with expectations.

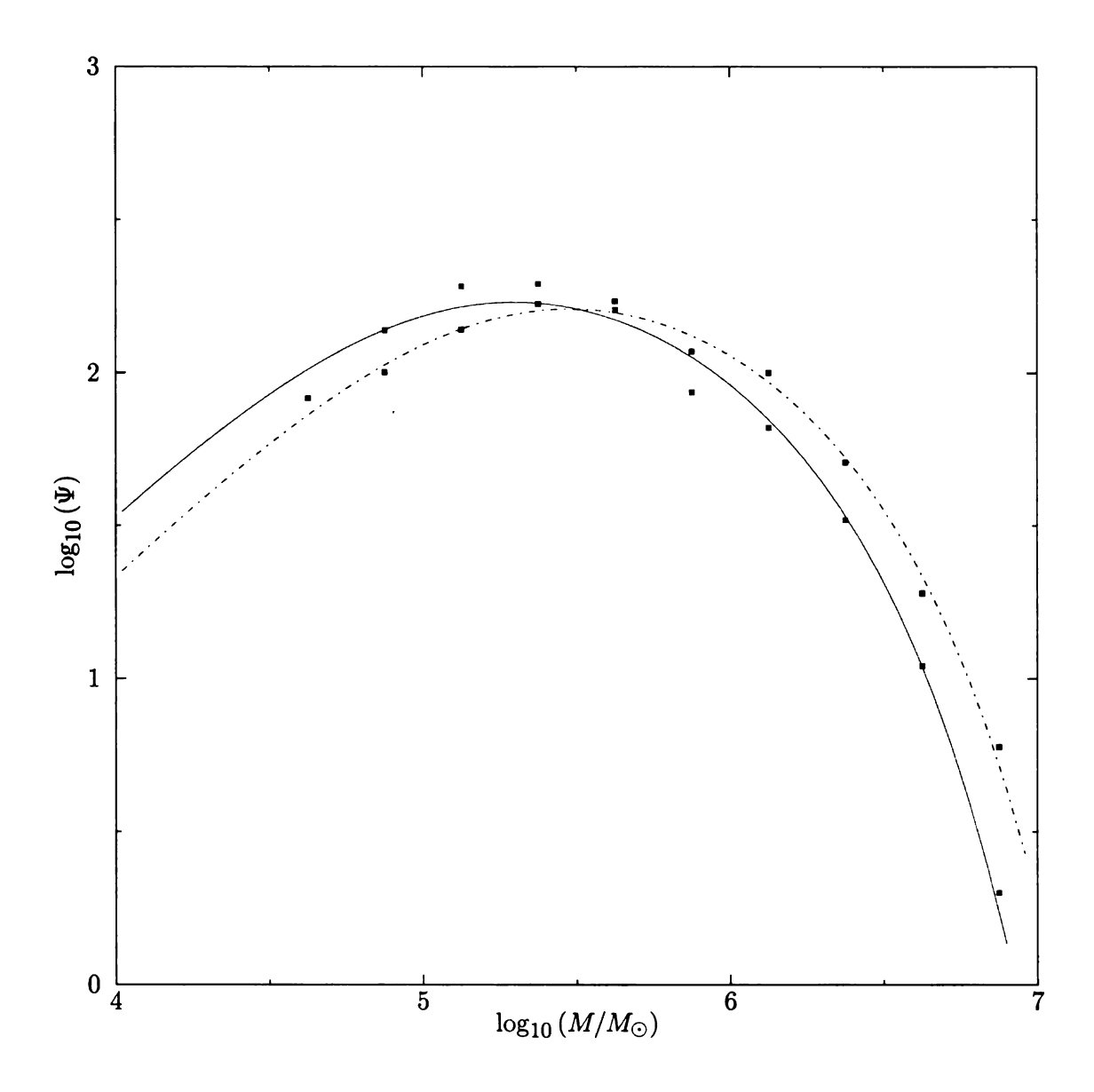


Figure 6.5 Comparison of the GCMFs for the red and blue samples. The blue sample clearly has a higher cutoff mass, and as it turns over faster, a larger amount of mass loss.

## CHAPTER 7: STRUCTURAL PARAMETER FITTING

The superior resolution offered by our data opens up the possibility of looking at more than simply the brightness of the clusters. The fact that the cluster widths are significantly wider than the local PSFs indicates that we are resolving the actual structure of the cluster. By generating simulated clusters, and matching these templates to the data, we can estimate the parameters of that real cluster. The program superking (see Appendix A.2) was written to perform the generation and fitting of simulated clusters. Briefly, superking reads in a list of extracted GC images and associated PSFs, estimates the initial parameters from the data image, and then uses a variety of fitting stages to calculate the set of parameters that yield the best  $\chi^2$  value.

As discussed in chapter 2, only three parameters are generally needed to fully define a King model: the concentration, any of the defined radii, and a brightness calibration. We have chosen the tidal radius and the total cluster flux to define our models, but due to the relations between the model parameters, any equivalent choice would be equally valid (say, the core radius and the central surface brightness). In addition to the parameters that define the model, there are parameters related to how the cluster projects onto the image plane. As the sampling of the model can change significantly with small changes in the center of the cluster, we must include the peak position of the cluster,  $x_0$  and  $y_0$ , as parameters in the fits. This must be fit as part of the template, as asymmetries in the PSF can skew a simple centroid away from the "true" value. Finally, since the local background is not guaranteed to be exactly

zero, a constant background level is also added to the parameters.

Other parameters can be added to this list, but, in general, are less important to the fit quality. The PSF centering can be allowed to move, to more accurately represent the effects of the pixel response function on subpixel shifts in the centering. This was included in the fitting, but most PSF shifts are negligible, so this parameter tends not to change much during fitting. The cluster ellipticity can also be included by laying the model onto a template image as a function of semi-major axis instead of a simple radius. However, this is not included in the King model formalism, and the definition of the tidal radius is not well constrained for such an objects. As we have required all cluster candidates to have at most  $\frac{A_E}{B_E} = 1.5$ , we should have few highly elliptical objects in the fitting sample, so this parameter can be safely excluded.

The data images are constructed by extracting a box of  $128 \times 128$  pixels centered on the cluster peak. These were drawn from the F814W image that had been drizzled to twice the nominal ACS resolution, such that 1 pixel = 0.025. The choice was made to use this instead of the single resolution data as the increase in resolution provides more pixels on a given cluster, so even though the signal decreases, the quality of a given fit is better constrained. The image size was chosen to correspond to a projected radius of  $\sim 128$  pc, which is larger than the tidal radii of most Milky Way globular clusters. Therefore, all extracted images should fully contain the GC.

#### 7.1 ERROR ANALYSIS

Even before running the fitting, it is clear that by fitting six main parameters by minimizing the  $\chi^2$ , there will be some degeneracy in the fits. This can cause coupled errors between the best fitting values. The first source of error is between  $x_0$ ,  $y_0$ , and  $r_c$ . This arises from the fact that miscentering the cluster forces the fit to move light away from the model peak to accommodate the peak in the data, leading to a model with a higher core radius. A similar effect can be caused from errors in the PSF. If

the PSF used for fitting is wider than the true PSF, then the best fitting model will have a smaller core radius to ensure that the final convolved simulated cluster has the correct effective width.

The largest problem in the fitting couples c,  $r_t$ , cluster magnitude, and the background level together. This coupling is easiest to visualize by assuming an error in the background level in which  $B_{\rm Fit} > B_{\rm True}$ . In this case, the best fitting tidal radius will be smaller than the true value, as any wide tails will be swallowed by the increased background level. Since the cluster is then smaller, fewer pixels are considered to be part of the cluster, so the best fit flux is also smaller. As the size of the core is changed little by this error, but the tidal radius has decreased, the fit concentration will be lower as well. The opposite case works similarly, with a smaller background creating clusters with larger  $r_t$ , larger F, and higher c.

Given the set of expected errors, it is reasonable to wonder how well any of these parameters can be fit. To test this, artificial globular clusters were generated for the full range of expected parameters. These fake clusters have Poissonian noise for the cluster light, as well as Gaussian noise with the value of  $\sigma$  chosen from the range observed in the data images. Looking at the quality of these fits and the variance in the parameters provides an estimate of how well we can believe the fits to the real data.

This estimate of the error does ignore two major sources of uncertainty. First, as the template images are created using the same PSF as they are fit with, they are certain to have better fits than any real data. The PSFs used are the best estimate of the true image PSFs, but are not likely to be perfect matches. This uncertainty will make the fits to the real data noisier in the core. The second problem is that the templates are made with Gaussian distributed noise over a fixed flat background. The real images often contain other globular clusters, and may not have such an idealized noise and background. This will cause issues with the background estimate, and as

discussed above, that can seriously alter the fit.

#### 7.1.1 Position Errors

Figure 7.1 shows the histograms of the position deviations from the simulated cluster fitting, along with the best fitting Gaussians to the distribution. It is clear that the simple position errors have wide wings that are poorly fit by the Gaussian model. However, incorporating the PSF offsets largely eliminates these wings. This points to the PSF offset changing the modeling only slightly, and working more as a second component of the positioning. If we compare the "effective centers," defined as  $x_0 - x_{\rm PSF}$ , between the input and output values, we can see that there are no offsets between the two ( $\Delta x = -0.0005$ ,  $\Delta y = -0.0007$ ) and very small scatter ( $\sigma_x = \sigma_y = 0.016$ ). This confirms that the centers found during the fitting process are exceptionally accurate.

#### 7.1.2 Magnitude and Background Errors

The error in the measured magnitudes is in general small ( $\sigma_M = 0.004$ ). For the faintest clusters, however (V > 25), there is an extended tail where the measured magnitude is even fainter. This suggests that the fitting routine fails to correctly identify and fit these clusters, and provides the limit for the faintest cluster that can be reliably fit.

The background is generally well measured, although the distribution is wider than a simple Gaussian. Figure 7.2 shows the scatter in the background as a function of the input magnitude, with the largest scatter coming from the brightest clusters. This is to be expected, as these bright clusters will tend to skew the statistics used for calculating the background. In addition, the objects in this sample with the largest scatter also are the clusters with the largest input tidal radii, which would also naturally lead to errors in the background, as these large clusters will serve to

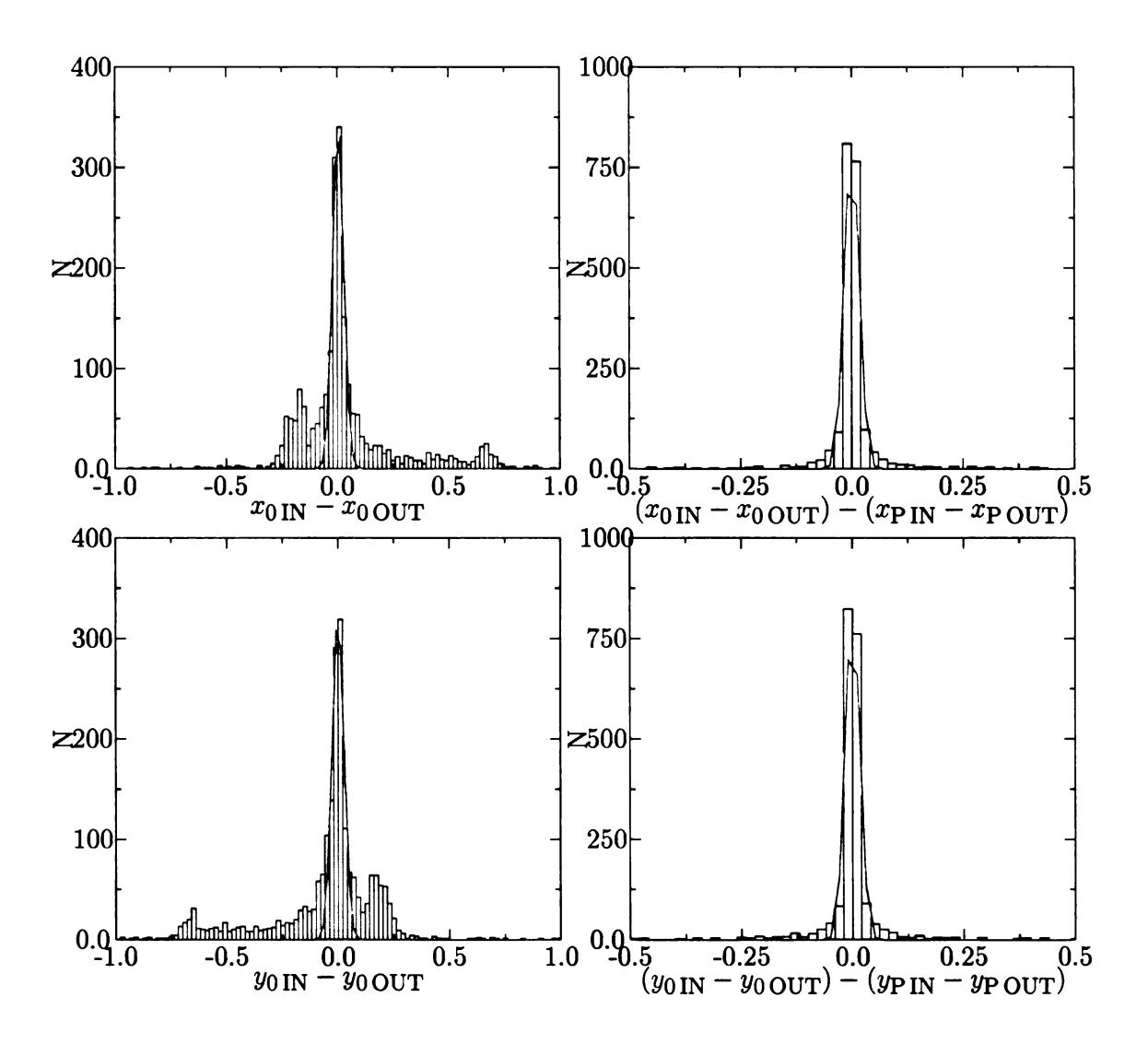


Figure 7.1 Expected errors in position from fitting simulated clusters.

raise the image average.

#### 7.1.3 STRUCTURE ERRORS

Given that the background shows a problem in fitting the largest clusters, it is reasonable to investigate how well the structure of such large clusters is fit. The central potential fits for these clusters are very good, but show a large scatter and offset in the best fitting  $R_t$ . A detailed check of the source of this scatter shows that the limit of reliable  $R_t$  fits occurs at  $R_{t\,\mathrm{IN}}\sim\frac{1}{2}\mathrm{image\,size}$ . This is an obvious limit, as larger

clusters are not fully contained on the fitting image, and so should not be expected to be fit well.

The effects of the input radius on the central potential fits show almost the exact opposite trend. The largest clusters have excellent fits to the central potential, due to the large number of pixels devoted to the central core. The small clusters, however, have a much larger scatter. This is reasonable, as such small clusters begin to all look like a point source. If we consider a fairly diffuse cluster, with c = 1.0, but then set  $R_t = 5$  pixels, then the central pixel will contain  $\frac{2}{3}$  of the total light of the cluster. This effect is even worse as the concentration increases, making all small clusters effectively point like. Using this as a guide, we can set a lower limit of  $R_t > 5$  pixels for reliable fits to the central potential.

#### 7.2 FITTING RESULTS

From the sample of all clusters detected, 1194 were chosen for fitting. These clusters were selected to be brighter than V=25, and were chosen to be the brightest clusters within 25 pixels. This spacing requirement was added to allow PSFs to be generated without problems from overlapping. Once the best fitting model was calculated with superking, the various derived parameters defined in section 2.4 were calculated as well. Given the results from the fitting of the simulated data, all clusters that have final tidal radii less than 5 pixels or greater than 64 pixels were excluded from further analysis. This leaves a final sample of 1096 clusters.

Figure 7.4 shows one of the extracted cluster images, along with the residual for the best fitting model. The deviations in the core are generally less than 5%, consistent with the expected error in the PSF. Based on this fact, it seems unlikely that any fit can be made with a better residual, without some new understanding of the PSF.

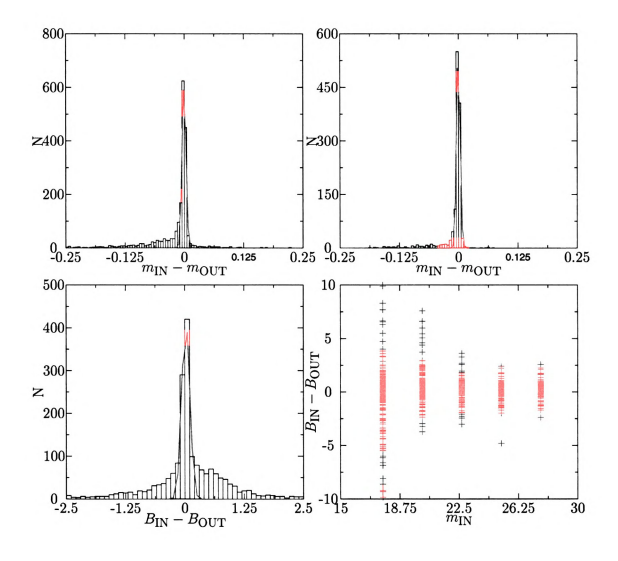


Figure 7.2 Expected errors in magnitude and background level based on fitting simulated clusters. The upper right panel shows the improvement in the magnitude errors when the clusters fainter than  $I \sim 25$  are excluded.

110

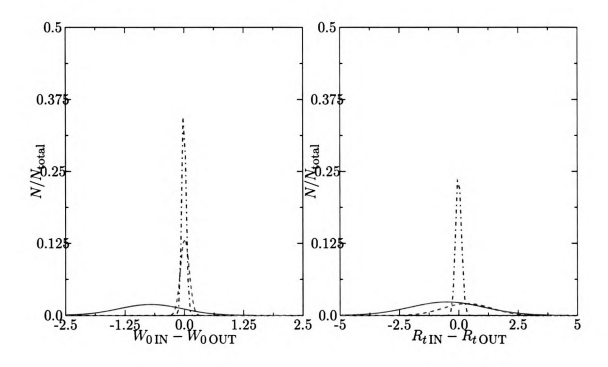


Figure 7.3 Expected errors in the structural parameters based on fitting simulated clusters. The red solid line shows the results for  $R_{t\,\rm IN} < 5$ , and the green dashed line for  $R_{t\,\rm IN} > 50$ . The blue dot dashed line is the result for the remaining clusters, showing the small scatter for such objects.

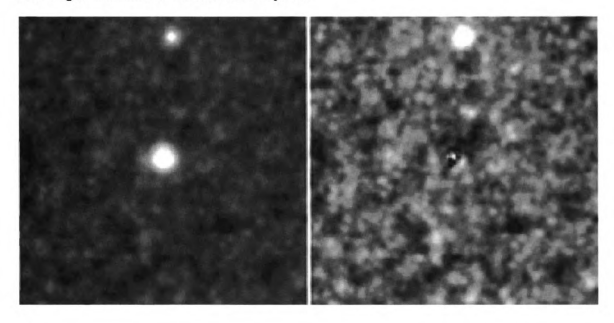


Figure 7.4 Original extracted cluster (x,y) = (4562,6772) and residual for best fitting model. The companion cluster near the top of the frame does not seem to skew the fitting at all.

# CHAPTER 8: GLOBULAR CLUSTER STRUCTURE RESULTS

Given this extensive sample of structural parameters, we can compare against the Milky Way results of Djorgovski & Meylan (1994). The Milky Way is obviously the best observed, and has a some advantages over any extragalactic sample. First, the true three dimensional distance from the center of the galaxy can be easily found, whereas only the projected distance is observed for M87. In addition, the small distances to the Milky Way clusters allows spectra to be taken in a reasonable amount of time, providing a direct measure of the central velocity dispersion of the stars. Finally, even the faintest clusters of the Milky Way have values for at least some of their structural parameters, and as discussed in Chapter 7, the fitting in our data is limited to  $V \sim 25$ .

Despite these issues, the M87 sample does have one main advantage over the Milky Way. The shear number of globular clusters ensures that for the range of parameters that can be fit, the results should be more statistically sound. Over the range in luminosities that we consider, Djorgovski & Meylan (1994) used 116 clusters (out of a total sample size of 143 clusters), giving this new sample nearly ten times the number of objects.

#### 8.1 EFFECT OF CLUSTER LUMINOSITY ON STRUCTURE

Figure 8.1 shows the relations between several structural parameters with the absolute V magnitude. These are plotted long with the Milky Way data taken from Harris (1996), which is effectively the same set of measurements used by Djorgovski & Meylan (1994). This figure shows that the two samples line up rather well, and illustrates that brighter clusters tend to be more concentrated, and have smaller cores than lower luminosity clusters.

These trends become more clear in figure 8.2, in which the M87 data is median binned in magnitude, with the error bars calculated using the non-parametric method presented by Djorgovski & Meylan (1994), where

$$\sigma = 0.7415(Q_{75} - Q_{25}) \tag{8.1}$$

where  $Q_{75}$  and  $Q_{25}$  are the 75th and 25th percentiles in the bin. This gives the same value as the standard deviation if the bin is populated with Gaussian distributed data, but in the case of data with many outliers, provides an estimate that ignores such points.

The binned data shows a clear trend of increasing concentration with brighter clusters. This trend continues up to  $M_V \sim -10$ , beyond which the concentration flattens out, with a constant concentration level for the brighter objects. This flattening may represent a failing in the quality of the fits for clusters with the smallest core radii. However, the binned results of Djorgovski & Meylan (1994) also show such a flattening above  $M_V \sim -9$ . This suggests that the effect may be real, and as the M87 data extends about two magnitudes brighter, we are simply seeing more of this flattening.

The enhancement in concentration also shows as a drop in the binned core radius over the same luminosity range. Djorgovski & Meylan (1994) fit this drop as  $r_c \sim$ 

 $L_V^{-0.5\pm0.25}$ , or in terms of magnitudes

$$\log_{10} r_c \propto 0.2 M_V \tag{8.2}$$

Fitting this trend over the full range of the M87 data gives  $\log_{10} r_c \propto 0.04 M_V$ , which does not match well. However, limiting the sample to only those clusters fainter than  $M_V \sim -9$  provides a fit of

$$\log_{10} r_c = 0.15 M_V + 0.943 \tag{8.3}$$

well within the error range given by Djorgovski & Meylan (1994)

As the central density increases with both increasing concentration and luminosity, it is not surprising that the trend in this parameter is fairly strong. The Djorgovski & Meylan (1994) fit gives  $\rho_0 \sim L_V^{2\pm 1}$ , or

$$\log_{10}\rho_0 \propto -0.8M_V \tag{8.4}$$

Restricting the fitting again to the range of magnitudes considered for the Milky Way, we find a trend of

$$\log_{10} \rho_0 = -0.69 M_V - 0.939 \tag{8.5}$$

for the M87 data, which again matches.

The lack of a trend between the half light radius with luminosity is a well known result for globular clusters, due to the fact that it contradicts what is observed for elliptical galaxies, which have larger effective radii with increasing mass. This constant half light radius has been observed in young cluster systems (Zepf et al., 1999; Larsen, 2004), which suggests that the half light radius is set during formation. The

M87 data provided a confirmation of this lack of trend, with

$$\log_{10} r_b = 0.013 M_V + 0.604 \tag{8.6}$$

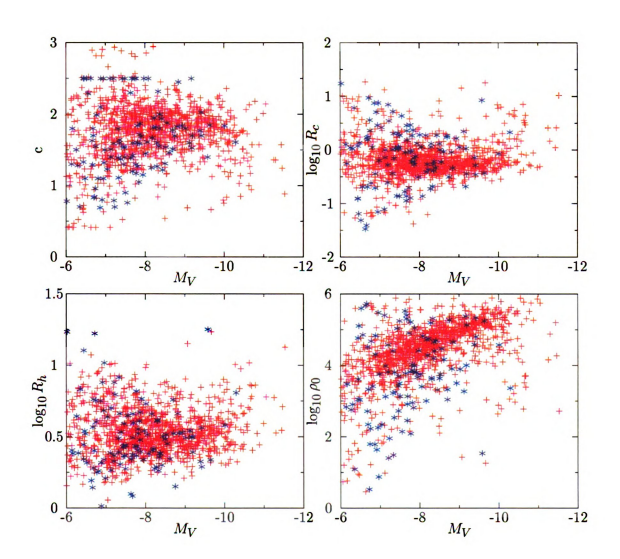


Figure 8.1 Parameter correlations with absolute magnitude. The red crosses are the new M87 data, and the green asterisks are the Harris (1996) data. All distances are in parsecs, and the central density is given in solar masses per cubic parsec.

#### 8.2 EFFECT OF DISTANCE ON STRUCTURE

The structure of globular clusters is expected to change with the distance from the center of the galaxies. The clusters that are close to the core will shrink due to the higher potential felt by the cluster, which in turn raises the concentration and central density. However, due to the projection effects, any such trend is washed out in this sample.

Figure 8.3 shows the trends with projected distance, although no attempt was made to try to fit trends to the data. Qualitatively, the clusters with the lowest concentration do seem to be at the largest projected distance. Similarly, the half light radii increases with distance. Unfortunately, without a good deprojection, no firm trends can be established.

#### 8.3 Relations Between Core Parameters

Djorgovski & Meylan (1994) also show the correlations between various core structural parameters, plotted here in figure 8.4. The fairly tight correlations are believed to be the result of clusters evolving toward core collapse. The central density of such a cluster is expected to follow the relation  $\rho_0 \sim r_c^{-2.23}$  (Binney & Tremaine, 1987), the same result found by Lynden-Bell & Eggleton (1980) by modeling core collapse in a thermally conducting gas. A fit to our data yields

$$\rho_0 \propto r_c^{-2.12}$$
(8.7)

remarkably close to the theoretical expectation.

# 8.4 THE FUNDAMENTAL PLANE OF GLOBULAR CLUSTERS

In addition to simple correlations between parameters, Djorgovski & Meylan (1994) noted that the parameters were related by a manifold of only three dimensions: a size, a shape, and a brightness. This is reasonable to expect, as globular clusters are reasonably well fit by King models, which have exactly the same parameters. Beyond this, Djorgovski (1995) determined that the parameters can be fit to "Fundamental Plane."

This plane is given in terms of the cluster surface brightness as

$$\mu_0 = (-4.9 \pm 0.2) (\log_{10} \sigma - 0.45 \log_{10} r_c) + (20.45 \pm 0.2)$$
 (8.8)

$$\langle \mu \rangle_h = (-4.1 \pm 0.2) (\log_{10} \sigma - 0.71 \log_{10} r_c) + (19.8 \pm 0.1)$$
 (8.9)

for the core and half light radii. Djorgovski (1995) notes that the core result can be transformed to match the virial theorem  $(r_c \sim \sigma^2 I_0^{-1})$ , and that the half light radius result can be transformed to match the fundamental plane result for elliptical galaxies  $(r_h \sim \sigma^{1.4} I_0^{-0.8})$ .

Unfortunately, this derivation for a fundamental plane requires information that we do not have for M87. However, if we accept that the clusters are fit by King models, then we can take advantage of a "cheat." We have defined the core radius as

$$r_c = \sqrt{\frac{9\sigma^2}{4\pi G\rho_0}} \tag{8.10}$$

This  $\sigma$  is formally the 3-d velocity dispersion, and not the line of sight dispersion measured by spectra and used for the fundamental plane relations. However, McLaughlin (2000) shows that for concentrations greater than  $c \sim 1$ , these two values deviate by less than 10% from each other. Therefore, we can trade the central density to get a

velocity dispersion. Doing this, and then fitting the best plane to the M87 data yields

$$\mu_0 = -5.0 \left( \log_{10} \sigma - 0.53 \log_{10} r_c \right) + 21.4$$
 (8.11)

$$\langle \mu \rangle_h = -5.0 \left( \log_{10} \sigma - 0.60 \log_{10} r_c \right) + 21.16$$
 (8.12)

which are very close to the cited fundamental plane relations.

A closer look at the cheat indicates that our calculation of  $\rho_0$  is based directly on values of  $\mu_0$  and  $r_c$  (equation 2.53). Therefore, if simply rearranging the structural parameters can provide a "fundamental plane," for this data set that closely matches those published, then it suggests that the fundamental plane is not a surprising effect, but merely the consequence of the fact that globular clusters are well defined by King models.

#### 8.5 LMXB PROBABILITY

Low mass X-ray binaries (LMXBs) are binary star systems in which one star overfills its Roche lobe, dumping mass onto the companion star. This companion is assumed to be a compact object, like a neutron star or black hole, as the X-ray luminosity is so great. The source of these X-rays is believed to be gas that is heated as it spirals into the companion gravity well. These LMXBs have been found with surprisingly high numbers in globular clusters, leading to the theory that these objects are formed when two previously unrelated stars form a close binary due to stellar interactions. Such an event would be vastly more likely to occur in the dense stellar environment of a globular cluster than in the field.

To investigate these objects in the M87 sample, we used the catalog of X-ray sources in Jordán et al. (2004) and matched the objects against our catalog of globular clusters. Figure 8.5 shows the structural parameters and CMD for the objects matched, along with the general cluster population. As has been noted by many au-

thors before (Jordán et al., 2004; Sivakoff et al., 2007; Kundu et al., 2007), the bright clusters and the more metal rich (or redder) clusters are more likely to host LMXBs.

Furthermore, the structural parameter data suggests that for the GCs that host LMXBs that are not among the brightest clusters, those clusters with high concentrations (or equivalently, small core radii and high central densities) are the most likely. This is consistent with the LMXB probability being a function of the stellar encounter rate

$$\Gamma \propto \frac{\rho_0^2 r_c^3}{v} \sim \frac{\rho_0^2 r_c^3}{\sigma} \sim \rho_0^{1.5} r_c^2$$
 (8.13)

As shown above (section 8.4), both of these parameters tend to scale with the cluster luminosity, so this effect is not surprising. However, by looking at the plot of  $\Gamma$ , we can see that at a given magnitude, clusters with LMXBs tend to have the most extreme values of  $\Gamma$ .

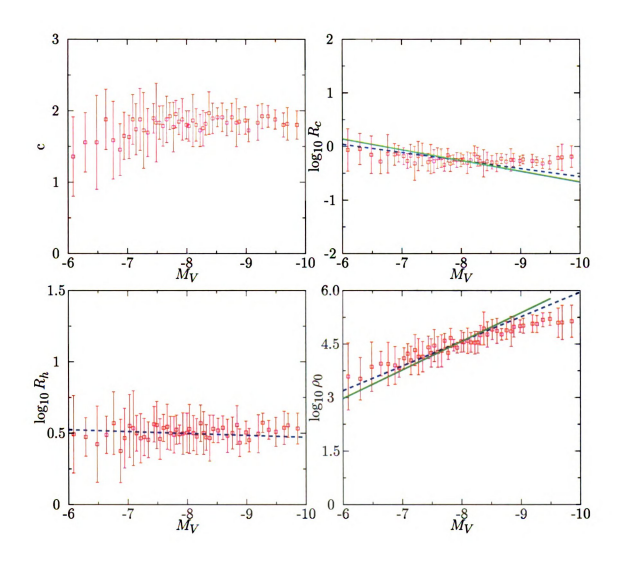


Figure 8.2 Parameter trends in averaged bins of luminosity. The solid green lines show the best fit trends from Djorgovski & Meylan (1994), and the dashed blue lines the new M87 fits.

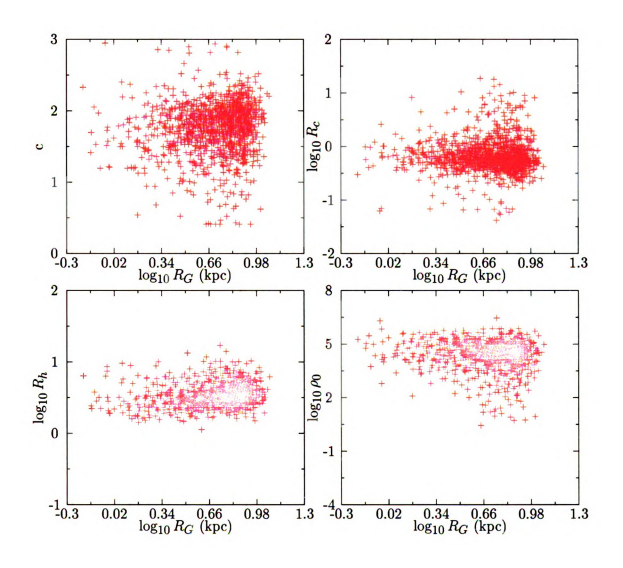


Figure 8.3 Parameter correlations with projected galactocentric distance.

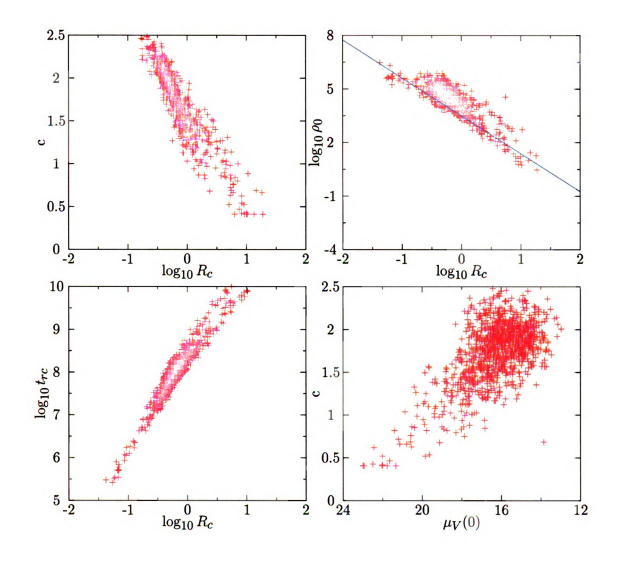


Figure 8.4 Correlations between core structural parameters. The blue line shows the trend of central density with core radius.

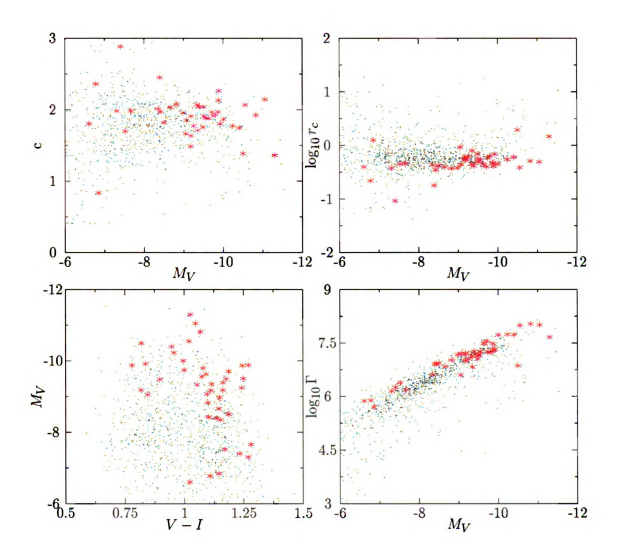


Figure 8.5 Plot of the locations of LMXBs with various structural parameters. The small dots show the general cluster population, with the asterisks denoting clusters that host LMXBs.

### CHAPTER 9: CONCLUSIONS

The data used for this thesis have shown that very deep images of galaxies can provide a wonderful opportunity to investigate the evolution and structure of globular clusters. Although there are likely few datasets that have the same depth as the one used for this project, other galaxies that are closer can easily be adapted to use the same methods. However, it is clear that space based observing provides a tremendous advantage over ground based imaging, due to the enhanced resolution.

The globular cluster luminosity function observed for M87 is consistent with previous space based surveys. The dispersion measured for this new sample does tend to be larger than those found previously, likely due to the truncation of the GCLF in that shallower and less complete data. Although the bimodality of cluster colors has been observed before, this sample shows no evidence for a mass-metallicity relation that some recent studies have found. Since the data presented here is so much deeper and better sampled, it seems likely that and the appearance of such a relation is simply the effect of photometric errors. By separating the cluster luminosity function into radial bins, it is clear that the bins closer to the core of the galaxy have brighter mean values and smaller dispersions. This result is entirely consistent with the expectation of enhanced mass loss from clusters in those regions.

The effect mass loss has on the shape of the cluster luminosity function becomes even more clear after considering the cluster mass function. The observed mass function is fit very well by considering mass loss only due to the effects of evaporation from two-body relaxation. By accounting for the changes in the cluster mass to light ratio from the preferential loss of the lowest mass stars, the observed mass loss rate is consistent with theoretical predictions. The mass function also explains the differences that are seen between the GCLFs for the red and blue cluster samples. The shift in the blue peak to brighter luminosities is due to a lower mass to light ratio for these clusters compared to the red sample. After accounting for this, the peak masses are effectively the same between both samples. Assuming that both types of cluster lose mass via the same mechanism, then the smaller observed dispersion in the blue GCLF is likely due to those clusters being older and having lost more of their total mass due to that difference in age.

The high resolution images used for this project show that reliable King model structural parameters can be measured, even at the distance of the Virgo cluster. The trends between these parameters appear to be universal, as the relations between the cluster structure and luminosity observed for the Milky Way match well with those found for M87. However, care must be taken when finding relations between the various parameters. As globular clusters are well fit by King models, the observed parameters are coupled together by the definition of such a model. Specifically, the proposed "fundamental plane" for globular clusters appears to simply be an artifact of this parameter coupling.

As has been observed before, low mass X-ray binaries are more likely to be found in clusters that are brighter and more metal-rich. As these objects are believed to form due to the capture of a star to a compact object to create a close binary, they probability of finding an LMXB should correlate with the rate of stellar interactions,  $\Gamma$ . This interaction correlates strongly with luminosity, obscuring which parameter is most important. However, for the fainter clusters, only those clusters with larger than normal values of  $\Gamma$  are found to host an LMXB, suggesting that stellar interactions are the important factor.

**APPENDICES** 

# APPENDIX A: DETAILED SOURCE CODE

## A.1 LIBKINGMODEL

LIBKINGMODEL is a C library written as part of this thesis to simplify the creation and evaluation of King (1966) models. In addition to creating the one dimensional volume and surface densities, it can also project this onto a two dimensional image, and perform the convolution with an instrumental PSF. The library is linked against the Gnu Scientific Library (GSL, http://www.gnu.org/software/gsl/), the FFTW Fast Fourier Transform library (http://www.fftw.org/), and CFITSIO (http://heasarc.gsfc.nasa.gov/docs/software/fitsio/) to handle many numerical methods, and to allow standard fits images to be used.

In general LIBKINGMODEL is very fast, able to generate a complete template image from scratch in about a second on a 1 GHz processor. Individual model generation is faster than this, although the dominant component of the execution time remains in solving the King model differential equation.

There are two main structures used in the library. The <u>kingmodel</u>, which contains the 1D model, and the <u>kingmodel\_template</u>, which holds the 2D image information. The <u>kingmodel</u> internally calculates the main defining parameters of the model: the central potential  $(W_0)$ , the core  $(r_c)$  and tidal radii  $(r_t)$ , and the King concentration (c). All of these are in an undefined "internal unit" system, as are the volume and surface densities. Since these parameters are generally normalized after the fact, this is not major problem.

#### A.1.1 KINGMODEL.C

The functions defined in this file handle the allocation, generation, and evaluation of the one dimensional King model.

- <u>kingmodel \* km\_model\_alloc(int size)</u>; This function allocates a <u>kingmodel</u> structure pointer for evaluation. The <u>size</u> parameter denotes how many radial samples are used for the model.
- void km\_model\_free(kingmodel \*M); This destroys a kingmodel pointer, and frees all
  memory associated with it.
- void km\_model\_solve(kingmodel \*M, double W0); This solves the King model with specified central potential W0, and stores the calculated volume density. The differential equation for the model density comes from Poisson's equation, where

$$\frac{d}{dr}\left(r^2\frac{dW}{dr}\right) = -4\pi G r^2 \rho_1 \left(e^W \operatorname{erf} \sqrt{W} - \sqrt{\frac{4}{\pi}W}\left(1 + \frac{2}{3}W\right)\right) \tag{A.1}$$

as the density can be written in terms of the reduced potential as

$$\rho(W) = \rho_1 \left( e^W \operatorname{erf} \sqrt{W} - \sqrt{\frac{4}{\pi}W} \left( 1 + \frac{2}{3}W \right) \right)$$
 (A.2)

This second order differential equation can be solved by breaking it into two first order differential equations

$$\frac{dW}{dr} = Y \tag{A.3}$$

$$\frac{dY}{dr} = -4\pi G\rho(W) - \frac{2}{r}Y \tag{A.4}$$

This system of differential equations is solved using a very accurate 8th order Runge-Kutta Prince-Dormand solver from GSL. This method requires the Jacobian of the system, which is easy enough to find:

$$J = \begin{pmatrix} 0 & 1\\ -4\pi G \left( e^W \operatorname{erf} \left( \sqrt{W} \right) - \sqrt{\frac{4}{\pi}W} \right) & -\frac{2}{r} \end{pmatrix}$$
 (A.5)

The first step to solve the model is to calculate the core radius,  $r_c = \sqrt{\frac{9}{4\pi G\rho(W_0)}}$ . The next step is to find the King tidal radius, where W becomes zero. Unfortunately, there is no analytic solution for this. Instead, it is found by using a binary search algorithm to bisect the range of values considered until the range becomes very small. The final range is then the uncertainty in the tidal radius, and is restricted to be smaller than  $1 \times 10^8 \cdot r_c$ . Although this is a fairly stringent constraint, the speed of the binary search algorithm allows this to be found with only a dozen or so iterations.

Once the tidal radius is found, the radius is divided into samples. The first five points are fixed to have the values

$$\frac{r}{r_t} = \left\{0.0, 1 \times 10^{-10}, 1 \times 10^{-8}, 1 \times 10^{-6}, 1 \times 10^{-4}\right\}$$
 (A.6)

to ensure that the very core of the cluster is reasonably sampled. The remaining points are distributed logarithmically, such that

$$\log_{10}(r_{\rm i}) = \log_{10}(r_t) \times i/\underline{\text{size}} \tag{A.7}$$

With the radius array filled, the volume density is then evaluated at each sample radius, and the values stored as well.

Once both arrays have been filled, GSL is used to construct a cubic spline through all the data points. This ensures that the evaluation can be performed quickly at all radii, and that no further calls to solve the differential equation are needed. This spline is also stored in the <u>kingmodel</u>. Finally, the tidal radius is solved once more, to determine the cutoff for the spline. This stage usually only corrects the tidal radius slightly, and is done to check the limit beyond which the spline cannot be evaluated anymore. This new tidal radius is then used to calculate the model concentration.

void km\_model\_project(kingmodel \*M); This function projects the volume density into a surface density. GSL is again used to perform this integration. The standard integral for projection is

$$\Sigma(R) = 2 \int_{R}^{r_t} \rho(r) \frac{r}{\sqrt{r^2 - R^2}} dr$$
 (A.8)

but, by noting that we can write  $f = \rho(r)$  and  $\frac{dg}{dr} = \frac{r}{\sqrt{r^2 - R^2}}$ , we can use integration by parts to remove the singularity from the integral:

$$\Sigma(R) = 2\left(\left(\rho(r)\sqrt{r^2 - R^2}\right)_R^{r_t} - \int_R^{r_t} \frac{d\rho(r)}{dr} \sqrt{r^2 - R^2} dr\right)$$
(A.9)

which then allows a faster and simpler integration method to be used that does not need to work around the point where r=R. This can be simplified further, as we can notice that the first term is zero at both endpoints. This leaves the projection integral in terms of the volume density derivative, which is easy to calculate with the spline implementation. This integral is evaluated on the same set of radial points as the volume density, and a spline is created for it as well.

<u>kingmodel \* km\_model\_simple(double WO);</u> For quick cases in which only a single model is needed, this function allows a <u>kingmodel</u> to be allocated, and the model with central potential <u>WO</u> solved and projected in one step.

double km\_model\_eval\_rho(kingmodel \*M, double r);

double km\_model\_eval\_drho(kingmodel \*M, double r);

### double km\_model\_eval\_surf(kingmodel \*M, double r);

double km\_model\_eval\_dsurf(kingmodel \*M, double r); These four functions evaluate the King model at a specified radius, and return the value of the  $\rho(r)$ ,  $\frac{d\rho(r)}{dr}$ ,  $\Sigma(R)$ , or  $\frac{d\Sigma(R)}{dR}$ . The radius is again in the internal radius units, and so needs to be converted using the stored kingmodel tidal or core radius.

#### A.1.2 KINGIMAGE.C

The functions in this file handle the creation of template images that contain a two dimensional representation for a <u>kingmodel</u>. The layout parameters and image data are stored in the kingmodel\_template structure.

kingmodel\_template \*km\_template\_alloc(int size); This allocates space for the image data on a square image of length size.

# void km\_template\_init(kingmodel\_template \*T,

double x0,double y0,double pxl\_tidal\_radius); This function sets the center and tidal radius scale for use in the filling stage.

#### void km\_template\_fill(kingmodel \*M,kingmodel\_template \*T,char \*method);

This fills the template image with the specified <u>kingmodel</u> surface density data. The <u>method</u> can be either <u>Sampled</u> or <u>Elliptical</u>, although only the <u>Sampled</u> method has been thoroughly tested.

The <u>Sampled</u> method functions by first assuming that the model has circular symmetry. It then evaluates the projected radius as

$$R^{2} = (x - \operatorname{int}(\underline{x0}))^{2} + \left(y - \operatorname{int}(\underline{y0})\right)^{2}$$
(A.10)

This ensures that the peak of the cluster is located on a pixel corner. The phase values for the template,  $\underline{\mathtt{phi}}_{\underline{\mathtt{x}}} = \underline{\mathtt{x0}} - \mathrm{int}(\underline{\mathtt{x0}})$  and  $\underline{\mathtt{phi}}_{\underline{\mathtt{y}}} = \underline{\mathtt{y0}} - \mathrm{int}(\underline{\mathtt{y0}})$ , are

then stored to be applied following convolution. This is a necessary step, as simply laying the pixels out directly will tend to underestimate the core value for highly concentrated models after convolution.

The 'Elliptical' method works in a similar fashion, using a radius equation

$$R^{2} = \left( (x - \underline{x0}) \cos(\underline{\text{theta}}) + (y - \underline{y0}) \sin(\underline{\text{theta}}) \right)^{2} + \left( \left( -(x - \underline{x0}) \sin(\underline{\text{theta}}) + (y - \underline{y0}) \cos(\underline{\text{theta}}) \right) / \underline{E} \right) \quad (A.11)$$

where <u>theta</u> is the position angle of the major axis, and  $\underline{\mathbf{E}}$  is the ellipticity. This method is not recommended, as it does not ensure the core is properly sampled, nor does it correctly model the cluster as an elliptical object, but merely skews the standard spherical form.

void km\_template\_normalize(kingmodel\_template \*T,double flux); This function normalizes the image in a kingmodel\_template to have total counts flux.

#### void km\_template\_free(kingmodel\_template \*T);

This destroys the kingmodel\_template, and frees all associated memory.

#### A.1.3 KINGCONVOLVE.C

As this library is designed largely to help fit King models to observed data, the generated images must be convolved with the PSF of the detector. This file contains the functions needed to perform this convolution using the FFTW fast Fourier transform library.

#### void km\_template\_plan(kingmodel\_template \*T);

To perform the Fourier transforms, FFTW requires "plans" to be generated to speed up the calculation. This function generates the plans necessary for a given template. This only needs to be done once for a given template, as it depends

only on the template size.

#### void km\_template\_convolve(kingmodel\_template \*T, fitsimage \*PSF);

This performs the actual convolution with <u>PSF</u>. The PSF data is first padded to the size of the template image, and then shifted so that the peak value is on pixel (0,0). The PSF data is wrapped around the edges, which ensures that after the convolution, no unwanted shifts are introduced.

Following this, both the template and the PSF are transformed into the Fourier domain, and convolved by multiplying the complex values pixel by pixel. This product image is then transformed back to the real domain, yielding the convolved image. This image is then normalized to unit flux. If the values of <a href="mailto:phi\_x">phi\_x</a> and <a href="mailto:phi\_y">phi\_y</a> are not zero, the convolved image is shifted back to the correct centering.

void km\_template\_shift(kingmodel\_template \*T); This function performs the shift
to remove the effects of phi\_x and phi\_y using a bicubic interpolator.

#### A.1.4 KINGUTILS.C

This file contains miscellaneous routines, largely for converting between the various model parameters. Since these parameters are functions of a given King model, they are included here.

double km\_concentration\_to\_WO(kingmodel \*M, double c); The concentration for a given  $W_0$  can be found by simply evaluating the model. This function works the other way, searching for the value of  $W_0$  that has a concentration of  $\underline{c}$ .

double km\_integrate\_flux(kingmodel \*M, double R); This function finds the total flux (in the internal units) enclosed within a given projected radius.

double km\_find\_rhalf(kingmodel \*M); This finds the radius that contains half of the total flux of the cluster.

#### void km\_scale\_radii(kingmodel \*M, double rt, double \*rc, double \*rh);

This calculates the core and half light radii that correspond to the given kingmodel, and have tidal radius <u>rt</u>.

#### void km\_calculate\_surface\_brightness(kingmodel \*M, double mag,

double pixel\_scale, double \*mu0, double \*meanmu\_half);

This calculates the central and half light surface brightnesses for a cluster of given mag and pixel\_scale in arcseconds.

#### void km\_calculate\_central\_density(kingmodel \*M, double mag,

double pixel\_scale,double distance, double \*rho0);

Calculates the central mass density for the model in solar masses per cubic parsec.

# A.2 SUPERKING

Superking is a program to determine the best fitting single mass King (1966) model to a given globular cluster image. It automatically finds the best central potential, tidal radius, center, cluster magnitude, and background level, with few required inputs.

The default way to run superking is to simply specify an extracted GC image and a corresponding PSF. Alternatively, a list of GC and PSF images can be specified in a file, and **superking** will proceed to fit all the images. The options supported by the program are as follows:

- -help, -h Display a list of the options available, and a usage summary.
- -list, -L Read a list of GC and PSF image pairs from a file.

- -gain, -g Specify the image gain for the GC images. The fitting is performed in units of electrons, so the gain is required for the conversion.
- -readnoise, -r Give the detector read noise to be included in the noise calculation.
- -zeropoint, -z The zeropoint used for converting the measured flux into an instrumental magnitude.
- -background, -K Fix the background level to be the specified constant value for the entire fitting.
- -quick, -q Use only a single pass of the Levenberg-Marquardt solver to find the best fitting model.
- -slow, -s Run a more thorough search method that adds a second pass grid search in  $W_0$  and  $R_t$ .
- -randomize, -R Randomize the initial model values by searching for a new maximum around the first guess.
- -brute, -B Change how many samples are taken during the grid search. The search is square, so this value determines the number of samples on a side.
- -iterations, -I Change the number of iterations used at a given sampling step.
- -range, -J Multiplier for all the ranges considered when doing a search.
- -N Set the radial resolution of the King model.
- -Z Set the size of the King model template image.

#### A.2.1 INITIALIZATION

Superking loads the GC and PSF images, and calculates a first set of estimates for the fit parameters directly from the data. The uncertainty in the background

is found by calculating the standard deviation of the image, using an iterative  $3\sigma$  clipping process. The cluster is assumed to be in the center of the image, so that is set as the first guess. The image minimum is set to the background, although that is nearly always an underestimate. As the central potential and tidal radius are not easy to estimate directly from the image, they are set to 5 and 15 respectively. These values are chosen simply because they are good "middle" values. The initial magnitude is found by summing the image flux and converting it.

An error map is calculated and stored along with the GC image. This contains the expected noise on each pixel, and is used in calculating the  $\chi^2$  value. The exact form of the error map can be altered by changing options in the <u>superking.h</u> header file. The default error calculation incorporates all of the major sources of error

$$E(x,y) = Gain \cdot |GC(x,y)| + \sigma_{readnoise}^2 + Gain \cdot \sigma_{background}^2$$
(A.12)

Once all the initial values are calculated, and the necessary images loaded, a logfile is opened to store the results of the calculation for each step of the fitting process.

#### A.2.2 FIT EVALUATION

The quality of the fits is determined by calculating the  $\chi^2$  value for the model. This is calculated as

$$\chi^2 = \frac{1}{N_x \cdot N_y} \sum_{x}^{N_x} \sum_{y}^{N_y} \frac{(\text{Gain} \cdot \text{GC}(x, y) - (\text{Flux} \cdot \text{T}(x, y) - \text{background}))^2}{\text{E}(x, y)}$$
(A.13)

For each new set of fit values, superking determines what has changed from the previous run. As the various stages of the evaluation of a new model run at different rates, it is worthwhile to attempt to prevent any unneeded calculations. Changes in the photometric parameters, the magnitude and the background, require no changes to the model, and are implemented as just a simple reevaluation of the  $\chi^2$  value.

Changes in how the cluster is laid out, either in the cluster centering or in the scaling of the tidal radius, do require a new template image to be generated and convolved with the PSF. However, the King model used previously can continue to be used in all cases, except that of a change in  $W_0$ .

Because of the different speeds involved in the changes of different parameters, the speed of the fitting process can be improved by holding the slow parameters fixed while the faster parameters are varied. This can help alleviate the degeneracy of the fitting, as the best fitting magnitude and background can be quickly found for a given set of  $W_0$  and  $R_t$ .

#### A.2.3 FITTING PROCEDURE

If the "-randomize" option is specified, the program first randomly samples magnitude and background values in an attempt to find the best fitting initial values. The ranges for these parameters are  $\Delta m = \pm 1$ ,  $\Delta B = \pm 1000$  counts. This is repeated for the position, with a range in both  $x_0$  and  $y_0$  of  $\pm 1$  pixel. This uses a randomized hill climbing algorithm, which checks if the proposed value is better than the current value, and if so, sets the new center to that location. This ensures that a good value can be found quickly.

A grid search is the next stage of the fitting, with a range of  $W_0$  from 3.5 to 13, and a range of  $R_t$  from 0 pixels to half the image size. At each grid point, the magnitude and background are searched using the same hill climb algorithm, over ranges  $(\Delta m, \Delta B) = (\pm 0.1, \pm 150)$ . This helps ensure that these parameters are the best values possible for the given  $(W_0, R_t)$ . If this were not done, the degeneracy of these four parameters would likely prevent equally good fits across the grid.

With the optional randomized refinement of the parameters finished, a Levenberg-Marquardt solver (using the implementation provided by GSL) is used to attempt to find a good set of fit parameters. This fit is generally reasonable, but the odd

degeneracy of the parameters can cause the Levenberg-Marquardt solver to often find a local minimum instead of the final global best fit.

To rectify this, unless the "-quick" option is given, **superking** repeats the hill climb and grid searches again, with an optional second pass if the "-slow" option is also used. The ranges searched for this are given in table A.1. As is clear from these ranges, the second pass is designed to refine the fit around the final best fitting model.

With the fitting completed, the best fitting model is calculated, and the results saved to a series of images: the best fitting template, the difference image between the data and the template, the  $\chi^2$  map, and the calculated error map. If the fitting is being run from a list, a new file with the "best" extension is created that saves the best fitting values for each set of input images.

Table A.1: Search Ranges for Fitting

Parameter	$W_0$	$R_t$	$x_0$	yo	m	В	Grid Search m	Grid Search B
Initial Randomization	3.5 - 13	3.5 - 13 0 - $\frac{1}{2}$ imagesize	±1.0	±1.0	±1.0	$\pm 1000$	±0.1	±150
Pass 1	2 - 14	$\frac{1}{4}R_t - 2R_t$	±1.0	±1.0	$\pm 0.25$	±1000	±0.05	∓20
Pass 2	±0.5	±2.0	$\pm 0.5$	±0.5	±0.1	$\pm 250$	∓0.05	±25

# APPENDIX B: GLOBULAR CLUSTER CATALOG

In order to allow easy access to the globular cluster data, a SQLITE database was created to store the various measured parameters. Given that there are thousands of objects, with up to a hundred parameters for each one, no other method of organizing the data is practical.

Each object stores all of the values measured by Source Extractor for both data images. After matching the filters, the final RA and DEC are chosen, and the distance from the center of the galaxy is calulated. The next set of parameters are the photometric data calculated during the calibration phases, with instrumental and final magnitudes, and the aperture corrections and completeness values for both filters. These are combined to create the object color and final completeness. Finally, a quality flag is calculated to note how likely an object is to be a cluster. A quality of zero is reserved for the good objects, with higher values being a bitmask to denote all the reasons why an object is rejected.

For clusters that have matches in either the Kundu et al. (1999) or Waters et al. (2006) samples, that data is stored as well, with a "merge" value that gives the angular separation of objects between catalogs. The Jordán et al. (2004) Xray data is also matched in the same way, and stored for the clusters that match. Finally, the raw output of **superking** is stored, along with the calculated structural parameters defined in section 2.4.

This same database is also used to store the results from the false and UDF

frames, along with all the calibration data from the simulated cluster searches. These components are included to allow for any reanalysis at a later date.

**BIBLIOGRAPHY** 

#### REFERENCES

Anderson, J., & King, I. R. 2003, PASP, 115, 113

Anderson, J., King, I. R. 2006, ACS Instrument Sci. Rep. 2006-01 (Baltimore: STSci)

Ashman, K. M., Bird, C. M., & Zepf, S. E. 1994, AJ, 108, 2348

Ashman, K. M., Conti, A., & Zepf, S. E. 1995, AJ, 110, 1164

Ashman, K. M., & Zepf, S. E. 1998, Globular Cluster Systems, (Cambridge: Cambridge Univ. Press)

Baltz, E. A., Lauer, T. R., Zurek, D. R., Gondolo, P., Shara, M. M., Silk, J., & Zepf,S. E. 2004, ApJ, 610, 691

Barmby, P., & Huchra, J. P. 2001, AJ, 122, 2458

Baumgardt, H., & Makino, J. 2003, MNRAS, 340, 227

Beckwith, S. V. W., et al. 2006, AJ, 132, 1729

Bertin, E., & Arnouts, S. 1996, A&AS, 117, 393

Binney, J., & Tremaine, S. 1987, Galactic Dynamics, (Princeton, NJ: Princeton Univ. Press)

Brosche, P., Odenkirchen, M., & Geffert, M. 1999, New Astronomy, 4, 133

Burkert, A., & Smith, G. H. 2000, ApJ, 542, L95

Chernoff, D. F., & Weinberg, M. D. 1990, ApJ, 351, 121

Côté, P., et al. 2004, ApJS, 153, 223

Da Costa, G. S., & Freeman, K. C. 1976, ApJ, 206, 128

Djorgovski, S., & Meylan, G. 1994, AJ, 108, 1292

Djorgovski, S. 1995, ApJ, 438, L29

Fall, S. M., & Zhang, Q. 2001, ApJ, 561, 751

Fruchter, A. S., & Hook, R. N. 2002, PASP, 114, 144

Gunn, J. E., & Griffin, R. F. 1979, AJ, 84, 752

Harris, W. E. 1996, AJ, 112, 1487

Harris, W. E., Whitmore, B. C., Karakla, D., Okoń, W., Baum, W. A., Hanes, D. A., & Kavelaars, J. J. 2006, ApJ, 636, 90

Hénon, M. 1961, Annales d'Astrophysique, 24, 369

Herschel, W. 1789, Philosophical Transactions Series I, 79, 212

Innanen, K. A., Harris, W. E., & Webbink, R. F. 1983, AJ, 88, 338

Jordán, A., et al. 2004, ApJ, 613, 279

Jordán, A., et al. 2005, ApJ, 634, 1002

Jordán, A., et al. 2007, ApJS, 171, 101

King, I. 1962, AJ, 67, 471

King, I. R. 1966, AJ, 71, 64

Koekemoer, A. M., Fruchter, A. S., Hook, R., Hack, W., 2002, HST Calibration Workshop, 337

Krist, J. 1993, Astronomical Data Analysis Software and Systems II, 52, 536

Kroupa, P. 2001, MNRAS, 322, 231

Kundu, A., Whitmore, B. C., Sparks, W. B., Macchetto, F. D., Zepf, S. E., & Ashman, K. M. 1999, ApJ, 513, 733

Kundu, A., Maccarone, T. J., & Zepf, S. E. 2007, ApJ, 662, 525

Lamers, H. J. G. L. M., Anders, P., & de Grijs, R. 2006, A&A, 452, 131

Lamers, H. J. G. L. M., Gieles, M., & Portegies Zwart, S. F. 2005, A&A, 429, 173

Larsen, S. S. 2004, A&A, 416, 537

Lauer, T. R. 1999, PASP, 111, 1434

Lauer, T. R. 1999, PASP, 111, 227

Lynden-Bell, D., & Eggleton, P. P. 1980, MNRAS, 191, 483

Macri, L. M., et al. 1999, ApJ, 521, 155

McLaughlin, D. E., Harris, W. E., & Hanes, D. A. 1994, ApJ, 422, 486

McLaughlin, D. E. 2000, ApJ, 539, 618

Meurer. G. R., et al. 2002, HST Calibration Workshop (Baltimore: STSci)

Meylan, G., & Heggie, D. C. 1997, A&A Rev., 8, 1

Ostriker, J. P., Spitzer, L. J., & Chevalier, R. A. 1972, ApJ, 176, L51

Perlman, E. S., Harris, D. E., Biretta, J. A., Sparks, W. B., & Macchetto, F. D. 2003, ApJ, 599, L65

Plummer, H. C. 1911, MNRAS, 71, 460

Schechter, P. 1976, ApJ, 203, 297

Schlegel, D. J., Finkbeiner, D. P., & Davis, M. 1998, ApJ, 500, 525

Schultz, H. 1866, Astronomische Nachrichten, 67, 1

Shapley, H., 1921, Bull. Nat. Res. Coun., 2, 171

Sirianni, M., et al. 2005, PASP, 117, 1049

Sivakoff, G. R., et al. 2007, ApJ, 660, 1246

Spitzer, L. 1987, Dynamical Evolution of Globular Clusters, (Princeton, NJ: Princeton Univ. Press)

Stoughton, C., et al. 2002, AJ, 123, 485

Strader, J., Brodie, J. P., Spitler, L., & Beasley, M. A. 2006, AJ, 132, 2333

Vesperini, E., Zepf, S. E., Kundu, A., & Ashman, K. M. 2003, ApJ, 593, 760

Waters, C. Z., & Zepf, S. E. 2005, ApJ, 624, 656

Waters, C. Z., Zepf, S. E., Lauer, T. R., Baltz, E. A., & Silk, J. 2006, ApJ, 650, 885

Whitmore, B. C., Sparks, W. B., Lucas, R. A., Macchetto, F. D., & Biretta, J. A. 1995, ApJ, 454, L73

Zepf, S. E., Ashman, K. M., English, J., Freeman, K. C., & Sharples, R. M. 1999, AJ, 118, 752

Zhang, Q., & Fall, S. M. 1999, ApJ, 527, L81

